OPTIMIZING PROCESSING AND SYNTHESIS OF PRUSSIAN BLUE ANALOGS FOR SODIUM-ION BATTERIES

by

Jay Deshmukh

Submitted in partial fulfillment of the requirements
for the degree of Master of Applied Science

at

Dalhousie University
Halifax, Nova Scotia
August 2024

To my Nana, and friends, Bruno and Bolt.

“If something is important enough, you believe in it enough, do it in spite of fear. When something is important enough, you do it even if the odds are not in your favor.”

“I think it is possible for ordinary people to choose to be extraordinary.”

"Conscious breathing is my anchor.”

“Loose an I, gain an eye.”

“Process is the prize.”

Table of Contents

List of Tables

List of Figures

Abstract

Electric vehicles and energy storage systems are major drivers in the quest to accelerate the transition towards a sustainable future. However, the incumbent lithium-ion battery technology that they rely on, might be a weakness in the future because of the mismatch between rising demands and supply of scarce and expensive metals like cobalt, lithium, nickel, and copper that Li-ion cells heavily employ. To overcome this, more sustainable chemistries, i.e., sodium- and potassium-ion cells, are being investigated with the goal of incorporating more earth-abundant metals into the composition of the electrodes and establishing more sustainable supply chains. Sodium-ion cells employing manganese hexacyanoferrate (MnHCF) as the positive electrode are of particular interest because this material can be tailored to be composed of mostly earth-abundant elements like iron and manganese. However, their cycle life is not yet sufficient for grid energy storage, and they suffer from undesirable water uptake that can be detrimental to cell performance if released into the organic electrolyte in significant amounts.

This work focuses on setting up synthesis and evaluation standards for Prussian Blue Analogs as positive electrode materials in sodium-ion cells. Three distinct synthesis routes were explored: co-precipitation, hydrothermal, and mechanochemical synthesis. Optimization of synthesis and processing conditions yielded high specific energy materials that were competitive with commercial lithium iron phosphate on a Wh/kg basis. A reduction in the water content of Prussian Blue Analogs was achieved through careful vacuum drying. Overall, this work should help the future development and commercialization of sustainable cells employing Prussian Blue Analogs.

List of Abbreviations Used

a	Unit cell length in the x-direction
at.	Atomic
b	Unit cell length in y-direction
c	Unit cell length in z-direction
CAM	Cathode active material
DMC	Dimethyl carbonate
DEC	Diethyl carbonate
EDS	Energy dispersive X-ray spectroscopy
E^{O}_{Anode}	Standard electrode potential for anode
$E^{O}_{Cathode}$	Standard electrode potential for cathode
E^{O}_{Cell}	Voltage of the cell at standard conditions
F	Faraday constant
FEC	Fluoroethylene carbonate
g	Gram
h	Hour
HC	Hard carbon
L	Liter
LFP	Lithium iron phosphate
mAh	Milliampere hour
NMC	Nickel manganese cobalt
PBAs	Prussian blue analogs

PC	Propylene carbonate
pH	Power of hydrogen
Q	Reaction activity
R	Universal gas constant
SEM	Scanning electron microscope
TGA	Thermogravimetric analysis
V	Volt
V_{Cell}	Voltage of cell at non-standard conditions
V^{O}_{Cell}	Voltage of the cell at standard conditions
wt.	Weight
XRD	X-ray diffraction
α	Angle between unit cell lengths b and c
β	Angle between unit cell lengths a and c
ɣ	Angle between unit cell lengths a and b
□	$Fe(CN)_6$ vacancies present in the structure
ΔG	Gibbs free energy

Acknowledgments

I want to thank my friend and research supervisor, Dr. Michael Metzger, and other committee members, Dr. Michael Freund (co-supervisor), Dr. Jeff Dahn, and Dr. Chongyin Yang for their patience, critique, and support during the last couple of years.

I am grateful for making a few good friends during the program, especially Dr. Ning Zhang, Dr. Hussein Hijazi, and Ziwei Ye, whom I dearly miss playing soccer (and beating them at) and cycling with.

Special thanks to Vineet Mehta, Dr. Nupur Sinha, and Dr. Sun Jurng from Tesla (Palo Alto, California), for engaging in thoughtful conversations and encouraging me for my future steps during my internship.

I am grateful to my parents, Pradeep and Bhagyashree Deshmukh (Maharashtra, India), grandfather, Dr. Ashok Wasudeo Deshmukh, and aunt, Sheetal Deshmukh (Princeton, USA), who all continue to support and spoil me beyond any rationality.

Thanks to Daniel Gerald (Antigonish, Canada) and Stephen Williams (Cape Breton, Canada) for being good friends and helping me navigate the Canadian system.

Thanks to Mike Johnson and Jessie Harlow for managing the lab and equipment, without whom my experiments could have barely kept going.

I acknowledge the funding support from the Natural Sciences and Engineering Research Council of Canada (NSERC) and Tesla Inc. for this work.

Chapter 1. Introduction

1.1. Motivation

In the pursuit of a sustainable energy future, renewable energy generation sources like wind and solar are being deployed. However, due to their intermittent nature of generation, deployment of energy storage solutions is critical to help make up for periods where the load exceeds generation. Li-ion battery (LIB) technology has shown its prowess greatly in electric vehicles (EV) and energy storage systems (ESS) applications. Due to the culmination of collective research and innovation in the past decades, modern LIBs boast long lifetimes and high energy densities. [1] However, as we look to meet the terawatt-hour scale demand in the future, the heavy reliance of LIBs on scarce and expensive metals like Li, Cu, Ni, and Co represents a challenge for the supply chain. Figure 1.1. shows supply-demand projections of lithium carbonate equivalent (LCE), a key ingredient needed to make Li-ion cells, using a bottom-up methodology, aggregating granular micro-level inputs and historical data to arrive at the final projection (retrieved from BloombergNEF [2]). This projection also takes various losses on the manufacturing side into account, e.g., material wastage (7.5%), inactive material (5%), and losses during the formation cycle of a cell (15%). It shows that the supply of LCE will most likely struggle to keep up with the demand by the end of the decade due to rising demands from various sectors. A premium may be charged for consumer electronics and EVs, which might make it difficult to allocate the desired number of cells for ESS where cost-effectiveness is

paramount since renewables are competing with other relatively cheap energy sources like coal.

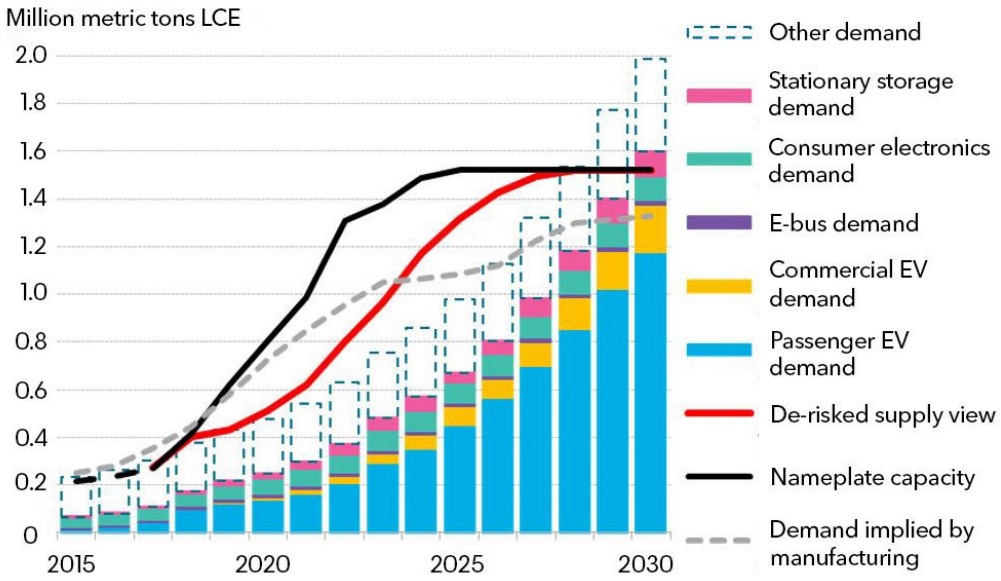

Figure 1.1. Li supply-demand using bottom-up methodology for specific use cases, retrieved from BloombergNEF (2019). [2] These calculations take into account material wastage (7.5%), inactive material (5%), and material loss during the formation cycle (15%).

LIBs employing the layered oxide class of positive electrode materials offer the highest energy density, both on a gravimetric and volumetric basis (see Section 2.1. for an energy densities comparison of different positive electrode types), and can be reserved for more demanding applications like long-range EVs and electric aviation. Lithium iron-phosphate (LFP) based Li-ion cells have lower energy density than their oxide counterparts but can help reduce the cost to some extent by eliminating the use of Ni and Co. However, more cost savings and sustainability goals need to be realized by minimizing the usage of the remaining critical metals like Li and Cu apart from Co and Ni. In the case of ESS, the

requirement for high energy density may be less critical (due to its stationary nature) and hence lower energy density battery chemistries could potentially be deployed if cost savings during the total lifetime make them competitive.

Hence, battery technologies of the likes of Na- and K-ion are being investigated that can employ more earth-abundant and cheaper elements in the positive electrode materials, also referred to as cathode active materials (CAMs), and offer a more sustainable supply chain. Another advantage of these two chemistries is the ability to use Al as the current collector for the negative electrode side, which cannot be realized in LIBs due to the formation of a Li-Al alloy at low potentials. Using Al helps to further reduce the weight (Cu being ~3x heavier than Al) and cost (closing spot prices for Al and Cu were 2.58 and 9.84 USD/kg, respectively as of June 7th, 2024). [3][4] Figure 1.2. shows the abundance in the earth's crust for key elements used in major Li-ion and Na-ion battery (SIB) chemistries. For SIBs, hard carbon is often the most popular choice of negative electrode, and hence the exact chemistry of a cell is often characterized by the choice of positive electrode. Layered oxides, V-containing phospho-olivines (NVPF), and Prussian Blue Analogs (PBAs) are three major classes of positive electrode materials for sodium-ion batteries (see section 2.1 for a brief overview of these various materials). The PBA class of positive electrode materials is particularly of interest for SIBs because only this class of positive electrodes can be designed to employ mostly earth-abundant elements like Fe and Mn (see Figure 1.2.), which will be critical for terawatt-hour scale battery deployment.

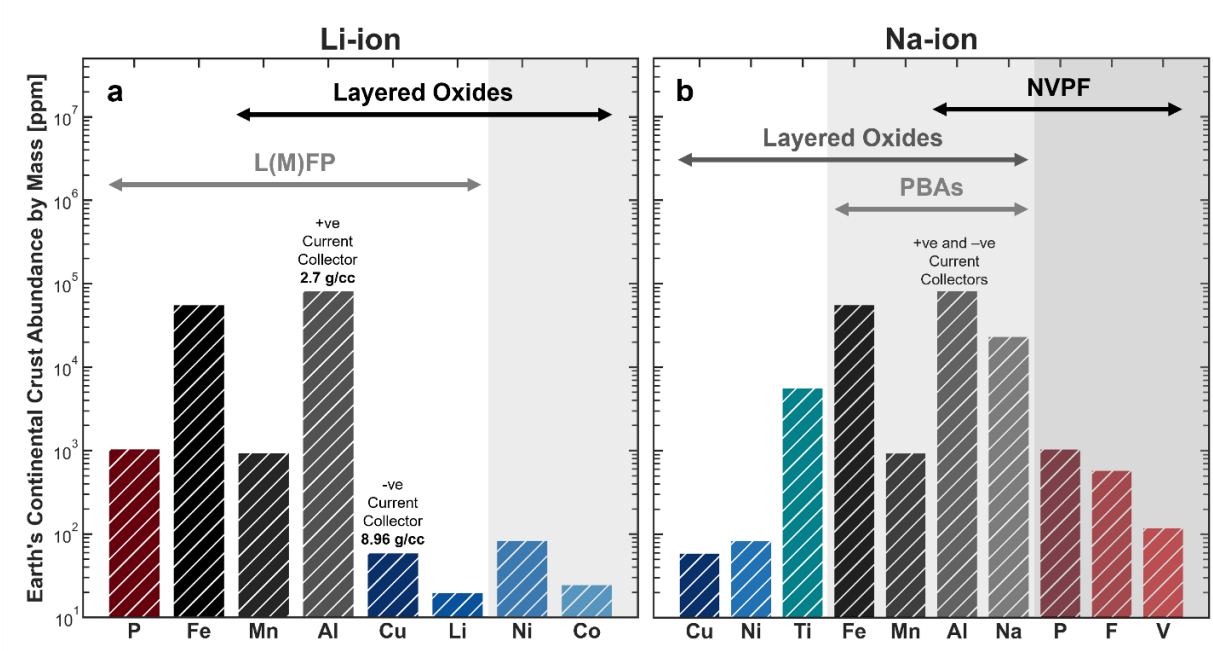

Figure 1.2. Abundance of key elements for (a) Li-ion and (b) Na-ion batteries in the earth's continental crust. Numbers retrieved from CRC Handbook of Chemistry and Physics. [5]

1.2. Specific Objectives and Scope of Thesis

This work focuses on establishing synthesis and processing standards for the development of the Prussian Blue Analogs (PBAs) class of positive electrode materials. Multiple synthesis routes such as co-precipitation, hydrothermal, and mechanochemical were explored. Rigorous optimization of the co-precipitation synthesis route and the processing conditions shall help to improve the electrochemical performance of PBAs and lead to gravimetric energy densities that are competitive with commercial LFP. The electrochemical performance of these in-house materials was compared with literature references and commercial materials, to show superior electrochemical performance for the in-house materials. Water uptake and subsequent release of water into the non-

aqueous electrolyte during cycling is a known issue for PBAs, which decreases the lifetime and performance of PBAs when organic electrolytes are used. This issue was addressed in this study by optimizing the processing conditions post-synthesis. Overall, this work shall help to demonstrate that PBAs can be a viable next-generation positive electrode active material for non-aqueous Na-ion batteries in the following nine chapters.

Chapter two of this thesis discusses the relevant electrochemistry principles that Li-ion and Na-ion cells work on with the similarities and differences that they share. This is followed by a brief discussion of the roles and types of positive and negative electrodes, including a comprehensive background and a review of the current understanding of PBAs in literature.

Chapter three describes the main characterization techniques used in this work, which include X-ray diffraction (XRD), thermogravimetric analysis (TGA), scanning electron microscopy (SEM), energy dispersive X-ray spectroscopy (EDS), and inductively coupled plasma-optical emission spectroscopy (ICP-OES). The underlying working principles will be discussed to establish how meaningful takeaways can be generated from these techniques to augment the understanding of the PBA materials. This chapter also describes the cell assemblies and electrochemical tests used to study PBA-based batteries.

Chapter four goes over the description of experimental routes explored in this study, which include co-precipitation, hydrothermal, and mechanochemical synthesis. The details on synthesis setups and chemicals are also covered in this section.

Chapter five of this thesis provides a discussion of the synthesized products and the results of their characterization, which includes phase identification by XRD, morphology inspection using SEM, and elemental compositions using ICP-OES and EDS analysis.

Chapter six will present the effects of processing and drying conditions on structural changes in PBAs. Phase changes as a function of different processing conditions and water uptake are studied using XRD and TGA, with strong correlations observed between the results from these two techniques.

Chapter seven will look at a way of increasing the sodium content in PBA materials post-synthesis to enable the usage of sodium-deficient positive electrodes in practical full-cells. This was carried out using two different reducing agents.

Chapter eight will look at the electrochemical evaluation of the PBAs synthesized via the optimized co-precipitation route. Long-term capacity retention and rate performance were evaluated in half-cells. Their performance is also compared with commercial PBA and LFP.

Chapter nine will conclude the thesis by summarizing the main findings of this work and discussing potential next steps.

Chapter 2. Electrochemistry of Li- and Na-ion Chemistries: Similarities and Differences

In the construction of a rechargeable galvanic alkali-ion cell with Li- or Na-ion chemistry, the positive and negative electrodes are separated by an electronically insulating separator as shown in Figure 2.1. Typically, a non-aqueous liquid electrolyte, also electronically insulating but ionically conductive, is used, which is a mixture of solvents (common examples include alkyl carbonates and ethers) and the respective salts such as lithium hexafluorophosphate ($LiPF_6$) or sodium hexafluorophosphate ($NaPF_6$) to enable ion transport. Positive and negative electrodes are made by mixing a slurry consisting of active materials, binder, and carbon diluents in a suitable formulation before casting onto the current collectors to achieve a desired mass loading that dictates the absolute capacity of a cell.

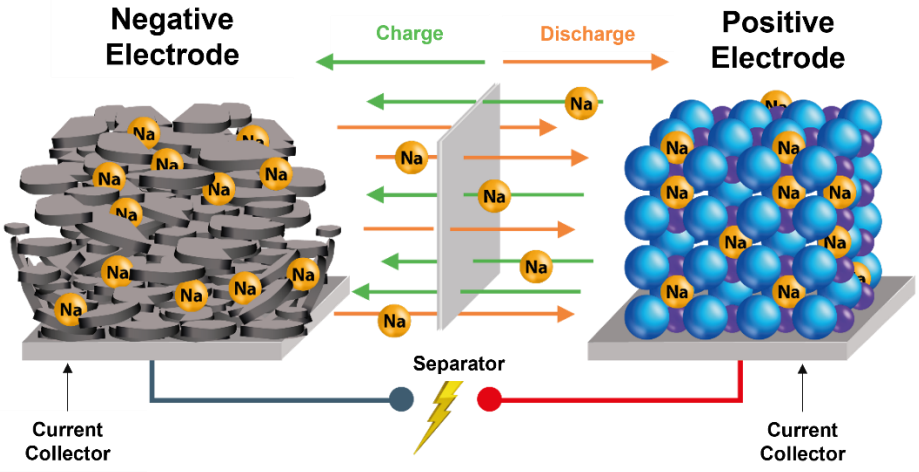

Figure 2.1. Schematic showing the high-level working principle of a typical Na-ion cell. Figure adapted from work by Daniel and Besenhard (2011), published in *Handbook of Battery Materials* (DOI: 10.1002/9783527637188). [6]

After drying, the electrodes are calendered, slit, and later wound or stacked and inserted in a casing before filling with electrolyte. Some common cell formats include coin, cylindrical, pouch, and prismatic, depending on the end application (see Figure 2.2).

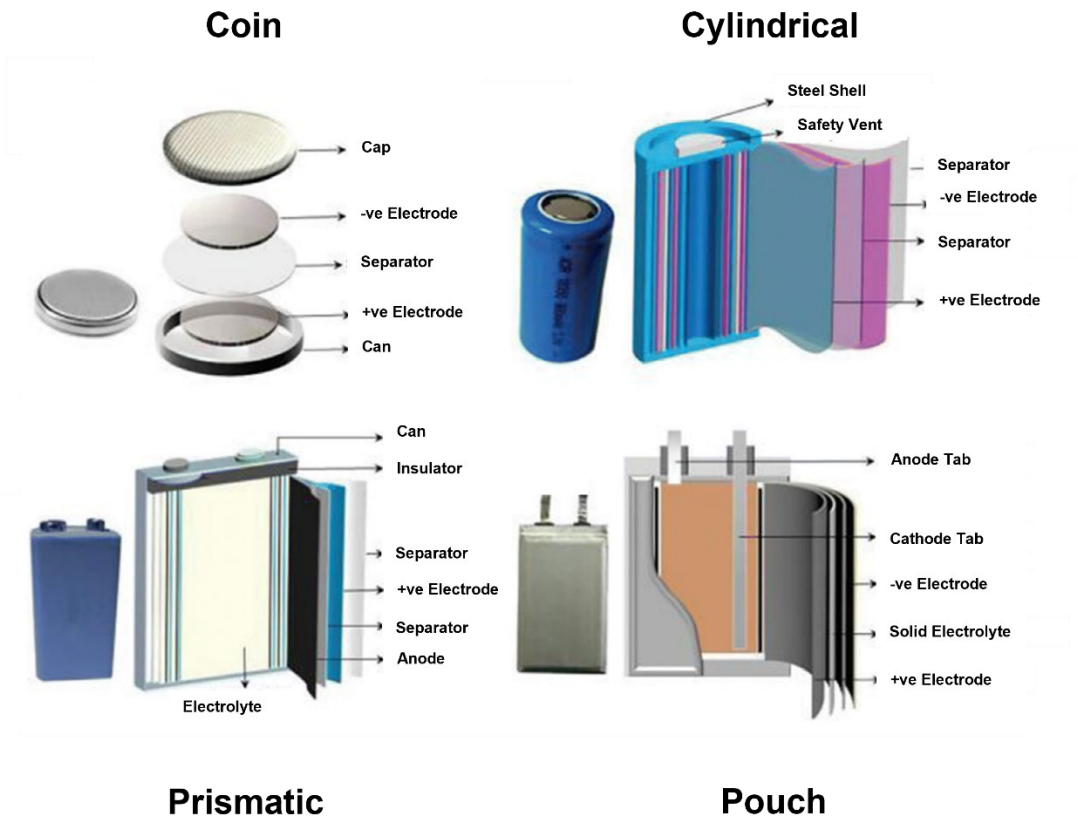

Figure 2.2. Some common Li-ion cell formats. Figure adapted from work by Liang et al. (2019), published in *InfoMat* (DOI: 10.1002/inf2.12000). [7]

During charging, energy is supplied externally which causes Li^+/Na^+ ions to move from a low-energy state in the positive electrode to a high-energy state in the negative electrode, increasing the overall energy of the cell in the process. To neutralize the positive charges from Li^+/Na^+ ions at the negative electrode side, electrons travel externally to complete

the circuit since the electrolyte and separator are electronically insulating. During discharge, the direction of flow of Li^+/Na^+ ions and electrons is reversed and energy is supplied by the cell to do work, lowering the energy of the cell in the process. Equations 1 and 2 represent charge-discharge reactions for Na-ion PBA/hard carbon and Li-ion LFP/graphite cells, respectively.

$$Na_2Mn[Fe(CN)_6] + yC \underset{Discharge}{\overset{Charge}{\rightleftarrows}} Na_{2-x}Mn[Fe(CN)_6] + Na_xC_y \quad (1)$$

$$LiFePO_4 + yC_6 \underset{Discharge}{\overset{Charge}{\rightleftarrows}} Li_{1-x}FePO_4 + yLi\underset{\overline{y}}{x}C_6 \quad (2)$$

The energy (E) of a cell can be calculated by integrating the area of the voltage vs. capacity curve associated with that particular chemistry. However, it may also be approximated as a product of the average cell voltage (V) and the capacity (Q) according to Equation 3:

$$E\,[Wh] = V_{Cell}\,[V] \times Q[Ah] \quad (3)$$

For standardized conditions, $V°_{Cell}$ can be determined as the energy difference between the standardized redox energies of the positive electrode or cathode ($E^O_{Cathode}$) and the negative electrode or anode (E^O_{Anode}) according to Equation 4:

$$V°_{Cell} = E°_{Cathode} - E°_{Anode} \quad (4)$$

The voltage of a cell at any given set of conditions is governed by the Gibbs free energy (ΔG) associated with that particular set of conditions (see Equation 5). ΔG is a function of temperature and the Na/Li concentration in the cathode and anode (later influencing the chemical potentials).

$$V = -\frac{\triangle G}{nF} \tag{5}$$

In Equation 5, F is the Faraday constant (9.65 x 10^4 C/mol of electrons), and n is the number of electrons transferred for a given redox reaction. A cell is considered in a fully discharged state (low energy) when all the Li/Na inventory that contributes to the capacity is present at the positive electrode, while it is in a fully charged state (high energy) when the entire active inventory resides at the negative electrode. However, in real cells, the complete extraction of Li/Na from the positive electrode is often not permitted, even if that means reduced capacity, due to the limited stability window of the electrolyte and possible irreversible phase transition(s) of the active materials beyond a certain degree of extraction. [8][9] From Equation 3, it can be deduced that increasing the voltage is a key lever to increase the energy stored in a cell, which can be achieved by pairing two electrodes with a large difference in chemical potentials as shown in Figure 2.3. This difference should take into account the energy of the electrons as well as the influence of insertion species. So, to get a high voltage cell, the energy of the negative electrode should lie as high as possible (i.e., requiring the stabilization of lower oxidation states with a higher energy band), while the positive electrode energy should lie as low as possible (i.e., requiring the stabilization of higher oxidation states with a lower energy band). [10]

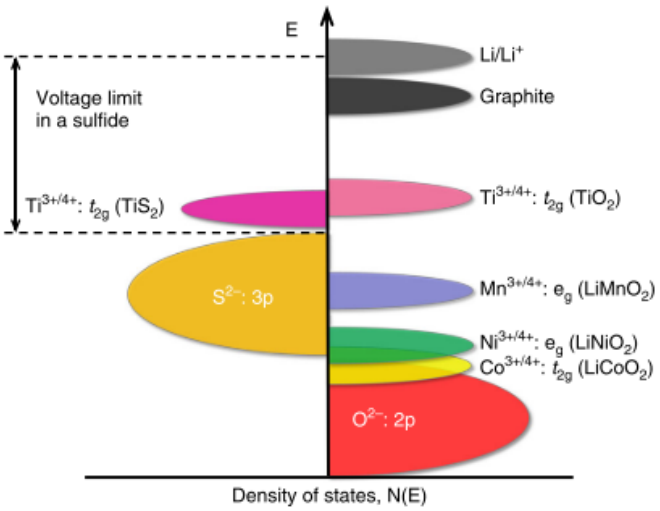

Figure 2.3. Positions of the redox energies relative to the top of the anion: p bands. Figure retrieved from work by Manthiram (2020), published in *Nature Communications* (DOI: 10.1038/s41467-020-15355-0). [10]

Whittingham, in 1976 at Exxon Corporation, demonstrated the first rechargeable Li cell with a titanium disulfide positive electrode (TiS_2) and a Li metal negative electrode which used $LiClO_4$ dissolved in solvents like dimethoxymethane and tetrahydrofuran as the electrolyte. [11] However, it had three major shortcomings: low discharge voltage (<2.5 V), a Li deficient positive electrode (meaning it cannot be paired with non-lithiated negative electrodes like graphite), and a reactive Li metal counter electrode. In the subsequent years, major contributions were made to the field to address these issues, particularly by Goodenough and co-workers whose discovery of oxide-based positive electrode materials solved the first two shortcomings. By replacing the sulfide with an oxide group, it meant that the earlier restricted lower-energy bands of transition metals such as $Mn^{III/IV}$ and $Co^{III/IV}$ were now accessible (see Figure 2.3), giving rise to > 3 V cells.

However, the environment surrounding the transition metal can also influence the energies of redox active sites. As shown in Figure 2.4., $Fe^{II/III}$ has different energies because of the distinct groups surrounding it. In 1983, Yoshino fabricated the first Li-ion cell with a $LiCoO_2$ positive electrode and a graphite negative electrode using a non-aqueous electrolyte before subsequent commercialization by Sony in 1991. [12] Although Li and Na belong to the same column in the Periodic Table and share similar oxidation states, the difference in their size and reduction potential means a simple one-to-one imitation of electrode and electrolyte design is far from reality which will be discussed next.

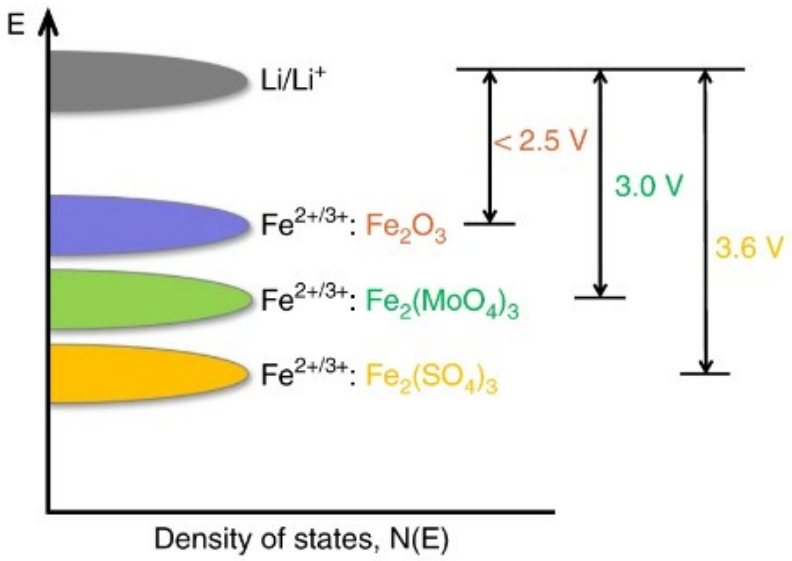

Figure 2.4. Role of counter-cations in shifting the redox energies in polyanion oxide positive electrodes. Figure retrieved from work by Manthiram (2020), published in *Nature Communications* (DOI: 10.1038/s41467-020-15355-0). [10]

2.1. Positive Electrode Active Materials

Research targeting SIBs was already happening in the 1980s in parallel to LIBs, with the likes of $NaCoO_2$, $NaFeO_2$, $NaMnO_2$, and $NaCrO_2$ being some of the earliest potential positive electrode active material choices. [13] However, the early commercial success of LIBs in the 1990s, mainly by pairing $LiCoO_2$ with graphite, led to the slowdown of the progress rate in SIB research. An ideal positive electrode active material should possess a high average oxidation/reduction potential versus the negative electrode (but within a given electrolyte stability window) in order to allow high energy density according to Equation 4. In the current state-of-the-art LIBs, the layered oxide class offers the highest volumetric and gravimetric energy densities (see Figure 2.5). Their general formula is $LiTMO_2$, where transition metal (TM) can be of a single type, like $LiCoO_2$, or a combination of different TMs like $LiNi_{1/3}Mn_{1/3}Co_{1/3}O_2$ and $LiNi_{0.8}Mn_{0.1}Co_{0.1}O_2$ (abbreviated as NMC111 and NMC811, respectively). Due to the slopy shape of the voltage-capacity profile of layered oxides (unlike lithium iron phosphate), higher voltage operation is needed to access more capacity. However, operation at higher voltage can cause oxidation of the electrolyte and escape of lattice oxygen which leads to rapid voltage polarization and capacity decay. [8] Hence, the upper voltage cut-off is restricted and the complete theoretical capacity of $LiTMO_2$ is hardly achieved. In most common ternary NMCs, Mn does not change its oxidation state in the tenable voltage window operation, staying in the +4 state. Hence, Mn does not offer any capacity but rather provide stability to the structure. Whereas in ternary NMCs, Ni readily undergoes a change in oxidation states from +2 to +3 towards +4, thus actively contributing to the capacity of the cell. Hence, Ni-rich materials are suited for high energy density requirements (see Figure 2.5). $LiCoO_2$

was the first commercial positive electrode and continues to be the favored choice in today's portable electronics applications, due to higher volumetric and gravimetric energy densities. However, $LiCoO_2$ is expensive, less safe, and shows more capacity fade and voltage polarization than NMCs with moderate Ni contents. Cycle life and cost requirements are more stringent in EVs and ESS than in portable electronics. Hence, balancing the transition metal (TM) composition is critical for meeting specific applications.

Lithium iron phosphate (LFP), despite eliminating Co and Ni, received little attention in the early days of LIB research compared to layered oxides due to its relatively low energy density and other shortcomings that existed at that time. One of the biggest shortcomings of LFP was its lower electronic conductivity, which was addressed by Zaghib and co-workers by reducing the particle size and applying an effective carbon coating. [14][15] This enabled successful LFP commercialization, making it now the favored choice for short-to-mid-range EVs and ESS products. Due to the inherent safety (and by extension, lower heat flow) of LFP over NMC positive electrode materials, the construction of large LFP cells is permitted. By building large format cells, reduction in usage of inactive materials and balance of plant accessories can be achieved beyond cell level as well which helps bridge the energy density gap, and hence the large volumetric energy density differences shown in Figure 2.5b are hardly ever realized to its full potential, especially for NMC and LCO materials, where limiting the upper charge cut-off for better retention results in significant losses in energy densities because of the slopy voltage-capacity profile. LCO has the highest theoretical energy densities, but most common LCO cells rely on an

upper-cutoff voltage of less than 4.6 V or less typically for longer lifetimes and safety reasons (but are still significantly energy denser than LFP at the materials level). BYD (China) showed that gains in energy density can be realized at the pack level for LFP by redesigning the cell architecture, thus closing the energy density gap between it and the layered oxides. [16]

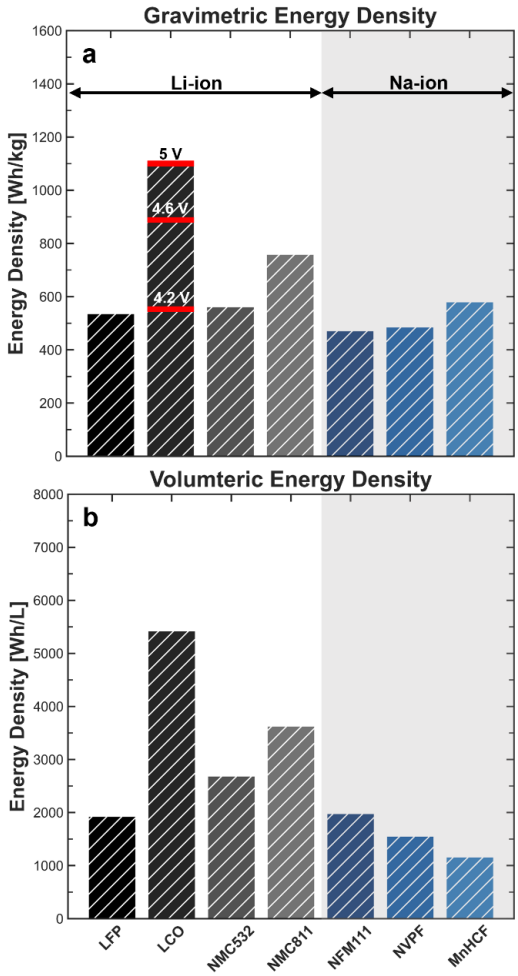

Figure 2.5. (a) Gravimetric and (b) volumetric energy densities of some common Li- and Na-ion positive electrode materials. Volumetric energy densities were calculated using crystal densities: 3.6, 5.08, 4.78, 4.2, 3.2, and 2 g/cc for LFP, LCO, NMCs, NFM111, NVPF and MnHCF, respectively. Capacities and voltages used for these calculations are summarized in Table XI (Appendix).

However, more cost savings are desired by eliminating Li and Cu to enable terawatt-hour scale ESS deployment, which has led to renewed interest in beyond Li chemistries like Na, K, Ca, Mg-ion, etc. with the aim of employing more earth-abundant elements into their overall composition. Na-ion seems to be the forerunner among other chemistries in terms of commercialization, with the likes of Contemporary Amperex Technology Limited (CATL) from China already announcing Na-ion-based cells in their future roadmap in 2021. [17]

Hard carbon is the most popular negative electrode choice for SIBs (see Section 2.1.2), and hence the type of SIB chemistry of a cell can be categorized by the type of positive electrode utilized. Positive electrode choices for SIB can be divided into three major classes: Vanadium fluorophosphates, layered oxides, and Prussian Blue Analogs. Vanadium-based phospho-olivines, like $Na_3V_2(PO_4)_2F_3$ or NVPF, have received considerable attention in the academic community. [18][9][19][20] This class of positive electrode material allows good C-rate performance (i.e., fast charge and high power) and long lifetimes but suffers from lower energy density (due to the heavy V atom and the numerous atoms in the polyanionic group). Vanadium, despite having an abundance in the earth's crust similar to that of nickel and copper (see Figure 1.2), is a significantly more expensive metal because of its complex recovery process and has undergone multiple price fluctuations, even spiking to around USD 66/kg in 2019-2020, a ten-fold increase from its 2016 price. [21] Also, vanadium is highly concentrated in only a handful of locations worldwide (>98% of its ores are found in just four countries) which makes supply chains for a true scale-up somewhat non-ideal. Despite these challenges, Tiamat

(France) is pursuing its commercialization with plans of commissioning a 0.7 GWh scale factory by 2025 and eventually a 5 GWh plant by 2029. [22]

Like Li-layered oxides, Na-layered oxides (Na_xTMO_2) offer higher volumetric and gravimetric energy densities than other mainstream positive electrode classes. However, due to the larger size of Na, it is possible for it to occupy prismatic sites in addition to the octahedral site occupied by Li in layered oxides. Hence, Na layered oxides are further divided into two major types, O3 and P2, depending on the stacking nature as suggested by Delmas et al., [23] where O and P stand for octahedral and prismatic sites occupied by Na, respectively. The number after O and P denotes how many distinct (TMO_2) layers are needed in order to generate a self-repeating unit. While O3 can be synthesized in a Na-rich phase, it usually suffers from poor capacity retention when operating at > 4 V due to irreversible phase transitions. [9] Whereas P2 has decent capacity retention even after cycling to 4 V, but usually suffers from a Na-poor phase upon synthesis (x often <0.7) which is impractical for full-cells where Na-deficient negative electrodes are used. [24][25]

In general, although Na layered oxides offer competitive specific energy similar to that of LFP, the usage of considerable amounts of Ni still remains undesirable, which makes exploration of other sustainable positive electrode choices important.

2.1.1. Prussian Blue Analogs

Hexacyanometalates or Prussian Blue Analogs (PBAs) are a class of cyano-containing polyanion positive electrode active materials that can be synthesized easily at low

temperatures and be designed to employ mostly earth-abundant elements found at >800 ppm concentration in the earth's continental crust (see Figure 1.2) with an even geographical distribution. Interestingly, it was first discovered as a blue pigment in Berlin by Johann Jacob von Diesbach and Johann Conrad Dippel in the year 1706 and still continues to be used as a dye until the present day, [26] see Figure 2.6 for a high-level timeline of PBA development.

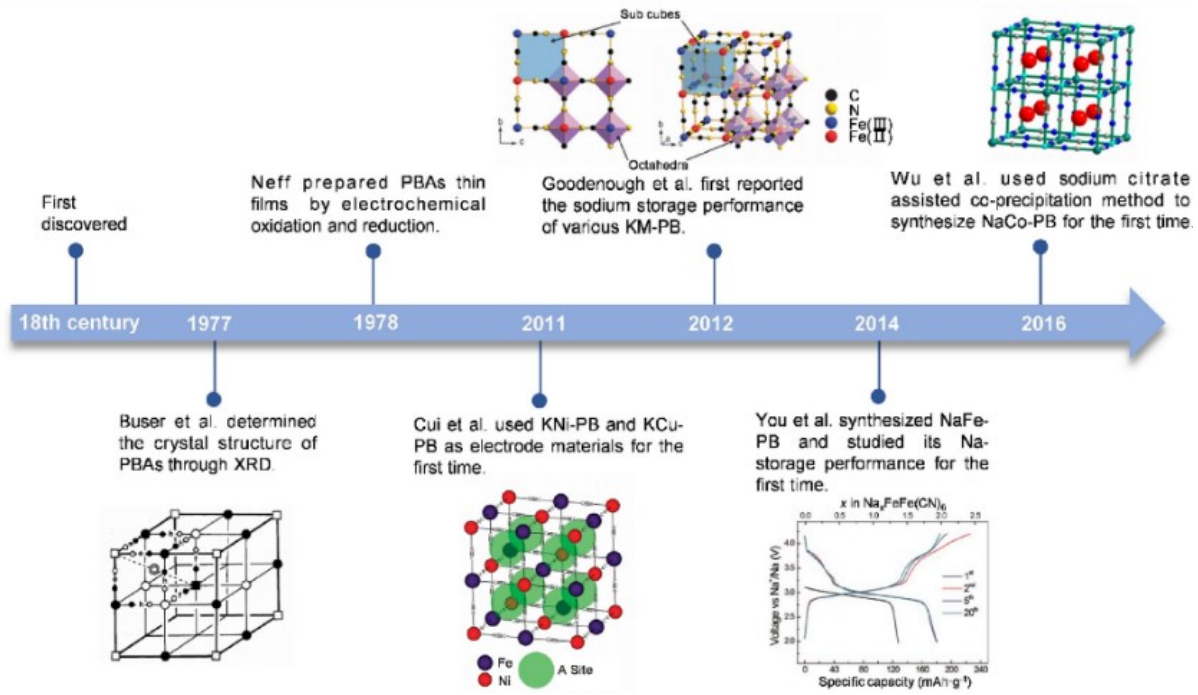

Figure 2.6. Key milestones in PBA development. Figure retrieved from work by Fu et al. (2024) with permission, published in *Rare Metals* (DOI: 10.1007/s12598-024-02887-3). [27]

The first scholarly work on Prussian Blue was published in 1710, in the first volume of *Miscellanea Berolinensia ad incrementum scientiarum,* the new scientific journal of the Royal Prussian Society, with mention of it being low-cost and non-toxic. [26] Since then, it

has found its way into various applications like catalysis, sensors, energy storage, etc. due to its highly tunable properties.

Buser et al. first analyzed the structure of a PBA in 1977 by using X-ray diffractometry and presented refinement results. [28] Wessels, Peddada, Huggins, and Cui, from Stanford University, first demonstrated the use of a PBA as an electrode material for sodium and potassium insertion in 2011. [29] They demonstrated stable capacity retention over 5,000 cycles for Ni-containing PBAs and an impressive ability to deliver >66% of capacity at a high C-rate of 41.7 C, but the material suffered from the relatively low absolute capacity (59 mAh/g at C/6 rate). In 2012, after this work, Pasta et al. from the same group, reported a similarly impressive capacity retention and high power performance for Cu-containing PBA in aqueous electrolyte but it also suffered from a low absolute capacity (54 mAh/g at 1C rate). [30] Their lower capacities and use of significant amounts of critical metals, like Ni and Cu, incentivized researchers to try a variety of different synthesis approaches with the goals of increasing energy density by using organic electrolytes for larger operational voltage windows and incorporating more cheaper transition metals in the composition. [31][32][33][34]

A major advantage of PBAs over other positive electrode active materials is that they permit the use of non-toxic aqueous slurry processing during coating for further reduced cost and a lower environmental footprint. [35][36] Wide diffusion channels in PBAs allow them to sustain very high current densities (critical for fast charge and high power applications) and promise long lifetimes [37] but at the expense of low volumetric density

arising from the lower crystal density of ~2 g/cc. For applications like ESS and short-range EVs, lower energy density may be tolerable if the cost of energy throughput over the total lifetime is competitive.

PBAs can be represented by the general formula $A_xM'[M(CN)_6]_y\square_{1-y}\cdot zH_2O$. In this stoichiometry, insertion species, A, can be Li^+, Na^+, K^+, Mg^{2+}, Ca^{2+}, NH_4^+, etc., and transition metals (TMs), M and M', are bonded to C and N, respectively (M'-N≡C-M, see Figure 2.7.). M and M' can be redox active species like Fe and Mn or redox inactive species like Ni, Cu, Co, etc. in the pragmatic voltage window of usually 2–4 V vs. Na/Na^+. Table I represents stoichiometries and electrochemical properties of some representative PBAs. $M(CN)_6$ vacancies can be present in the structure, represented by □, and are the defects generated during synthesis as a result of the rapid co-precipitation process. These vacancies lead to reduced specific capacity due to limited redox active centers for charge compensation. It is currently unclear in the literature whether $M(CN)_6$ vacancies improve ion transport and capacity retention (see below). The water found in PBAs can be of three types: interstitial, surface, and co-ordinated. Interstitial water competes with Na for similar sites inside the structure, while co-ordinated water is found in $M(CN)_6$ vacancies. In general, $M(CN)_6$ vacancies are undesired since they lead to the formation of the co-ordinated water in the structure, which can cause detrimental side reactions if it escapes into the organic electrolyte. Furthermore, $M(CN)_6$ vacancies lead to a reduction in available redox sites, which is also undesired as it lowers the capacity of the material. Hence, a lot of work reported in the literature has focused on reducing these vacancies.[38][39][40] However, some reports have highlighted that $M(CN)_6$ vacancies may help inhibit

distortion [41] and increase ionic conductivity in the structure by providing possible alternative diffusion to the <100> pathway [42] (see red arrow in Figure 2.7). Thus, a more in-depth understanding of these vacancies needs to be developed in future work to find a balance between a high-capacity defect-free structure and possible fast rates and longer lifetimes due to some defects in the PBA structure.

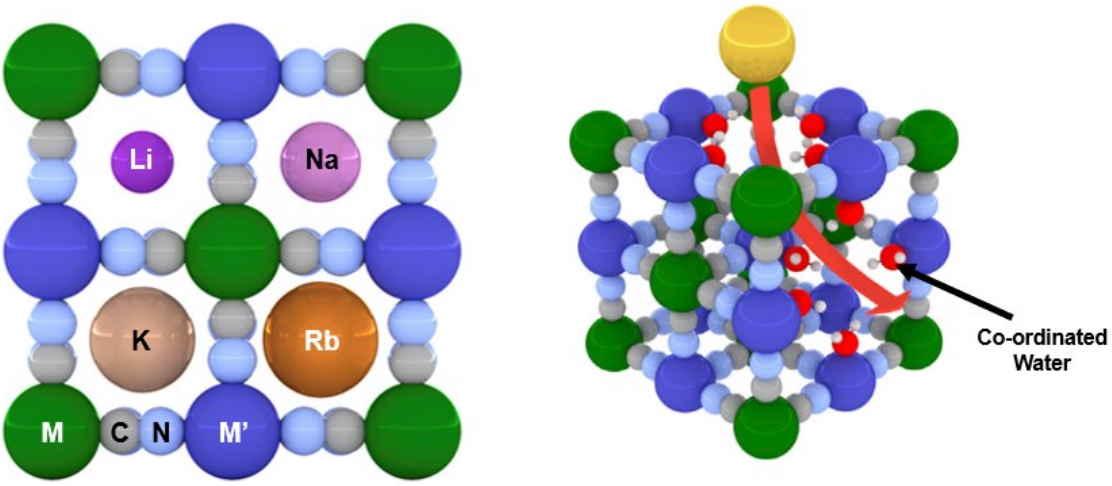

Figure 2.7. Schematic representing bonding network and stoichiometry of PBAs. Figure adapted from work by Hurlbutt et al. (2018) with permission, published in *Joule* (DOI: 10.1016/j.joule.2018.07.017) [42]

Table I. Electrochemical properties of some representative PBAs.

Analog	**Stoichiometry** Discharged ⇌ Charged	**Theoretical Cap. [mAh/g] (in 2-4 V vs. Na/Na^+)**	**Avg. Dis. Voltage [V] (vs. Na/Na^+)**
NiHCF	$Na_2Ni^{II}[Fe^{II}(CN)_6] \rightleftharpoons Na_1Ni^{II}[Fe^{III}CN)_6]$	~85	~3.1
FeHCF	$Na_2Fe^{II}[Fe^{II}(CN)_6] \rightleftharpoons Na_0Fe^{III}[Fe^{III}CN)_6]$	~170	~3.15
MnHCF	$Na_2Mn^{II}[Fe^{II}(CN)_6] \rightleftharpoons Na_0Mn^{III}[Fe^{III}(CN)_6]$	~171	~3.45

The open framework structure of PBAs with wide diffusion channels allows them to easily absorb moisture in their bulk, then referred to as interstitial water. Interstitial water leads to structural changes and potential side reactions with organic electrolyte solvents and sodium salts when released into the electrolyte during cycling. Table II summarizes common phases found in PBAs as a function of different water and Na contents. The rhombohedral phase is obtained when the Na content is high ($x>1.8$), and the structure is nearly free of water. However, upon water uptake, the crystal structure converts from rhombohedral to monoclinic phase. [43][44] For PBAs with moderate Na contents ($0<x<<2$), the cubic phase (with lattice parameters a = b = c) is dominant, [45][46] irrespective of water content, whereas for the fully de-sodiated material ($x\sim0$), the tetragonal phase is reported. [47][48] In the case of MnHCF, the rhombohedral phase shows higher capacity and discharge voltage compared to the hydrated monoclinic phase. [49][50]

Table II. Commonly reported PBA phases for different sodium and water contents.

Phase	Na (x)	Water (z)
Rhombohedral	~2	~0
Monoclinic	~2	≠ 0
Cubic	0<x<<2	≥ 0
Tetragonal	~ 0	≥ 0

Figure 2.8 shows the XRD patterns for some representative PBAs with distinct phases reported in the literature for different sodium and water contents. These patterns will be used as references when identifying the crystal structure of the different PBA materials in this thesis. As can be seen, the Na-rich rhombohedral and monoclinic phases, despite having the same chemical composition, show different diffraction patterns because of the different amounts of water present in them (see Table II). A phase transition from cubic to monoclinic results in the splitting of peaks due to a reduction in symmetry with more diffraction planes arising because of the presence of more than one type of body diagonal. (see Section 3.1)

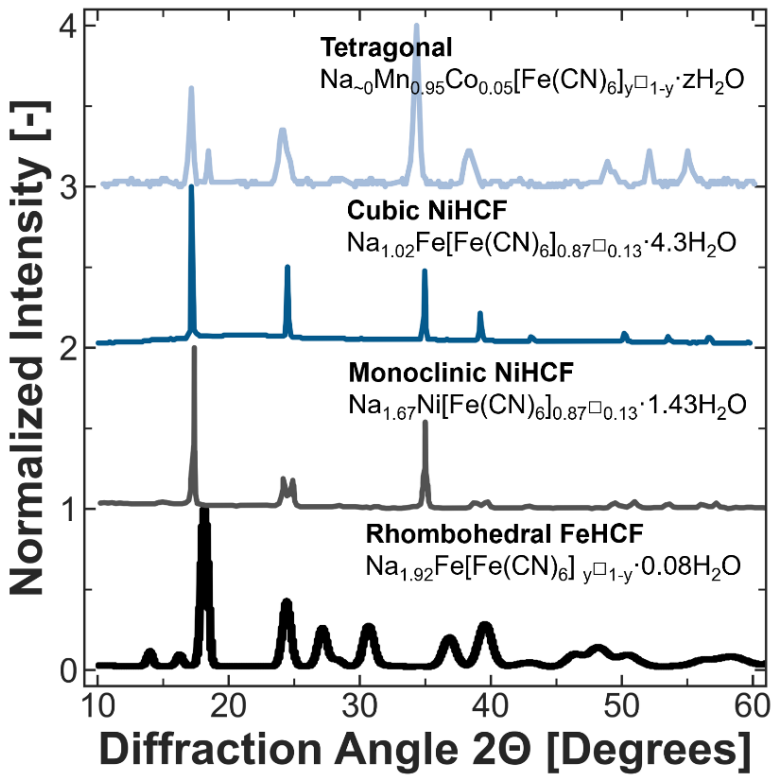

Figure 2.8. XRD patterns for some typical PBAs reported in the literature. Patterns for tetragonal, cubic, monoclinic, and rhombohedral PBAs were retrieved from work by Xu et al. (2019), [49] Zuo et al. (2022), [51] Rehman et al. (2020), [52] and Wang et al. (2015), [46] respectively.

2.1.1.1. Electronic Configuration of Prussian Blue Analogs

M and M' in the formula represent two distinct metal sites in the structure, bonded to 6 C and 6 N atoms, respectively, in an octahedral geometry. Transition metals M and M' can exhibit different spin states depending on their electronic configurations and ligand environment. Due to this, some TMs can be susceptible to Jahn-Teller distortions, which may affect the cycle life of a cell (discussed in Section 8.2).

Degeneracy in either t_{2g} or e_g orbitals is necessary for a TM to show Jahn-Teller distortion.

The electronic state of the central atom is influenced by the splitting energy (Δ) as well as the number of electrons in all d-orbitals. While the splitting energy itself is influenced by the nature of the ligands and the charge on the TM.

Crystal field theory (CFT) can help qualitatively describe the breaking of the degeneracy of the central transition metal's d orbitals under the influence of ligands. An isolated single TM ion has all five d orbitals at the same energy (see Figure 2.9). However, when it is approached by ligands, different orbitals face different repulsions due to differences in their geometries. For example, in the case of octahedral geometry, ligands approach the central atom from all directions x, y, and z, which make electrons in d_{z^2} and $d_{x^2-y^2}$ orbitals experience greater repulsion since they lie along the axes. This leads to the eventual splitting of the degenerate orbitals into orbitals of higher energy: e_g (d_{z^2} and $d_{x^2-y^2}$) and lower energy: t_{2g} (d_{xy}, d_{xz}, and d_{yz}).

The difference in energies of e_g and t_{2g} is called crystal field energy and is represented by Δ_O in the case of octahedral complexes. According to the Aufbau principle, orbitals are filled with increasing order of energies, meaning that in the octahedral case, t_{2g} will populate before e_g. Hund's rule serves as a guide to fill the electrons in these orbitals such that it promotes the highest number of unpaired electrons to minimize repulsions. However, once the t_{2g} orbitals are half-filled, the situation will be more complex and determine the spin state of the transition metal.

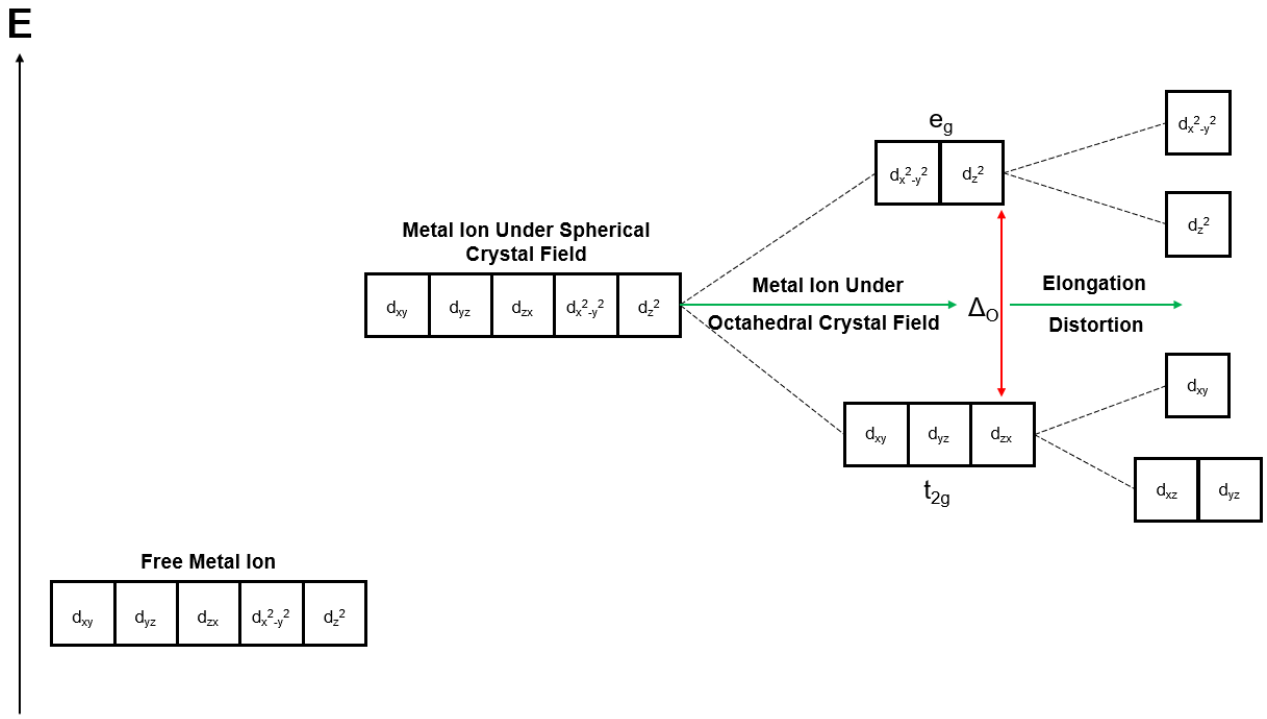

Figure 2.9. Illustration of elongation by Jahn-Teller distortion in the case of an octahedral complex.

For example, if one were to add an electron to a d^3 complex, there can be two possibilities: either the fourth electron can go to one of the empty higher energy e_g orbitals or pair with an opposite spin in the lower energy, half-filled t_{2g} orbitals as shown in Figure 2.10. However, to add an electron in the same exact orbital, an energy input called “spin pairing energy”, denoted by P, is required. [53] If the crystal field splitting energy, Δ_O, is greater than the spin pairing energy, P, the fourth electron will go to one of the half-filled t_{2g} orbitals; in the other case where $P > \Delta_O$, it will go to e_g as shown in Figure 2.10.

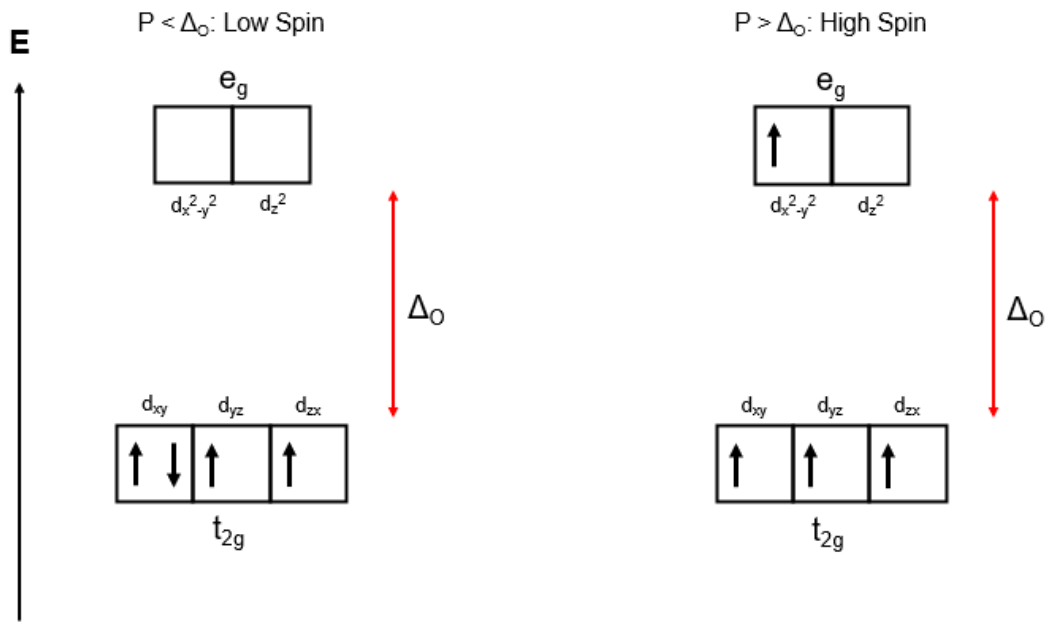

Figure 2.10. Illustration showing the effect of spin energy on the filling of orbitals.

The first case, where $P < \Delta_O$, allows for a minimum number of unpaired electrons and is labeled as a low-spin (LS) state, whereas the second case, where $P > \Delta_O$, allows for the maximum number of unpaired electrons and is called the high-spin (HS) state. The ligands strongly dictate the crystal field energy. A ligand is categorized as weak if it causes the central atom to have a large Δ_O and thus results in an LS state, while a strong field ligand results in an HS state due to a small Δ_O. In PBAs (M'-N≡C-M), low-spin and high-spin states are favored for M and M', respectively (N providing less crystal field splitting than C in the cyanide ligand). [54]

However, when the degenerate orbitals are unevenly filled, like the e_g orbitals in the high-spin state, it increases the energy of the system. So, to lower this energy, the once

degenerate orbitals undergo a reduction in symmetry by changing the relative lengths of axial and equatorial bonds that once were equidistant, causing distortion and volumetric changes in the crystal. The nature of metal-ligand orbital interactions strongly influences the extent of this distortion. Octahedral complexes can undergo either elongation or compression of axial bonds relative to the equatorial bonds to break the degeneracy of the orbitals and thus lower the energy of the system (see Figure 2.11).

In the case of elongation-induced Jahn Teller distortion, the degeneracy of orbitals is broken by lowering the energy of d orbitals with a z component, while the energy of orbitals without a z component is increased, i.e., they are made less stable. This is because orbitals without the z component have a greater degree of overlap with the ligands' orbitals, resulting in more repulsions and thus higher energy. It is the other way around in the case of compression-induced distortion, where orbitals with a z-component see an increase in energy.

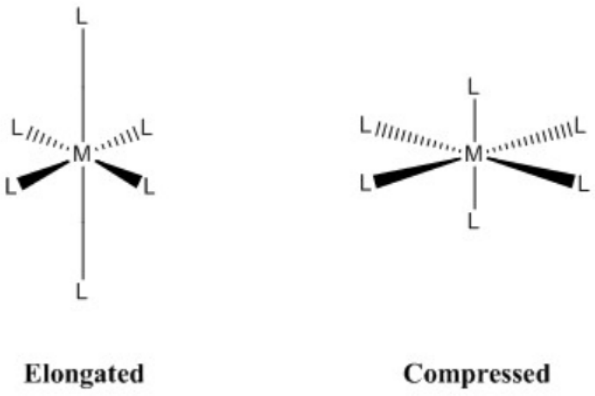

Figure 2.11. Types of Jahn-Teller distortions observed by the central atom in an octahedral complex. L represents the ligands that have covalent co-ordinate bonds with the central atom.

This phenomenon is expected for the Mn site in manganese hexacyanoferrate (when in +3 oxidation state to be precise), which is in the presence of a strong ligand (CN). In pristine (or reduced) MnHCF, Mn is in a 2+ oxidation state and the MnN_6 octahedra is symmetric with equidistant Mn-N shells. Upon removal of Na, Mn is oxidized to 3+ and the symmetry of the MnN_6 octahedra decreases, which leads to an Mn-N equatorial contraction (of about 10%) but without any changes to the axial Mn-N bonds (suggesting that Jahn-Teller distortion leads to basal shrinkage rather than axial elongation). [55] In other battery chemistries, similar distortions upon repeated charge and discharge cycles are sometimes ascribed as the reason behind capacity fade and failure modes such as particle cracking and transition metal dissolution. [56][49][57]

2.1.1.2. Understanding Manganese Hexacyanoferrate

The x in the formula $A_xM'[M(CN)_6]_{y\square 1-y}\cdot zH_2O$ represents the Na content and is typically between 0 and 2 in the fully charged and discharged states of a defect-free material, respectively, if two redox active transition metals are used. Cui and co-workers reported an anomalous analog, Na manganese hexacyanomanganate, $Na_xMn[Mn(CN)_6]$, where both C and N bonded sites, M and M', are occupied by Mn and x can be as high as 3. [58] This particular analog delivered a high reversible capacity of 209 mAh/g at a current density of 40 mA/g based on the three electron transfer reactions from $Na_3Mn^{II}[Mn^{I}(CN)_6]$ to $Na_0Mn^{III}[Mn^{III}(CN)_6]$ with three distinct plateaus visible at 1.8, 2.65 and 3.55 V vs. Na/Na^+. The third electron transfer reaction was suggested to result from the unusual oxidation state of +1 for the C-bonded Mn in the fully reduced state. Despite having such a high reversible capacity, the third Na in $Na_3Mn[Mn(CN)_6]$ was inserted electrochemically

(and not during synthesis), and its rather low average discharge voltage of 2.65 V compared to ~3.5 V for $Na_2Mn[Fe(CN)_6]$ only leads to a specific energy of 553.9 Wh/kg compared to the 590 Wh/kg for a defect free $Na_2Mn[Fe(CN)_6]$. Also, it can be speculated that $Na_3Mn[Mn(CN)_6]$ may have a shorter cycle life than $Na_2Mn[Fe(CN)_6]$ because of one more $Mn^{II/III}$ site that may experience Jahn-Teller distortion (if any), which makes MnHCF currently more appealing.

The highly reversible redox activity, abundance, and low cost of Fe made hexacyanoferrates (M'-N≡C-$Fe^{II/III}$) the preferred choice over their analogs for Na-ion cells. As stated before, hexacyanoferrates can have multiple electron transfer reactions, depending on the redox activity of the transition metal M' accessible in a given voltage window (see Table I for some representative analogs). For example, Mn or Fe reversibly change their oxidation state between +2 and +3 within 2-4 V vs. Na/Na^+, [46][34][49] while Ni is redox inactive and remains in the +2 oxidation state, hence allowing two and one electron transfer reactions in the same range, respectively. [59][60][61][29] In literature reports, it has been shown that PBAs with only one electron transfer reaction, like nickel hexacyanoferrate (NiHCF) and copper hexacyanoferrate (CuHCF), show significantly better capacity retention than PBAs with two-electron transfer reactions (MnHCF and FeHCF) despite operating between similar voltage limits. This comes at the expense of lower energy density, [61][62][63] which is roughly half for defect-free materials. The exact reason behind this discrepancy in capacity retention is still not completely understood. However, possible reasons include the near-zero strain nature of NiHCF and the absence of a Jahn-Teller center, compared to ~8% volume change for MnHCF. [64] Despite NiHCF

showing excellent C-rate performance and almost no capacity fade after thousands of cycles, [65][66] its rather low theoretical capacity of ~85 mAh/g and the use of a significant amount of Ni puts it at a disadvantage from an energy density and initial capital perspective.

Hence, manganese hexacyanoferrate (MnHCF) emerged as the most promising PBA positive electrode for Na-ion cells due to its relatively low cost, high capacity of ~171 mAh/g, and high discharge voltage of ~3.5 V (compared to ~3.2 V for FeHCF [67][46]). The theoretical active material energy density of ~590Wh/kg for MnHCF allows it to compete with LFP on a gravimetric basis with superior C-rate performance. [49] With further development of MnHCF, it can hopefully replace LFP in certain applications and help minimize the use of Li and Cu.

In 2015, Song and co-workers from the Goodenough group showed for the first time that a high reversible capacity of ~150 mAh/g and somewhat decent capacity retention of 75% after nearly 600 hours in Na half-cells is possible for MnHCF, which was unprecedented at the time. [34] They ascribed these gains in electrochemical performance to the removal of the interstitial water from the structure prior to cell fabrication by employing rigorous vacuum drying conditions. Earlier reports usually featured much lower capacities and poor capacity retention, which may have been due to the knowledge gap regarding the undesired escape of water into the electrolyte.

Since then, researchers have tried to implement different strategies to further increase

the performance of FeHCF and MnHCF in Na-ion cells. [68][69][32][70][71] Xu and co-workers synthesized MnHCF with a high reversible capacity of 160 mAh/g, however, it showed poor capacity retention (31% after 450 cycles with 5C charge-discharge in half-cells), which the authors ascribed to Mn dissolution and surface cracks as a consequence of structural instability arising from Jahn-Teller distortions at the Mn site. [49] The authors then employed a wet coating method to deposit 5 at. % Co on the surface, increasing the capacity retention to 81%. However, the use of Co is undesirable due to cost, toxicity, and scarcity (see Figure 1.2a). Cheng et al. showed benefits of introducing Cu as a dopant in $Na_{1.68}Fe_{0.92}Cu_{0.08}[Fe(CN)_6]_{0.86}\square_{0.14}\cdot 1.43H_2O$, which helped to access more capacity from the low-spin Fe redox site (107.9 vs. 127.4 mAh/g for non-doped and Cu-doped material, respectively). [72] Hu et al. synthesized a Ni-doped MnHCF material, $Na_{1.17}Ni_{0.1}Mn_{0.9}HCF$, showing capacity retention of 95% after 100 cycles in half-cells at a charge-discharge rate of 0.2 C. [64] The authors also saw higher ionic diffusivity by introducing Ni with 4.8 x 10^{-11} and 2.4 x 10^{-11} cm^2/s for sodiation, and 5.9 x 10^{-11} and 3.8 x 10^{-11} cm^2/s for de-sodiation in the case of $Na_{1.17}Ni_{0.1}Mn_{0.9}HCF$ and MnHCF, respectively. Gebert et al. employed a similar approach, where adding Ni to MnHCF resulted in a decent capacity retention of 96% after 500 cycles in half-cells at 0.8C, but their rather low specific capacity of 93 mAh/g at 100 mA/g, leaves room for improvement in terms of absolute capacity. [63]

In this study, the electrochemical performance of the synthesized products, NiHCF, MnHCF, and a Ni-doped MnHCF analog (abbreviated as $Ni_{0.03}Mn_{0.97}HCF$ based on stoichiometry) was evaluated (see Section 8). It is shown that decent capacity retention

of 80% and 95% for $Ni_{0.03}Mn_{0.97}HCF$ and NiHCF, respectively, after five months (more than 3500 hours) of testing in half coin cells with a reactive Na metal counter electrode can indeed be achieved. MnHCF showed a capacity retention of 70% after more than 2700 hours. To our knowledge, this is very competitive with current literature reports and commercial material, most likely a consequence of the optimized synthesis and processing conditions developed in this thesis (see Sections 5 and 6).

2.1.1.3. Water in Prussian Blue Analogs

One more issue that PBAs suffer from is their propensity to absorb water. The same open-framework structure that allows PBAs to sustain high current densities and long cycle life also makes them prone to absorbing moisture in the bulk during synthesis and processing, which can be as high as ~20 wt. %. [73][34][36] This could be tolerable if the moisture stays confined inside the crystal structure and does not escape into the organic electrolyte during cycling. However, if it does escape in significant quantities, it can react with fluorinated salt in the organic electrolyte to form HF (see Equation 6), which can cause the decomposition of passivation layers on the electrodes and the breakdown of solvent molecules, leading to a detrimental impact on cell performance.

$$NaPF_6 + H_2O \rightarrow NaF + 2HF + POF_3 \quad (6)$$

As mentioned before, three distinct types of water may be present in PBAs: surface, interstitial, and co-ordinated water. The first one, surface water, is relatively easy to remove by employing a 100-120 °C drying range. Interstitial water is more difficult to

remove and requires rigorous vacuum drying conditions usually at temperatures of ~170 °C for MnHCF or FeHCF. [44][35] The third type, so-called co-ordinated water, can exist in $M(CN)_6$ vacancies. It forms relatively strong co-ordinate bonds, a type of covalent bond where both electrons are provided by a single atom, with the transition metals in the structure (specifically M'), which makes it hard to remove even by vacuum drying.

Work by Wang et al. shows that co-ordinated water might be removed in the case of FeHCF by employing a 200-260 °C drying range based on their TGA analysis. [74] However, reports of possible structural damage and eventual collapse near 400 °C [75] set a limit for the drying temperature. While co-ordinated water may be hard to remove by drying, it has been reported to escape into the electrolyte during cycling to high states of charge (SOC). [50] It has been reported that the presence of considerable co-ordinated water can also restrict the redox activity of the N-bonded M site and thus lower the capacity even further [76] and lead to voltage polarization. [77] Therefore, synthesis optimization is key to minimizing vacancies and the associated risk of forming co-ordinated water in the first place. In the characterization part of this thesis (see Section 5.1), it is shown that synthesis optimization can help minimize vacancies, and by extension, the associated risk of forming co-ordinated water as verified by XRD and TGA.

PBAs show characteristic phases based on the sodium and water content present in them (see Table II). Monoclinic and rhombohedral phases are the favored synthesis products over cubic and tetragonal phases because of the high Na content, which is critical for a typical full-cell application with a Na-deficient negative electrode, where all the Na

inventory must come from the positive electrode, unlike in a half-cell where the Na counter electrode is a “near-infinite” reservoir of active Na. Upon charge (de-sodiation), the monoclinic or rhombohedral phases convert to the Na-poor cubic phase and finally to the tetragonal phase upon complete Na removal. However, the reversibility of the monoclinic phase is more nuanced with NiHCF and MnHCF showing vastly different behaviors.

Two consistent reports, by Song et al. and He et al., using ex-situ XRD showed that the monoclinic MnHCF converts to rhombohedral MnHCF during the initial cycle(s) by releasing water into the electrolyte. [34][44] Note that both phases have the same composition but different water content (see Table II). This indicates that MnHCF needs proper dehydration prior to cell fabrication due to its propensity to lose water at high SOC. Song and co-workers also reported better electrochemical performance for rhombohedral MnHCF than its monoclinic counterpart. Hence, some subsequent works focused on achieving and retaining the rhombohedral phase until fabrication in order to improve the electrochemical performance. [49][35]

An interesting observation was made by Song et al. when correlating the water content in MnHCF to the features in its voltage-capacity profile (see Figure 2.12). The hydrated monoclinic phase showed two distinct charge/discharge plateaus at ~3.5/3.2 and ~3.8/3.5 V vs. Na/Na^{+}, which were ascribed to the $Fe^{II \rightleftharpoons III}$ and $Mn^{II \rightleftharpoons III}$ redox couples, respectively. Interestingly, upon vacuum drying (or release of interstitial water during cycling), the two plateaus merged into one. The presence of only one plateau instead of two indicates possibly different responses of Mn−N and Fe−C interactions to the degree of the rotation

of the linear $(C\equiv N)^-$ anions from the Mn···Fe axes upon phase change from monoclinic rhombohedral. [34]

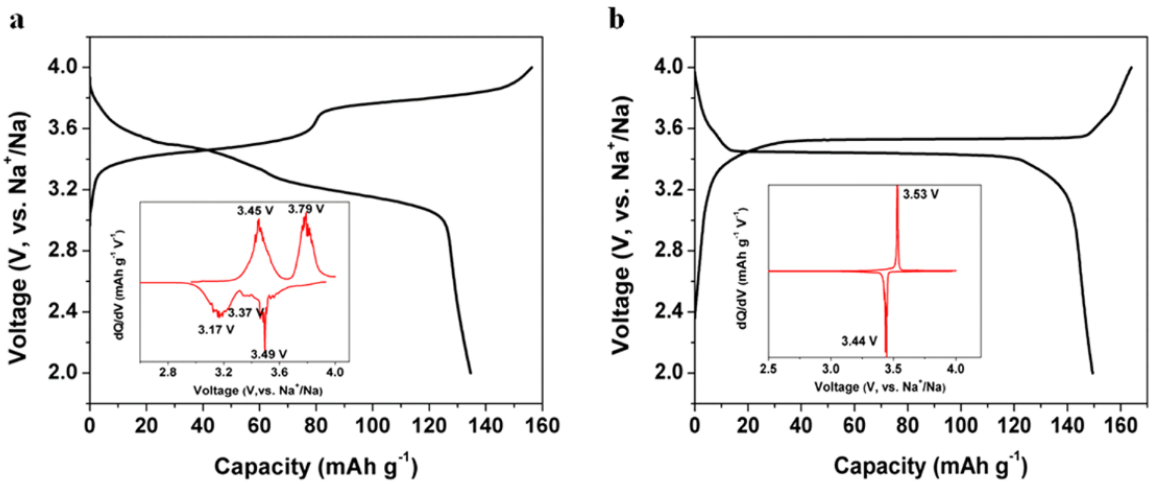

Figure 2.12. Initial voltage-capacity profiles for (a) monoclinic and (b) rhombohedral MnHCF at a current density of 15 mA/g in the voltage range of 2.0−4.0 V vs. Na/Na^+. Figure retrieved from work by Song et al. (2015), published in *Journal of American Chemical Society* (DOI: 10.1021/ja512383b). [34]

Generally, ionization energy can be treated as a proxy for comparing the ease of change in oxidation number. For example, the standard ionization energies of $Fe^{II\rightleftharpoons III}$ and $Mn^{II\rightleftharpoons III}$ are 2957 and 3248 kJ/mol, respectively. This tells that oxidizing Mn^{II} is expected to be less favorable (or that it changes oxidation state at higher potential) than Fe^{II} and is in agreement with other SIB and LIB positive electrode reports, where X-ray photoelectron microscopy (XPS) was employed to characterize the Fe and Mn oxidation states at different SOCs of a cell. [78][79] Wu and co-workers employed soft X-ray absorption spectroscopy and theoretical calculations to further deconvolute this behavior in the context of hydrated and dehydrated MnHCF. [80] They proposed that the well-segregated

spin states of Fe and Mn (low-spin state for C-bonded Fe and high-spin state for N-bonded Mn) in the MnHCF system have different ligand field stabilization energy (LFSE), with $Fe^{II \rightleftharpoons III}$ having greater LFSE than $Mn^{II \rightleftharpoons III}$, which increases the redox potential of $Fe^{II \rightleftharpoons III}$. However, this competes directly with the ionization energy differences (Mn having a greater one than Fe). Hence, the net result is just one plateau in the voltage-capacity profile with the two factors possibly canceling each other out when no water is present (see Figure 2.13).

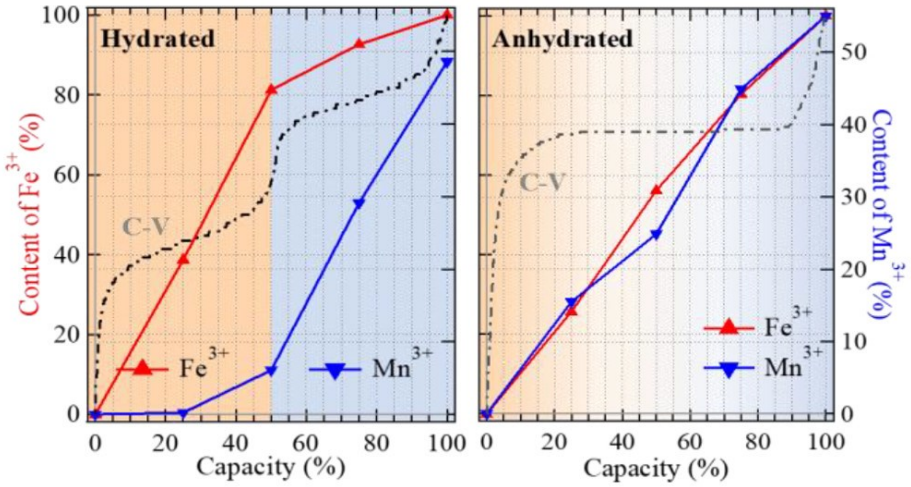

Figure 2.13. The concentration of the oxidation states of Fe^{3+} and Mn^{3+} upon electrochemical potentials for hydrated (monoclinic MnHCF) and de-hydrated MnHCF (rhombohedral MnHCF). Figure retrieved from work by Wu et al. (2017), published in *Journal of Royal Chemistry* (DOI: 10.1021/jacs.7b10460). [80]

Wu and co-workers proposed that a significant amount of water present inside the crystal structure diminishes the LFSE and hence, two separate plateaus in the voltage-capacity profile are visible for the hydrated MnHCF. Based on the above set of arguments, the redox energies of Mn and Fe for the monoclinic and rhombohedral phases of MnHCF can

be visualized in Figure 2.14. As shown, the redox $Fe^{II \rightleftharpoons III}$ and $Mn^{II \rightleftharpoons III}$ are segregated when considerable water is present in the structure (i.e., in the monoclinic phase), giving rise to two discharge plateaus at ~3.17 and 3.49 V vs. Na/Na^+, respectively, where the effect from the reduction potentials of the metals is dominant in absence of LFSE effects. Whereas in the case of the dehydrated MnHCF (i.e., the rhombohedral phase), the LFSE and the effects of reduction potentials cancel each other out, giving rise to only one energy level around 3.45 V.

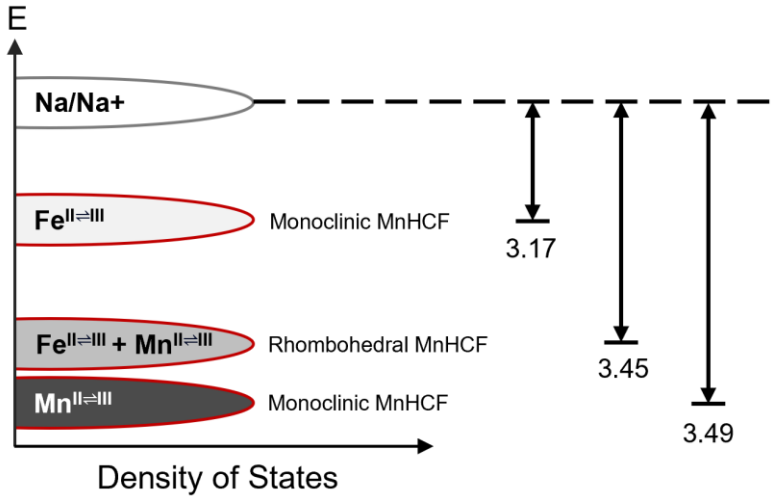

Figure 2.14. Suggested energy bands for iron and manganese in monoclinic, i.e., hydrated, and rhombohedral, i.e., dehydrated, MnHCF.

NiHCF synthesis reports show that it faces similar issues of having considerable water content. As shown by XRD analysis, Na-rich NiHCF similarly exhibits a monoclinic phase while Na-poor NiHCF is cubic. [81] Interestingly, during cycling, unlike MnHCF, it has been shown to undergo only the monoclinic to cubic phase transformation which is highly reversible and promotes long cycle life. [81][73] The fact that the monoclinic-to-cubic phase

transition does not convert to a rhombohedral-to-cubic phase transition during cycling may be an indication that water removal is more difficult for this material (see discussion in Section 6).

2.2. Negative Electrode Active Materials

An ideal negative electrode active material should possess a low oxidation/reduction potential versus the positive electrode and a high capacity in order to enable high energy density at the full-cell level (see Equation 4). However, the negative electrode potential has to be somewhat higher than 0 V vs. Li/Li^+ (or Na/Na^+) in order to avoid plating of the mobile ion on the particle surface, which can lead to dendrite-like structures that can pierce the insulating separator and cause thermal runaway event.

Graphite has been the most popular negative electrode material for Li-ion cells since their commercialization by Sony (Japan) in 1991. [82] This is mainly due to the decent capacity and long lifetime achieved through decades of research. Graphite is a crystalline compound, formed by periodic stacking of graphene layers. Graphite used in modern-day Li-ion cells can be either natural or synthetic (also called artificial). Natural graphite needs to be mined and processed whereas synthetic graphite is obtained by heating coal-based or petroleum-based precursors at a temperature of 2700 °C or higher. [83] Upon Li intercalation, the graphene layers undergo expansion and form three intermediate phases or "stages" (LiC_{72}, LiC_{36}, and LiC_{12}) in series before reaching the final intercalation compound LiC_6 (see Figure 2.15). This exact stoichiometry of the final compound determined the theoretical specific capacity, which is 372 mAh/g for a defect-free

structure. The four stages can be correlated to the four plateaus in the voltage-capacity profile of a Li-graphite half-cell (see Figure 2.15). Potassium, a much bigger atom than Li and Na, is reported to form a stage-1 KC_8 intercalation compound, giving rise to a theoretical specific capacity of 279 mAh/g. [84] Interestingly, Na does not intercalate into graphite even though its ionic radius is between that of Li and K. This tells us that other factors apart from size are at play that influence the electrochemical performance of graphite.

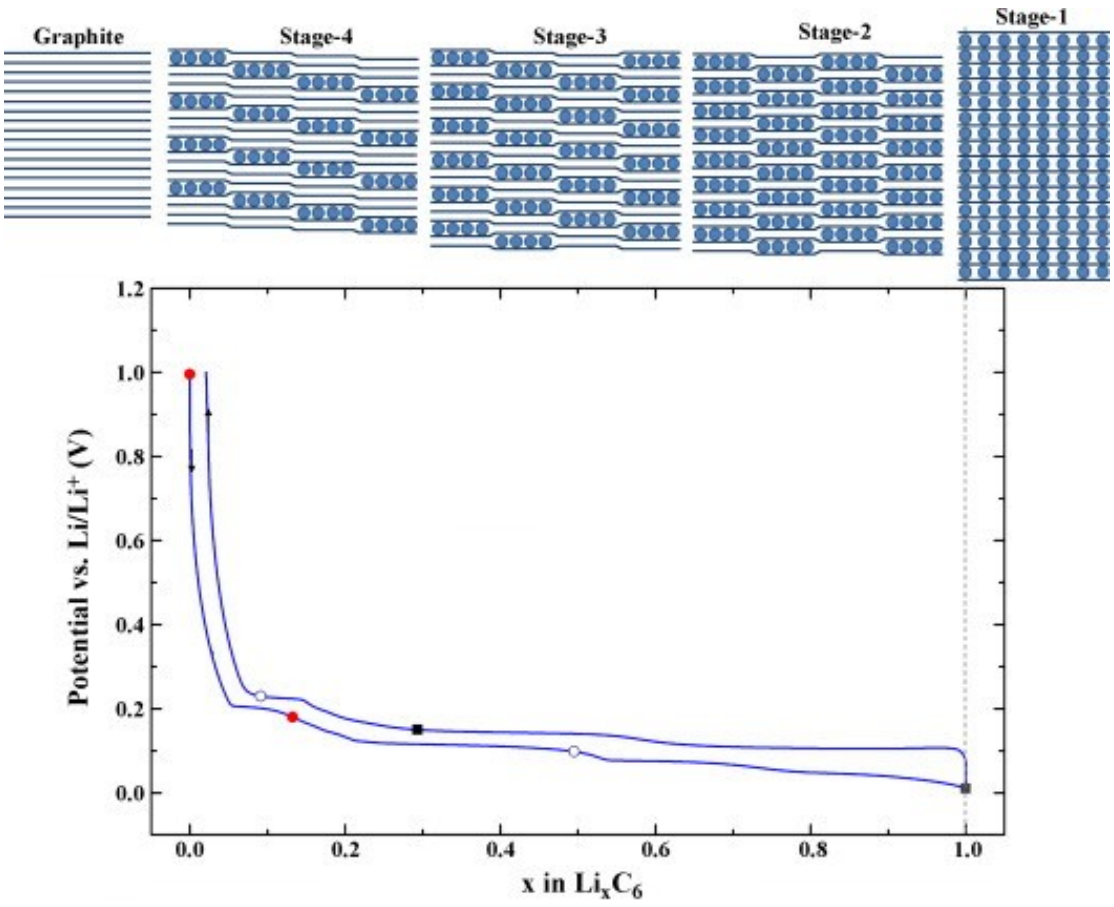

Figure 2.15. Voltage-capacity plot for Li-graphite half-cell and a schematic (top) showing different LiC_x stage compounds. Figure retrieved from work by Sethuraman et al. (2010) with permission, published in *Journal of Power Sources* (DOI: 10.1016/j.jpowsour.2009.12.034). [85]

Moriwakke and co-workers, in their 2017 work, argued that this anomaly of Na arises mainly because of less negative (i.e., less stable) formation energies (see Figure 2.16). [86] Their DFT study suggests that the tendency of alkali metals to form stable intercalation compounds with graphite increases down the periodic column (from Na to Cs) and that it is Li that is the exception rather than Na. They argued that the formation energy of Li-graphite intercalation compounds is more favorable than that of their Na counterparts because the former also benefit from some covalent interactions and van der Waal's attraction between graphene layers (due to rather limited expansion of graphene layers because of the smaller size of Li), whereas Na and the other bigger alkali atoms only rely on ionic interactions. The van der Waal's attraction between graphene layers is diminished for bigger atoms due to increased interlayer spacing upon insertion.

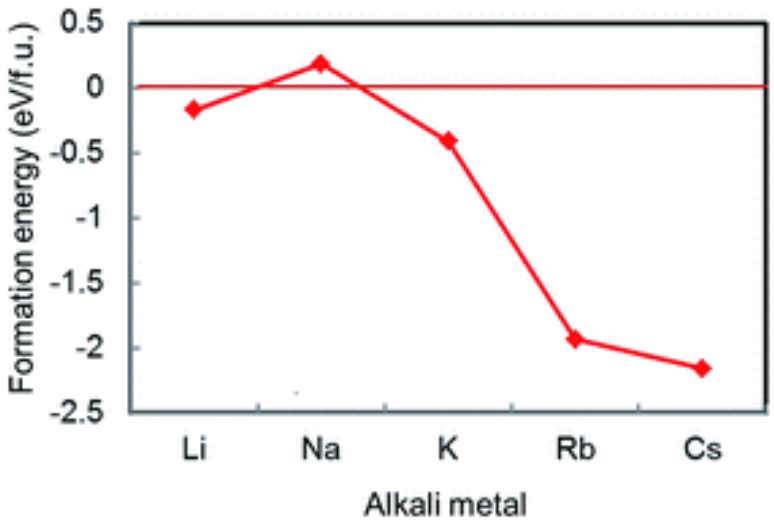

Figure 2.16. Formation energies of AMC_6 for AM = Li, Na, K, Rb, and Cs in order of increasing atomic number based on DFT calculations. Figure retrieved from work by Moriwakke et al. (2017), published in *Royal Society of Chemistry Advances* (DOI: 10.1039/C7RA06777A). [87]

In 2000, Dahn and Stevens discovered hard carbon (HC) as a competitive and practical negative electrode active material for Na-ion batteries, showing a specific capacity of 300 mAh/g which is close to the 372 mAh/g for LiC_6. [88] Since then, many different particle engineering and synthesis routes have been explored, with Kamiyama and co-workers from the Komaba group demonstrating specific capacities as high as 478 mAh/g. [89] Hard carbons are mostly amorphous in nature and composed of pores with different size, as well as some graphitic domains. This gives rise to more than one type of storage mechanism, unlike graphite where all ion storage happens by the intercalation principle (see Figure 2.17).

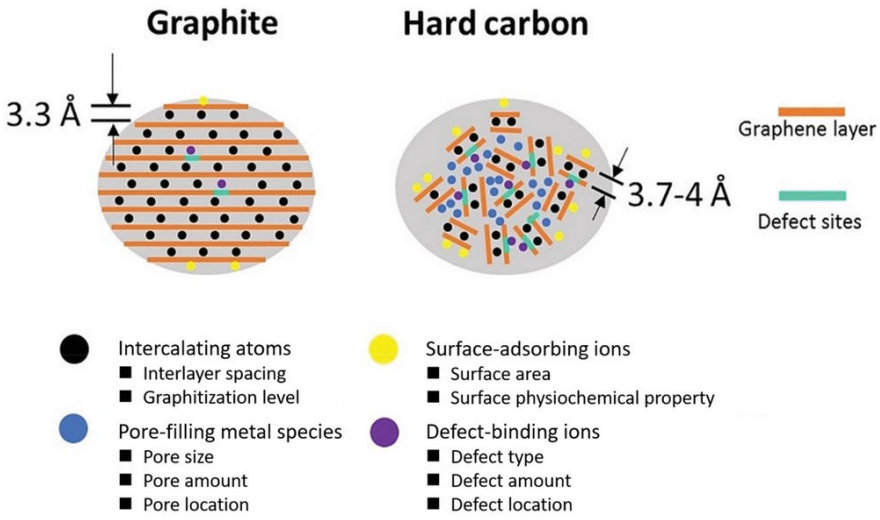

Figure 2.17. Schematic illustration of the differences in ion storage between graphite and hard carbon. Figure retrieved from work by Xiao et al. (2018), published in *Chemistry-Sustainability-Energy-Materials* (DOI: 10.1002/cssc.201801879). [90]

The voltage capacity profiles for hard carbons show two distinct features, a plateau, and a sloping region (see Figure 2.18), due to the presence of more than one storage mechanism. Stevens and Dahn showed that the capacities of the sloping region and the low voltage plateau are from Na insertion between the graphene layers and pore-filling, respectively. [91][91] However, some reports also suggest alternative mechanisms. [92][93][94]

Two commercial hard carbons were evaluated in this study; their physical properties are summarized in Table III. The particle size of both materials was similar, with D_{50} values of 9.72 and 10.20 μm, respectively (as verified by laser particle size analyzer, LA-950 from Horiba, Japan). The interlayer spacing in these hard carbons is about 0.382 nm, greater than the commonly reported 0.335 nm in commercial graphite for Li intercalation [95] and is most likely engineered to facilitate faster movement of bigger Na atoms.

Table III. Physical properties of commercial hard carbons used in this study.

Property	**Type I**	**Type II**
Particle Size (D_{50}) [μm]*	9.72	10.20
Specific Surface Area [m^2/g]**	4	7
Interlayer Spacing d_{002} [nm]**	0.382	0.382

*) Refractive indices used for water and hard carbon were 1.33 and 1.92, respectively.

**) Values provided by vendor.

It is interesting to see that both hard carbons show identical capacities for Na storage (see Figure 2.18b), but quite different capacities for Li storage (see Figure 2.18a). This may be due to a greater number of smaller-sized pores present in Type I than in Type II which may be small enough for Li diffusion but not for Na diffusion (evident by different surface areas). The Brunauer-Emmett-Teller (BET) technique can be used to measure the pore size distribution of HCs by adsorbing gaseous molecules of different sizes like nitrogen, argon, carbon dioxide, and water vapor. This can be used to identify and later engineer pores to maximize Li and Na storage capacities.

Currently, HC is the most popular negative electrode active material for SIBs, mainly because of the low-cost precursor materials, e.g., coconut shells, corn, cellulose etc., [96] and relatively long cycle life. [97][98] However, due to its amorphous nature, it has a rather low density (typically ~1 g/cc or less), which makes it challenging to achieve a high volumetric energy density at the cell level. However, for ESS applications, this can be acceptable if production costs can be lowered further, such that the metrics like cost per unit of energy ($/kWh) and cost per cycle ($/kWh·cycle) become competitive. For Na-ion cells with higher energy density requirements, such as for standard range EVs, alloy negative electrode materials (like Pb, Sn, and P) have recently been explored. [99][100][101] These alloy materials can potentially lead to Na-ion cells with higher volumetric energy density than LFP-based Li-ion cells, but need further improvements and validation in full-cells before they can be competitive with hard carbon systems in terms of lifetime. [20]

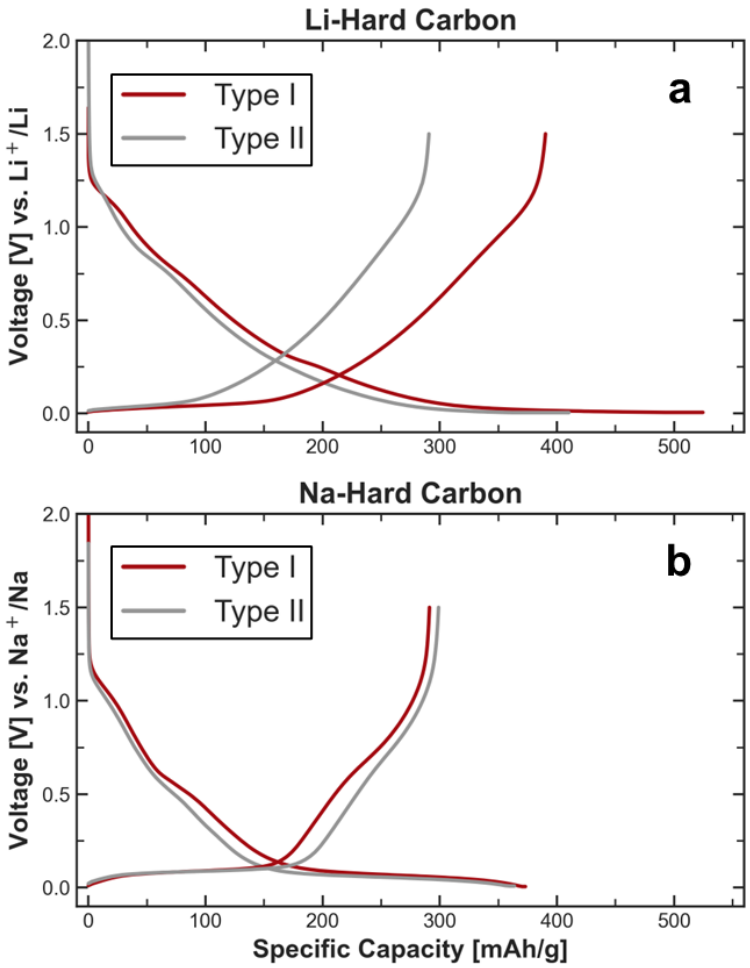

Figure 2.18. Voltage-capacity profiles rate for two different types of hard carbon half-cells paired with (a) Li and (b) Na counter electrodes for a C/20. The cells were cycled at 30 °C using a C/20 rate between 5 mV and 1.5 V vs. (a) Na/Na^+ and Li/Li^+. The C-rate was calculated based on a specific capacity of 330 mAh/g for both. Na and Li half-cells were assembled with 1 M $NaPF_6$ and 1 M $LiPF_6$ in EC:DEC 1:1, respectively. D_{50} for Type I and Type II hard carbons is 9.72 and 10.2 μm, respectively, as verified by a particle size analyzer.

2.3. Electrolytes

The electrolyte inside a Li- or Na-ion cell serves as a medium through which the transport of Li^+ or Na^+ ions is facilitated during the charge and discharge processes. Most common

liquid electrolytes use a combination of linear and cyclic alkyl carbonates to gain synergistic benefits. Usually, linear carbonates, like dimethyl carbonate (DMC) and diethyl carbonate (DEC), provide sufficient “wetting” of the porous electrodes and relatively high ion mobility due to their low viscosity, while cyclic carbonates, like polypropylene carbonate (PC) and ethylene carbonate (EC), increase the solubility of Li and Na salts due to their relatively high dielectric constants. The physical properties of some common solvents are listed in Table IV. The electrolyte solvents have to be selected with their melting points and boiling points in mind, to ensure wide temperature operation.

The electrolyte salt concentration is usually ~0.8-1.2 M which leads to the highest ionic conductivity. Some commonly used Li salts are lithium hexafluorophosphate ($LiPF_6$) and lithium bis(fluorosulfonyl)imide (LiFSI). Their Na analogs are commonly employed in Na-ion cells. The ~300-mV difference between the standard reduction potential of Li and Na (-3 V vs. SHE for Li/Li^+ and -2.7 V vs. SHE for Na/Na^+, respectively) represents an additional challenge for electrolyte optimization in Na-ion cells, especially for high voltage operation.

PC received attention during the early phase of research on Li-based cells due to its high dielectric constant, excellent low-temperature performance, and wide electrochemical stability window. However, when used in large amounts, PC causes the unwanted exfoliation of the graphite negative electrode due to its co-intercalation and subsequent electrochemical decomposition.

Table IV. Physical properties of some common electrolyte solvents used in Li- and Na-ion cells. [102]

Solvent	**Melting Point** [°C]	**Boiling Point** [°C]	**Dielectric Constant** [F/m]	**Viscosity** (@25°C) [mPa·s]
DMC	2.4	90	3.12	0.585
DEC	-43	126	2.82	0.748
EC	36.4	248	89.78	-
PC	-48.8	242	66.14	2.53

Fortunately, the discovery of another cyclic carbonate, EC, and its passivating properties for the graphite negative electrode in Li-ion cells by Dahn and co-workers in 1990 [103] made PC mostly obsolete for LIBs. For SIBs, PC has remained a popular solvent in the research community [104][105] since HC lacks the long-range layer order of stacked graphene sheets and thus only offers a minimal chance for exfoliation. All cells fabricated as a part of this study used PC as the main electrolyte solvent unless stated otherwise.

The highly oxidizing and reducing environments at the electrodes cause the decomposition of organic electrolytes, especially during the initial cycles, leading to the formation of films on the surfaces. These films passivate the particles and ideally prevent subsequent decomposition of the electrolyte by serving as a protective layer. These films can be thought of as an interphase between the solid electrode particles and the liquid electrolyte and hence are also referred to as a solid-liquid electrolyte interphase or SEI. At the negative electrode of a cell, reduction of electrolyte takes place during the initial

cycles upon which Na atoms irreversibly react with salt and solvent molecules to form products like NaF and Na_2CO_3. Since these decomposition products consume the available Na that otherwise would have contributed to the desired redox reactions, also called Na inventory, it reduces the usable capacity of a cell. Hence, the first cycle efficiency of a cell is crucial as it generally dictates the accessible capacity throughout the lifetime of a cell. An ideal SEI at the negative electrode should be robust enough to prevent subsequent Na inventory loss, while being ionically conducting but electronically insulating. In a dynamic cell, the SEI at the negative electrode keeps on evolving and thickening which can lead to an increased charge transfer resistance. Most electrolytes also comprise of certain additives to further augment the performance of cells like suppressing gas generation or lowering the cell resistance. Some additives explored in academic research for SIBs include prop-1-ene-1,3-sultone (PES), sodium difluorophosphate (NFO), and vinylene carbonate (VC). [20] On the positive electrode side, oxidation of electrolyte is more pronounced and can follow electrochemical or chemical pathways. Chemical oxidation is common in layered oxide positive electrodes, where oxygen can escape the crystal at higher states of charge. [106] The decomposition products of these oxidation reactions include gaseous products like (H_2O, CO, and CO_2) which pose the risks of swelling and rupturing of cell casings.

The presence of any water in the electrolyte can react with salt to corrosive hydrofluoric acid (HF), as shown previously in Equation 6. HF can cause the decomposition of carbonate molecules, as well as corrosion of electrodes, which leads to detrimental

effects on the performance of the cell (especially at high temperatures). [107] Hence, proper dehydration of cell parts is necessary before electrolyte filling.

Chapter 3. Experimental Methods for Materials Characterization

3.1. X-ray Diffraction (XRD)

X-ray diffraction is a widely used non-destructive technique for analyzing the structure of materials at the atomic level, and is mostly employed for studying crystalline materials, i.e., materials possessing long-range order. After X-rays from the emitter, usually a Cu source, encounter a 3D atomic arrangement of the sample, they are diffracted in a different direction than the original incoming beam and are collected using a detector (see Figure 3.1). The angle between the original and diffracted beams is called the diffraction angle and is denoted by 2-theta (2Θ). X-rays with a wavelength similar to the interatomic distances in the crystalline materials (nanometer scale) are used so that the arrangement of atoms inside the sample can influence diffraction behavior, i.e., promote the relative constructive or destructive interferences and affect the angle of diffraction. The majority of the diffraction beams will undergo destructive interference, i.e., diffracted waves canceling each other out, while some constructive interference is expected for crystallite samples when the wavelengths of diffracted waves are a whole number multiple (n) of the incoming wavelength (λ).

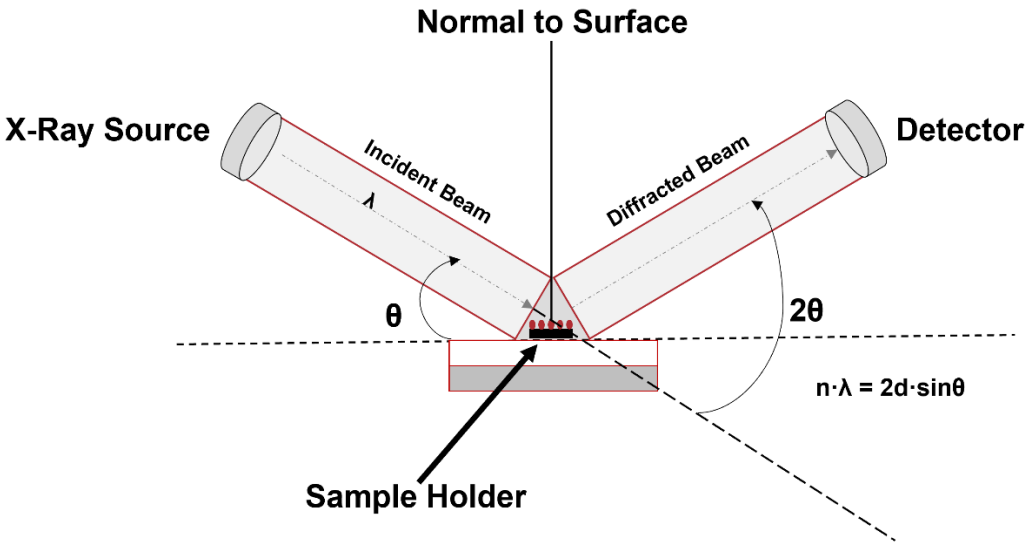

Figure 3.1. Schematic of primary components and working principle of an x-ray diffractometer.

So, if a high intensity is detected at a specific diffraction angle, it is due to the high periodicity of parallel atomic planes in that direction. By using Bragg's law (see Equation 7), the diffraction angle theta allows to calculate the distance (d) between the two parallel planes.

$$\sin\Theta = \frac{n\lambda}{2d} \tag{7}$$

Crystals can be thought of as being made up of small repeating constituents, called unit cells. Miller indices (hkl) are used to identify a plane (or parallel planes) that intersect the unit cell. They are used to define directions and distances within the crystal. A plane of atoms with Miller indices (hkl) can be visualized as a plane intersecting the unit cell at intercepts a/h, b/k, and c/l, respectively, where a, b, and c are the edge lengths of the unit

cell in x, y, and z direction, respectively. Based on the symmetry operations of unit cells, 230 distinct space groups exist. Based on the relative lengths of edges (a, b, and c) and the angles between them (α, β, and ɣ), 3D unit cells can be divided into seven crystal systems, which are summarized in Table V.

Table V. Lattice parameters for the seven 3D crystal systems.

Crystal System	**Edge Length(s)**	**Angles***
Cubic	a = b = c	α = β = ɣ = 90°
Tetragonal	a = b ≠ c	α = β = ɣ = 90°
Hexagonal	a = b ≠ c	α = β = 90°, ɣ = 120°
Rhombohedral	a = b = c	α = β = ɣ ≠ 90°
Orthorhombic	a ≠ b ≠ c	α = β = ɣ = 90°
Monoclinic	a ≠ b ≠ c	α = 90°, β ≠ 90°, ɣ = 90°
Triclinic	a ≠ b ≠ c	α ≠ β ≠ ɣ ≠ 90°

*) α, β, and ɣ are the angles between b and c, between a and c, and between a and b, respectively.

After finding the interplanar spacing (d) from Bragg's law (from Equation 7), unit cell parameters for each crystal system can be calculated using their respective geometric expressions. Such expressions for some crystal systems are shown below: -

Cubic: $1/d^2 = (h^2 + k^2 + l^2) / a^2$

Tetragonal: $1/d^2 = (h^2 + k^2) / a^2 + l^2 / c^2$

Hexagonal: $1/d^2 = 4 (h^2 + hk + k^2) / 3a^2 + l^2 / c^2$

Orthorhombic: $1/d^2 = h^2 / a^2 + k^2 / b^2 + l^2 / c^2$

Monoclinic: $1/d^2 = h^2 / (a^2 \sin^2 \beta) + k^2 / b^2 + l^2 / (c^2 \sin^2 \beta) - 2 hl \cos \beta / (ac \sin^2 \beta)$

After substituting a set of possible values of h, k, and l in the above expressions alongside the d spacing (from Equation 7), unit cell parameters can be calculated. For indexing peaks of a diffraction pattern, the reverse process is followed. Using a known d value, a possible combination of h, k, and l values is tested such that the above expressions are satisfied. However, indexing is particularly challenging to do manually as it may require significant trial and error attempts. This can be especially challenging for systems with lower symmetry whose general expressions are more complicated (like rhombohedral and triclinic), and one can rely on software like GSAS, [108] Vesta, [109] and Match [110] for indexing.

Distinct phases with the same or different molecular formula but a different arrangement of atoms in a unit cell can exist due to changes in external factors like temperature and pressure, as well as synthesis conditions. Solid-solid phase transformations can be of two types: first-order, where reconstruction occurs in a discontinuous way, and second-order, where there is a gradual change and a continuum is maintained, i.e., characteristic peaks are still related. XRD can be useful when evaluating first-order phase transformations, but structural information gained from refinement obtained for one phase cannot be used for

the other phase due to the vast differences in crystal structures of both phases. However, in the case of a second-order phase transformation, unit cells are often related since the complete reconstruction of the crystal does not take place (unlike for first-order) and mainly only the space-group symmetry changes. To check if a reaction is of a second-order type, diffraction patterns before and after can be compared, and if they share a similar blueprint of patterns, it gives an indication of whether the unit cells are related. An example of a second-order solid-to-solid phase transformation can include the transformation from cubic to rhombohedral in Figure 3.2, where both are related. This is of particular importance for the Prussian Blue Analogs studied in this thesis, which undergo such second-order phase transitions upon change in water or sodium content (charge or discharge).

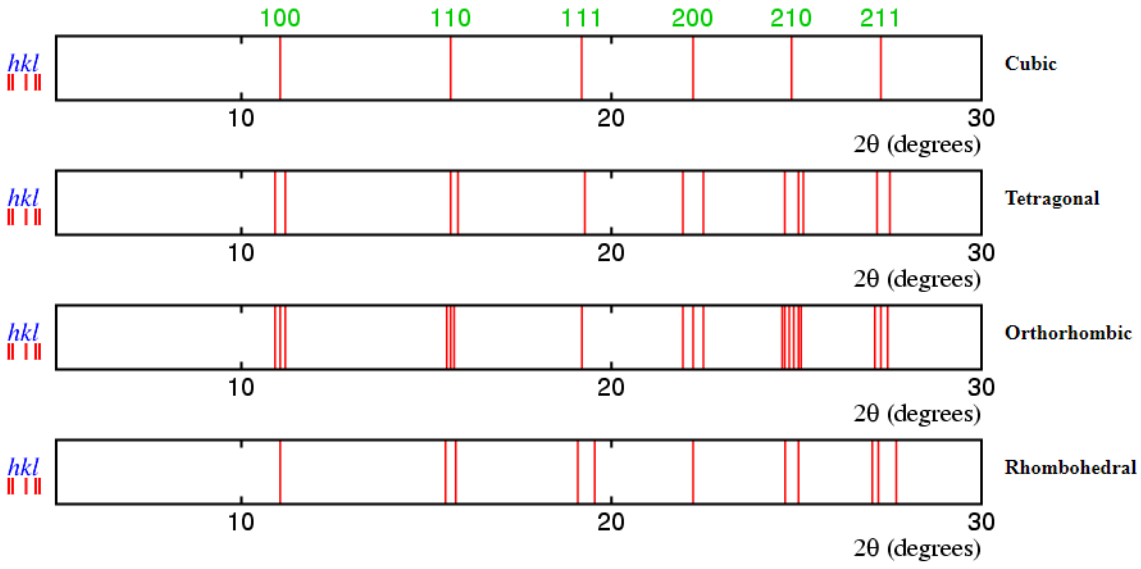

Figure 3.2. Possible diffraction lines for a cubic material with an 8 Å unit cell, as well as other phases that it undergoes upon physical changes to the material. Figure retrieved from online powder diffraction course by Cockcroft and Barnes from Birkbeck College, University of London. [111]

In the example shown in Figure 3.2, cubic and rhombohedral patterns share the same blueprint pattern, i.e., diffraction peaks are found at similar angles, but with some splitting (or non-splitting). The splitting (or non-splitting) can be explained by the symmetries of the unit cells. The body diagonal changes when going from cubic ($a = b = c$ and $\alpha = \beta = \gamma = 90°$) to rhombohedral ($a = b = c$ and $\alpha \neq \beta \neq \gamma \neq 90°$), causing the 111 cubic peak to split into two peaks since there are two different body diagonal lengths for the latter unit cell.

In battery research, XRD is often used to characterize active materials, especially positive electrode materials upon synthesis, to check for the desired phase and the presence of potential impurities. XRD can also be used to analyze active materials post-cycling to investigate structural changes or identify the formation of new phases and correlate them to the performance of the battery cells.

In this study, XRD characterization was carried out using a Bruker D8 diffractometer that employed a Cu-target X-ray source. Measurements were recorded with a resolution of 0.02° (spending 3 seconds at each step), with data being collected in the 10–70° two theta range. For the dehydrated samples, a custom-built air-tight holder was used, with sample preparation being carried out inside an Ar-filled glovebox to minimize phase changes arising from moisture uptake.

3.2. Thermogravimetric Analysis (TGA)

Thermogravimetric analysis (TGA) is a technique employed to study the mass change of a sample as a function of temperature and time. The instrument has a very high precision balance, able to detect even tiny mass changes. The instrument records the initial weight, after which the temperature is ramped up according to a user-defined protocol. The protocol can involve a constant heating rate, e.g., 5 °C/min, until a fixed upper limit is reached, or it may be programmed to spend a specific amount of time at the temperature point(s) of interest. A carrier gas like argon is used to purge the gaseous decomposition products that account for weight reduction away from the sample (see Figure 3.3).

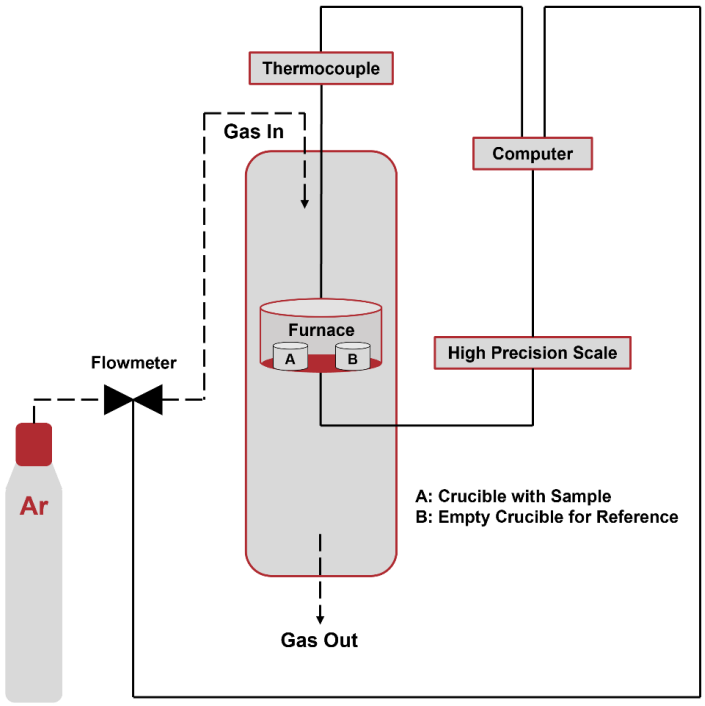

Figure 3.3. Schematic of primary components and the working principle of TGA instrument.

The outlet stream of the carrier gas can be coupled with a mass spectrometer for the identification of the gaseous byproducts which can be useful to uncover the reaction pathways triggered by thermal decomposition. Alternatively, a TGA instrument can also be programmed to record the weight increase of a sample as a function of time, usually from a reaction with ambient air after drying. TGA was particularly utilitarian in this study to help quantify the water content present in different PBAs after different processing conditions.

In this study, TGA analysis was performed on an SDT-Q600 (TA Instruments, USA) mainly with the goal of quantifying the moisture content of the as-synthesized or vacuum-dried PBA samples. For each run, ~10 mg of powder was used. The heating protocol consisted of a constant 5 °C per minute ramp to 400 °C. Argon was used as the carrier gas with a flow rate of 100 standard cubic centimeters per minute (SCCM). For the dehydrated samples, there was a 1–2-minute exposure while transferring the samples from the oven to the TGA instrument, and hence the actual water content was slightly higher than expected. All mass changes were normalized to the mass recorded before heating.

3.3. Scanning Electron Microscopy (SEM) and Energy Dispersive X-Ray Spectroscopy (EDS)

Scanning electron microscopy (SEM) is a common technique for imaging the morphology and topology of micron and nanosized materials. An electron beam is generated

thermionically from the cathode, e.g., a tungsten filament heated under vacuum to emit electrons, also called an electron gun, and is accelerated towards the anode (see Figure 3.4). Usually, tungsten is chosen because of its low cost and high melting point. After an external voltage is applied, the beam travels through a series of lenses and apertures before hitting the sample to produce high-resolution images. After the collision with the sample, backscattered electrons are reflected back due to the elastic interactions. Whereas secondary electrons are generated from the atoms present in the sample and are due to inelastic interactions. Both backscattered and secondary electrons convey different types of information about the sample.

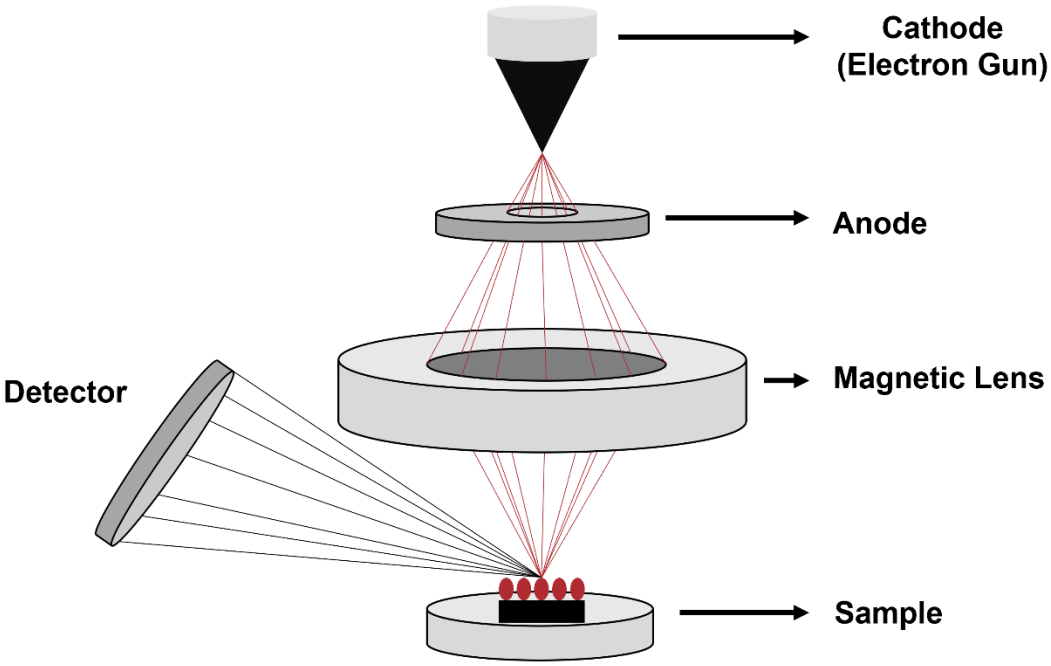

Figure 3.4. Schematic of primary components and the working principle of a SEM.

For example, the backscattered electrons can provide rich information about the surface and morphology since they cannot penetrate deep into the material. Whereas secondary

electrons come from deeper sections of the sample and can be used to distinguish between elements of different atomic numbers.

After the excitation of electrons, holes are left behind in the lower principal shell. Post-excitation, secondary electrons return to the lower principal shell to fill these holes and photons in the form of characteristic X-rays are generated during this process which are element specific. Most modern-day SEMs are paired with an energy-dispersive X-ray spectroscopy (EDS) detector that can detect these X-rays and assign them to specific elements based on the characteristic X-ray energies for electron transitions in the different elements. The elemental identification based on EDS can be overlayed with sample images from SEM to generate “EDS maps”, showing the distribution of elements within the sample (see Section 5.1. for examples).

In this study, SEM images were taken of as-synthesized PBA samples using a Thermo Scientific Axia ChemiSEM instrument (USA) with a tungsten filament and an EDS detector at an accelerating voltage of 5 kV. Powders were sprinkled on carbon tape (Nisshin Em Co., Japan) on a standard 0.5” SEM sample stub as a part of sample preparation.

3.4. Inductively Coupled Plasma Optical Emission Spectroscopy (ICP-OES)

ICP-OES is an analytical technique used to quantify the atomic composition of a sample.

It can be employed to detect trace amounts of certain elements (mostly metals) in a sample and is a preferred technique for determining the bulk composition of a material over techniques like EDS that are surface sensitive. The working principle of ICP-OES exploits the fact that different atoms absorb different amounts of energy to excite electrons from the ground state to higher energy bands (also referred to as excited states). Upon thermal decomposition of the material of interest by the energy input from a high-temperature plasma, electrons in the various atoms overcome inertia and go from local minima to higher energy bands (see E_1, E_2, E_3, etc. in Figure 3.5). The energy input required for an electron to travel between two different energy bands is fixed. As seen in Figure 3.5, an energy input equivalent to 283.3 nm is required for an electron in the lead (Pb) atom to go from the ground state to the first excited state, with higher energy (or lower wavelength) required for the subsequent higher excitations.

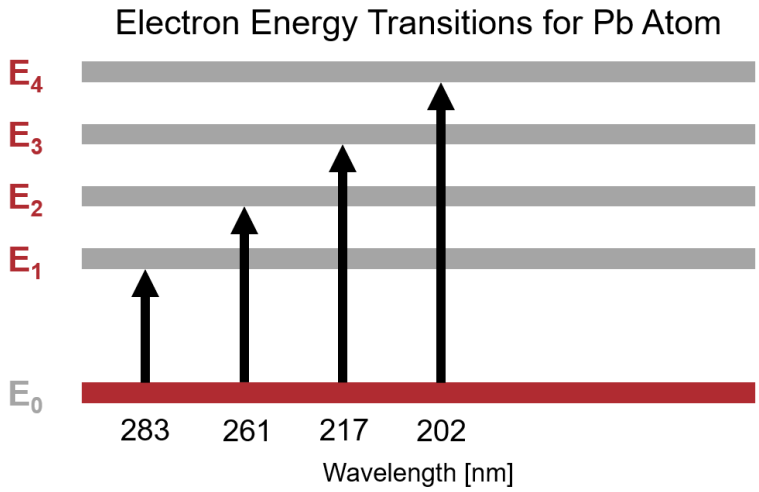

Figure 3.5. Energy level diagram for lead (Pb) atom.

After the excitation by the high-temperature plasma, electrons emit the same energy or

characteristic wavelengths in the process of transitioning back to the ground state (E_0). Using the Beer-Lambert law, one can then quantify the intensity of light at these wavelengths and determine the relative amounts of elements present in the sample.

An ICP-OES instrument consists of four major parts: the sample introduction chamber, the excitation source, the spectrometer, and the detector. Usually, the sample is introduced inside the instrument in the form of an aerosol after mixing with a solvent. Later, the aerosol is decomposed in the high-temperature plasma which results in vaporization of the solvent and splitting of molecules into atoms. This high-temperature plasma is made by ionization of a gas (typically argon) using an oscillating radio frequency and may reach temperatures as high as 1000 °C. The spectrometer is used to separate out the element-specific wavelengths before they land on the detector. Calibration of the detector is carried out with standards of known composition as a reference.

In this work, ICP-OES was used to analyze ~0.1 g of various PBA powders inside a digestion vessel with HCl:HNO_3 1:3 and a few drops of HF to get a final volume of 50 ml. This mixture was then put on a hotplate for two hours. Serial dilutions using 5% HNO_3 were carried out to get elements in the calibration range. Each sample was run with a 200x dilution or without dilution to obtain low detection limits on trace elements and high-concentration elements in the calibration range. Ar was used for the plasma, and also as the carrier gas in the sample introduction chamber. Generally, three calibration points were used for each element and up to five for alkali metals. Calibration was performed with certified elements from SCP Science.

3.5. Electrochemical Testing

3.5.1. Coin Cell Assembly

The electrochemical performance of all materials was evaluated in half-cells, i.e., cells with sodium metal as the counter electrode (CE). Coin cells of the 2325-type were assembled with a stack comprising of the working electrode (WE), which was in most cases a PBA-based positive electrode, glass fiber (GF) separators (Whatman), and a Na metal negative electrode (see Figure 3.6). A stainless-steel spacer and spring were place on top of the CE before crimping for higher pressure.

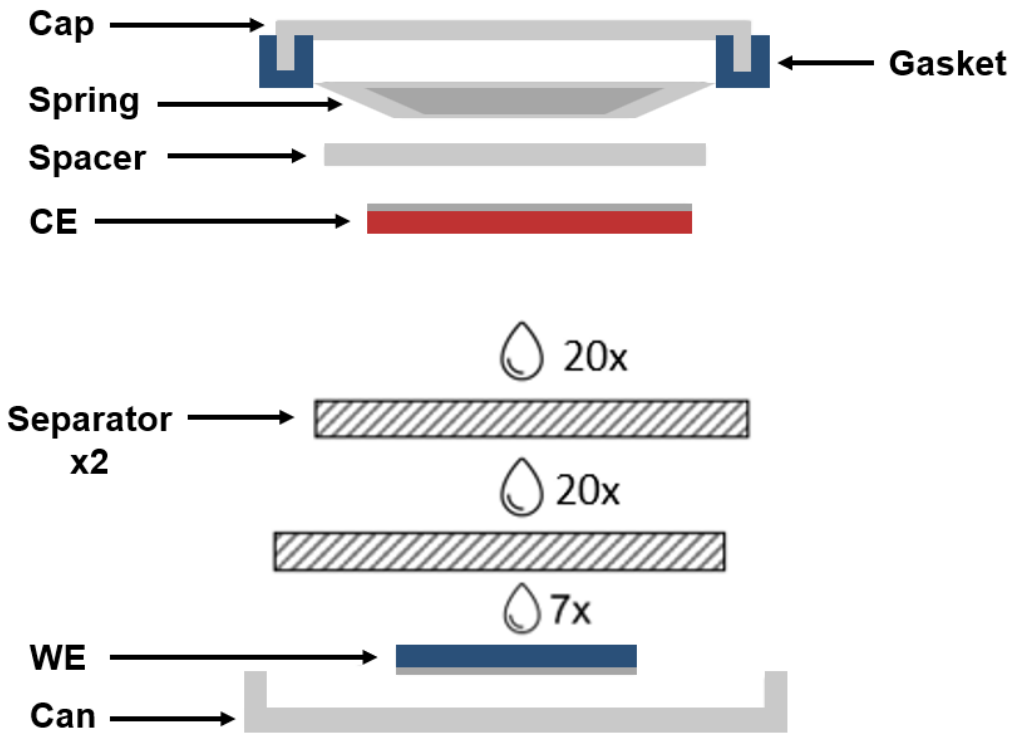

Figure 3.6. Schematic for coin cell stack assembly used in this work.

The PBA-based positive electrodes had a composition of 70% active material, 10%

polyvinylidene fluoride (PVDF) binder, 19.5% Ketjen Black, and 0.5% multi-walled carbon nanotubes (MWCNT) by weight. Few electrode formulations with higher active mass fraction and lower surface area carbon diluents were investigated as well (see Section 8.2). The slurry was prepared by mixing all the powders in desired amounts with N-Methyl-2 -pyrrolidone (NMP) solvent to get a uniform slurry using a planetary mixer (Mazerustar, Japan). The slurry was then hand-coated on a 15 μm thick Al foil. The coating was then dried in an oven at 120 °C for 2 hours. Later, the dried coatings were calendared at ~200 MPa and punched to get 11.25 mm diameter electrode discs (2-3 mg/cm^2 loading). The electrodes were then vacuum-dried at 150 °C overnight prior to coin cell fabrication inside an argon-filled glovebox. All cells were made using 1 M $NaPF_6$ in PC as the electrolyte with 2 wt. % fluoroethylene carbonate (FEC) as an additive (1 M $LiPF_6$ in PC + 2 wt. % FEC in case of LFP cells).

3.5.2. Cycling Parameters

The electrochemical performance of coin cells was evaluated in a temperature-controlled battery cycler (Neware Battery Testing System, Shenzhen, China) at 30 °C. The cycling protocol consisted of a constant current-constant voltage (CCCV) charge step at a C/5 rate to 4.1 V vs. Na^+/Na (until a current limit of C/20 is reached at the constant voltage step) and C/5 constant current (CC) discharge to 2.0 V vs. Na^+/Na. Four C/20 “check-up” cycles were conducted after every 50 C/5 cycles to evaluate low C-rate capacity retention. The C-rate used in this study for NiHCF and $Ni_{0.03}Mn_{0.97}HCF$, MnHCF, or LFP was calculated based on a specific capacity of 85, 170, 170, and 170 mA/g, respectively. For gathering rate performance metrics, discharge rates of D/10, D/5, D/2, 1D, 2D, 5D, and

10D were carried out in half-cells. Charge current densities were kept low (C/10 for D/10 and C/5 for following cycles) to prevent non-uniform plating and dendrite formation in half-cells with Na/Li metal as the CE.

Chapter 4. Synthesis Routes of Prussian Blue

4.1. Co-precipitation Method

The typical synthesis procedure involved the preparation of two solutions for the co-precipitation reaction. Solution A is a 400 ml aqueous solution of equimolar 0.04 M disodium ethylenediaminetetraacetate dihydrate (Na_2EDTA) with manganese chloride ($MnCl_2$) for MnHCF or nickel chloride ($NiCl_2$) for NiHCF. Solution B is a 100 ml aqueous solution of 0.14 M sodium ferrocyanide decahydrate ($Na_4Fe(CN)_6 \cdot 10H_2O$). Solution A was poured into a glass vessel in its entirety and mixed using a magnetic stir bar for 15 minutes at 60 °C. This was followed by pumping of solution B into the reaction vessel under a protective Ar layer to prevent oxidation. After completion of pumping, the resultant solution was continuously stirred for 4 hours at 60 °C and then was allowed to sit idle to help enable the insoluble PBAs to precipitate out and form a suspension. After decanting the suspension, the product was washed and centrifuged three times with de-ionized water and then dried at 120 °C to remove the water and obtain the solid. For Ni-doped MnHCF ($Ni_{0.03}Mn_{0.97}HCF$), a third solution C was made which comprised of 80 ml 0.015 M $NiCl_2$ (10% equivalent moles of $MnCl_2$). Solution C was pumped into the reaction vessel simultaneously with solution B. Figure 4.1 shows the synthesis setup used for the co-precipitation route in this study. To investigate the effect of water content on structural changes in these materials, each synthesized sample was divided into three batches: exposed to 100% relative humidity for 20 hours and then dried at 120 °C or 170 °C under vacuum with a <0.01 torr pressure for 20 hours (discussed in section 7).

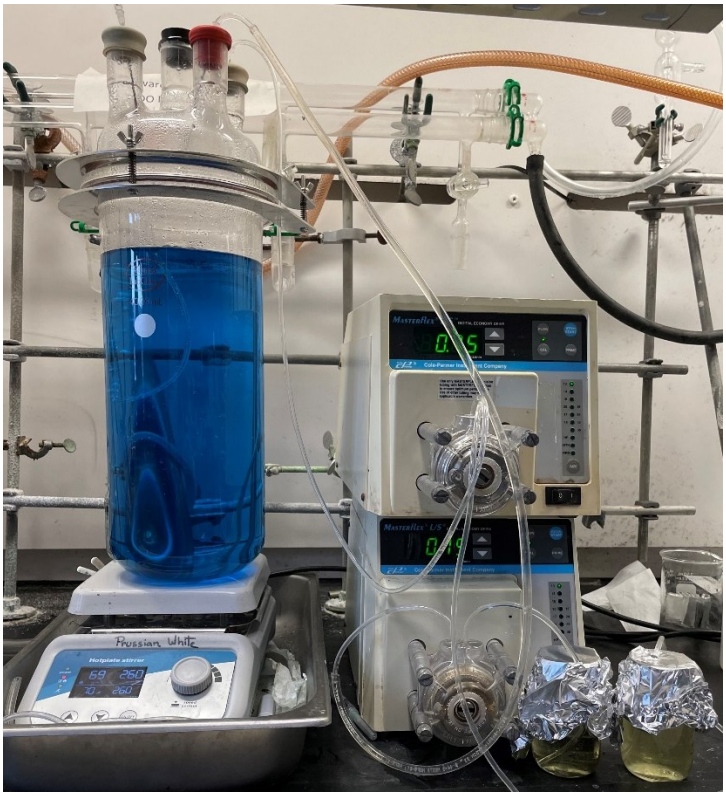

Figure 4.1. Co-precipitation synthesis setup used in this study to produce PBAs.

4.2. Hydrothermal Method

For hydrothermal synthesis of FeHCF, a single iron source approach was followed, similar to that reported by Wang et al. [46] First, 0.004 moles of $Na_4Fe(CN)_6 \cdot 10H_2O$ and 0.0189 moles of ascorbic acid were mixed in 140 ml of DI water. Later, the solution was poured into a polytetrafluoroethylene lined vessel which was subsequently placed between two stainless-steel (SS) discs as shown in Figure 4.2. This stack was then placed inside a stainless casing and cap.

Figure 4.2. Schematic for the hydrothermal reactor assembly used in this study.

After hand-tightening, the reactor was placed inside an oven at 140 °C for 20 hours. Post-synthesis, the solution was centrifuged and washed with distilled water. Finally, the products were dried in an oven at 120 °C for 20 hours.

4.3. Mechanochemical Method

For the mechanochemical synthesis of MnHCF, equimolar $Na_4Fe(CN)_6 \cdot 10H_2O$ and $Mn(CH_3COO)_2 \cdot 4H_2O$ powders (0.015 moles) were added to a tungsten carbide vessel with SS balls in the ratio 2:1 (by wt. %) as shown in Figure 4.3.

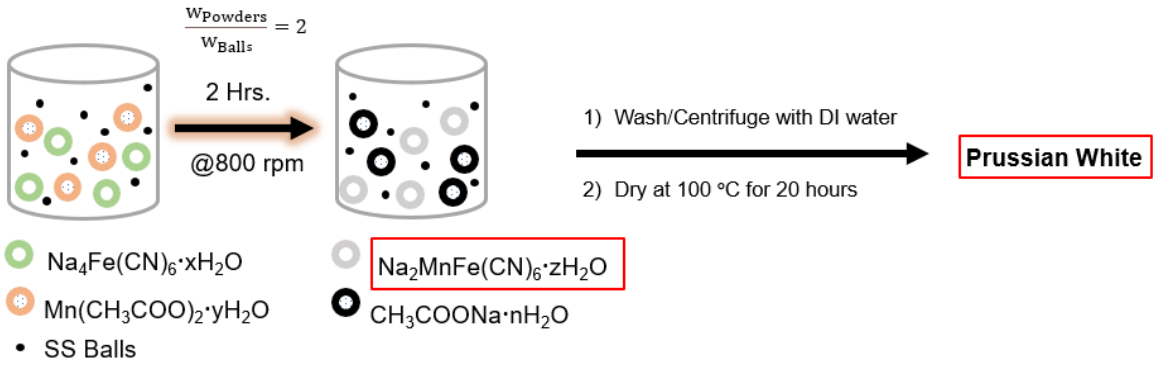

Figure 4.3. Schematic for the mechanochemical synthesis reaction setup in this study.

Then, the powders were subjected to 800 rpm in a ball milling machine for two hours. Afterward, the solution was centrifuged and washed with distilled water to recover the desired PBA powder. Finally, this product was dried in an oven at 120 °C for 20 hours.

Chapter 5. Characterization of Prussian Blue Analogs Made by Different Synthesis Routes

5.1. Co-precipitation Synthesis Results

The co-precipitation technique is a particularly popular and mature route for synthesizing LIB positive electrode active material precursors like transition metal hydroxides $M(OH)_2$, where M can be only one metal, like $Co(OH)_2$, or a combination of different transition metals like Co, Ni, Mn, and Al in the case NMCs or NCAs. The co-precipitation technique permits a high degree of homogeneity in the end product, resulting from atomically mixed transition metals at the M site. Another reason co-precipitation synthesis is more favorable than other synthesis approaches is that it gives users a finer control over experimental parameters like pH, flowrate, stirring speed, baffle shape, temperature, ability to grow gradient materials, etc. on-the-fly, which most other routes lack. Usually, ammonium hydroxide (NH_4OH) is used as a chelating agent to grow dense single-phase particles [112] and the reaction is shown below:

$$M^{2+} + nNH_3 \rightarrow [M(NH_3)_n]^{2+} \quad (8)$$

$$[M(NH_3)_n]^{2+} + 2OH^- \rightarrow M(OH)_2 + nNH_3 \quad (9)$$

However, these LIB precursor products from the co-precipitation route (which are devoid of Li) then need to be subjected to an additional energy-intensive sintering furnace step

for lithiation (around 950 °C) by adding lithium hydroxide (LiOH) or lithium carbonate (Li_2CO_3) as a Li source:

$$4M(OH)_2 + 4LiOH + O_2 \rightarrow 4LiMO_2 + 6H_2O \quad (10)$$

A similar strategy is employed in the synthesis of sodium layered oxide positive electrode active materials like $NaNi_{0.33}Fe_{0.33}Mn_{0.33}O_2$, where LiOH is replaced for NaOH. [9] Some of the earliest PBA synthesis attempts employed a co-precipitation route due to its simplicity. However, in the case of PBAs, no such sintering/sodiation step is required since $Na_4Fe(CN)_6$ acts both as a source of the $Fe[Fe(CN)_6]$ crystal skeleton as well as Na inventory. An optimized co-precipitation can ensure high Na content in the desired product during the coprecipitation step which helps reduce cost, energy input, and synthesis time.

$$Na_4FeCN_6 + MnCl_2 \xrightarrow{aq.} Na_2Mn[Fe(CN)_6] + 2NaCl \quad (11)$$

Figure 5.1 shows SEM images of the PBA powders synthesized via the co-precipitation route used in this work. All PBA single crystals show cubic morphologies, similar to most reports elsewhere in the literature. [113][114][33][34] Maeng et al. showed that by acid etching, spherical morphologies are possible for PBAs [115] which may help increase the tap density, and by extension electrode-level density. The as-synthesized NiHCF has a rough particle surface and relatively small primary particles of ~1-2 μm diameter that are agglomerated in a jagged way, which may lead to a higher surface area than the other

two analogs (see Figure 5.1). The other two analogs, $Ni_{0.03}Mn_{0.97}HCF$ and MnHCF, show relatively large cubic primary particles (see Figures 5.1b and c, respectively), with particle diameters of ~1-5 μm and ~3-10 μm, respectively.

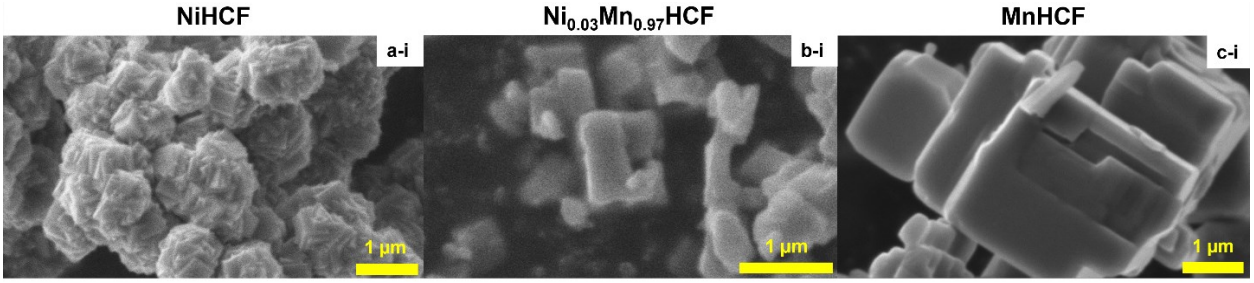

Figure 5.1. SEM images of (a) NiHCF, (b) $Ni_{0.03}Mn_{0.97}HCF$, and (c) MnHCF synthesized via co-precipitation route.

Figure 5.2 shows EDS elemental mapping that was employed to analyze the elemental distribution of Na, Mn, Fe, and Ni for (i) NiHCF, (ii) $Ni_{0.03}Mn_{0.97}HCF$, and (iii) MnHCF. As evident from Figures 5.2a-i, 5.2b-i, and 5.2c-i, NiHCF has well-distributed Na, Fe, and Ni across the various particles shown, but Mn is absent in this sample (see Figure 5.2c-i). On the other hand, MnHCF shows Na, Fe, and Mn homogenously dispersed in the particles, but the absence of Ni. Figure 5.2d-ii shows that a relatively weak signal for Ni is present in the case of $Ni_{0.03}Mn_{0.97}HCF$. A clear correlation of Ni to the places of the active material particles might be missing due to the very small agglomerate size for this material (see Figure 5.1).

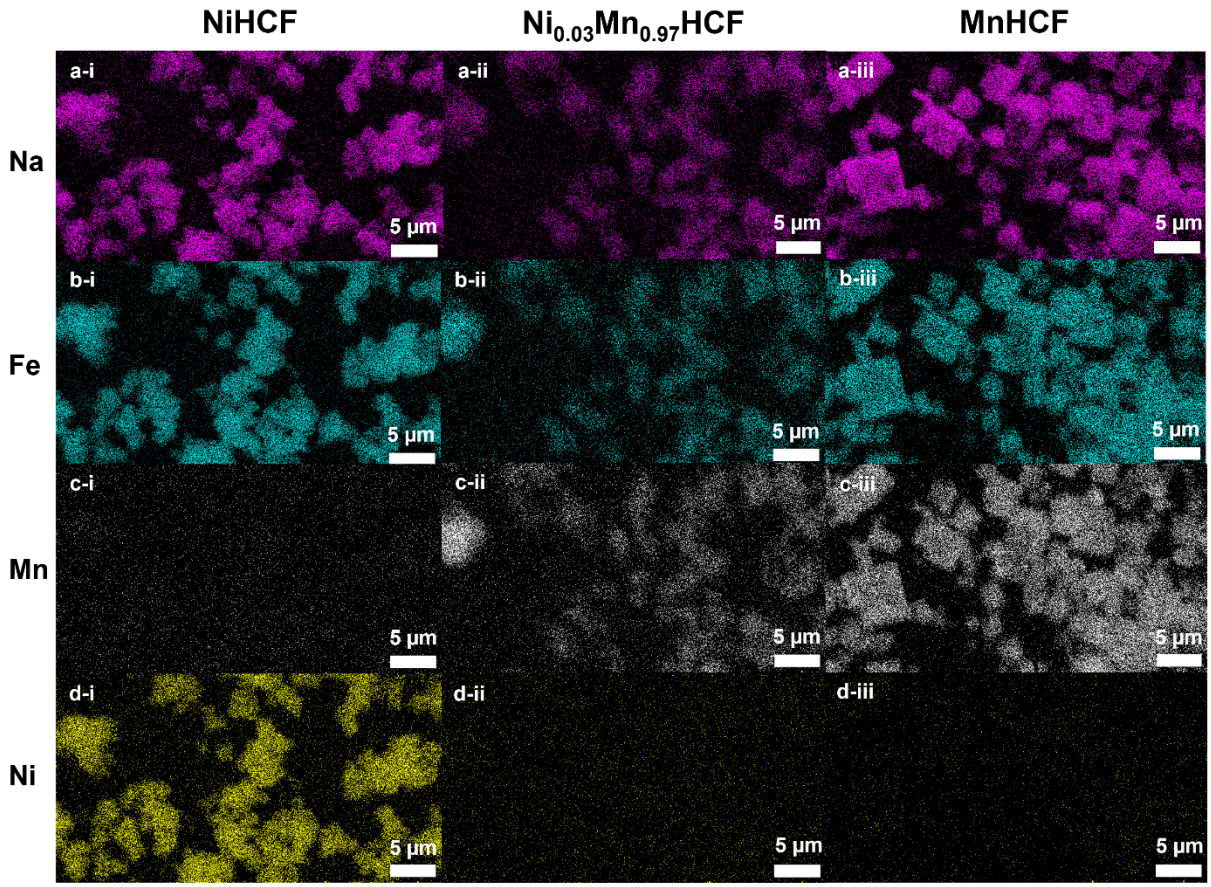

Figure 5.2. EDS elemental mapping showing the distribution of (a) Na, (b) Fe, (c) Mn, and (d) Ni for (i) NiHCF, (ii) $Ni_{0.03}Mn_{0.97}HCF$, and (iii) MnHCF.

Table VI shows the transition metal ratios in at. % as determined by EDS for the co-precipitation samples from Figure 5.2. Based on this, $Fe(CN)_6$ vacancies present in the structure can be calculated by comparing Fe to Mn and/or Ni ratio. NiHCF has approximately equal ratios of Fe to Ni (51:49 in at. %), indicating minimal vacancies present. MnHCF shows a slightly higher Mn to Fe ratio (48:52 in at. %), which may be ascribed to $Fe(CN)_6$ vacancies present in the MnHCF structure. However, we rely on the electrochemical capacitive method as a more accurate way to quantify these vacancies (see Section 8) because of the potential quantification error associated with the surface-

sensitive EDS technique. $Ni_{0.03}Mn_{0.97}HCF$ has a small amount of Ni present. Based on the synthesis procedure, 10 at. % of Ni at M' site in the structure (or roughly 5 at. % of total transition metals, since Fe:Mn is 1:1 in a vacancy-free MnHCF) was expected i.e., $Ni_{0.10}Mn_{0.90}HCF$ was the target compound. However, EDS suggested Ni worth of only ~3 at. % equivalents were present in the product post-synthesis (i.e., $Ni_{0.03}Mn_{0.97}HCF$ being the actual compound). It is reported that chelating agents like citrate show asymmetrical affinity even for the same valency transition metals due to the different binding enthalpies and equilibrium constants, [116][117] causing a delay in the release of the more strongly chelated transition metal compared to the other ones. Hue and co-workers found that under an identical set of conditions, EDTA chitooligosaccharide shows preferential absorption of Ni^{2+} over Mn^{2+}. [118] Hence, the less-than-expected Ni in the final $Ni_{0.03}Mn_{0.97}HCF$ product based on reactant stoichiometry during synthesis (the expected ratio at M' site for Mn:Ni was 90:10, but the actual one being 97:3) may be explained by a higher affinity of EDTA towards Ni than Mn, and the fact that the ratio of free EDTA molecules (i.e., the ones that are not bonded to any TM) to the incoming Ni moles in the reaction vessel increase as a function of time. Both factors have the potential to slow down the release of Ni during the co-precipitation reaction.

Table VI. Total transition metal ratios (i.e., site M + M') for PBAs based on EDS.

Transition Metal	**NiHCF**	**$Ni_{0.03}Mn_{0.97}$HCF**	**MnHCF**
Fe (at. %)	51.0	46.7	47.8
Mn (at. %)	-	51.3	52.2
Ni (at. %)	48.9	2.00	-
Ni to Mn (at. %)	-	2.6	-

$Ni_{0.03}Mn_{0.97}$HCF, however, also shows slightly reduced Fe content compared to the other two, which can be ascribed to the $Fe(CN)_6$ vacancies present in the structure and is also evident from the considerably lower reversible capacity than the theoretical value for a vacancy-free structure (see Figure 8.1b from Section 8). As stated earlier, we chose to depend on the electrochemical capacitive method to quantify these vacancies. To estimate the Na content present in these samples post-synthesis, ICP-OES was employed, and the results are shown in Table VII. The sodium content (x) in the stoichiometry of $Na_xM'[M(CN)_6]\cdot zH_2O$ can be determined as the ratio of Na to M' atoms present per unit weight. This calculation assumes that Ni and/or Mn populate the M' site bonded to N in the hexacyanoferrate structure (M'-N≡C-M), whereas all Fe is in the M site bonded to C.

Table VII. Na content in PBAs based on ICP-OES.

Metal(s)	NiHCF	$Ni_{0.03}Mn_{0.97}HCF$	MnHCF
Na [moles/kg]	4817	4697	4933
Ni + Mn [moles/kg]	2382	2666	2644
Na / (Mn + Ni) [-]	2.02	1.76	1.87

Figure 5.3 shows the XRD pattern of synthesized samples from the co-precipitation method, all having a monoclinic-rich phase (P21/n space group) based on comparison to other literature references, [34][44][61] which indicates a high level of Na (also validated by ICP, see Table VII) and considerable interstitial water as verified by TGA (see Figure 6.2). Monoclinic and rhombohedral phases are more desirable than the cubic phase because of the higher sodium content and possibly lower defects (the latter translates to higher reversible capacity because of greater availability of redox active sites).

Figure 5.3b helps compare the position of the dominant peaks for all three analogs, and it can be seen that they have moved to higher angles in the case of NiHCF when compared to MnHCF, which indicates a reduction in unit parameters according to Bragg's law. This can be explained by the smaller radius of Ni compared to Mn (248 vs. 254 pm). Whereas the peak positions for $Ni_{0.03}Mn_{0.97}HCF$ and MnHCF are nearly identical, which indicates that the addition of a mere 3 at. % Ni does not alter the unit cell parameters considerably, which agrees with the refinement results (see Table VIII).

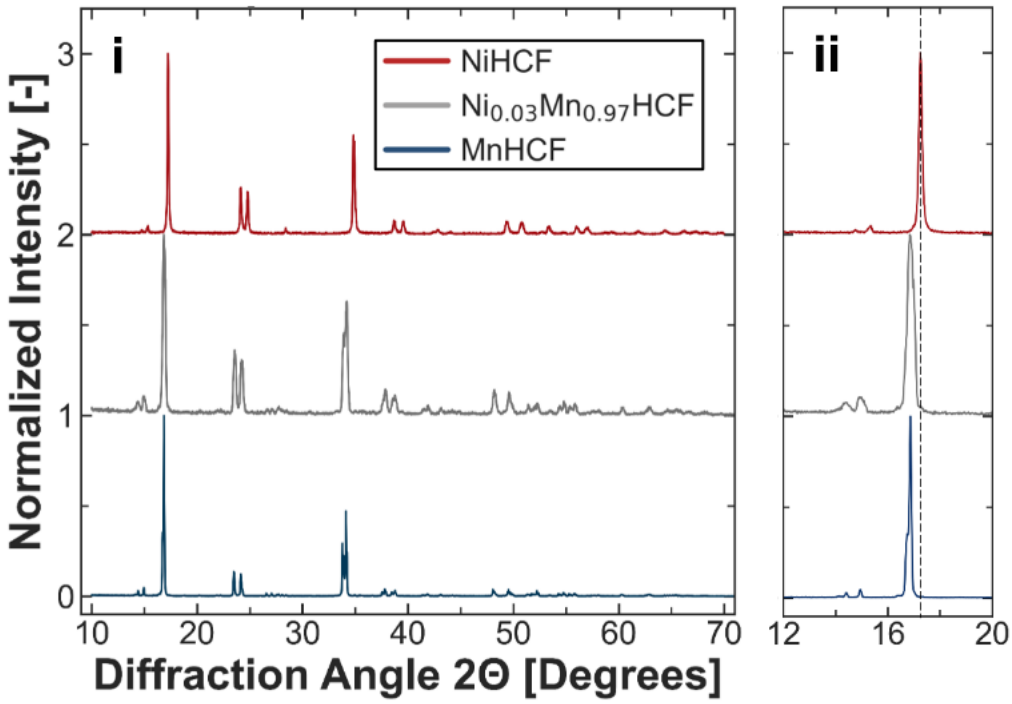

Figure 5.3. XRD spectra for NiHCF, $Ni_{0.03}Mn_{0.97}HCF$, and MnHCF synthesized using co-precipitation route.

Peak splitting at ~24°, ~39°, ~50°, and ~56° is observed for the monoclinic phase (since a ≠ c) and is ascribed to the distortion induced by high Na content which the Na-poor cubic phase (a = b = c) lacks. [81] Lim and co-workers also had a similar observation, where splitting of (220), (420), (440), and (620) diffraction peaks into two near-equal intensity peaks occurred when the sodium content (x) was increased from 1.5 to ~2. [43]

To demonstrate the efficacy and confidence in our synthesis approach, a successful scale-up synthesis of NiHCF was carried out in a 4 Lt reaction vessel, an 8-fold increase in throughput compared to the original setup (0.5 Lt). Figure 5.4a shows the XRD patterns for NiHCF obtained from both reaction volumes (see Figure 5.4b), both showing the pure Na-rich monoclinic phase without any impurity phases. The exact yield was difficult to determine because of the material loss during as a result of insufficient centrifugation

(limited by the instrument) and multiple washing steps involved. By using the known amount of reactants used as a rough basis, the yield for a typical synthesis can be estimated to be about 0.02 mol/Lt.

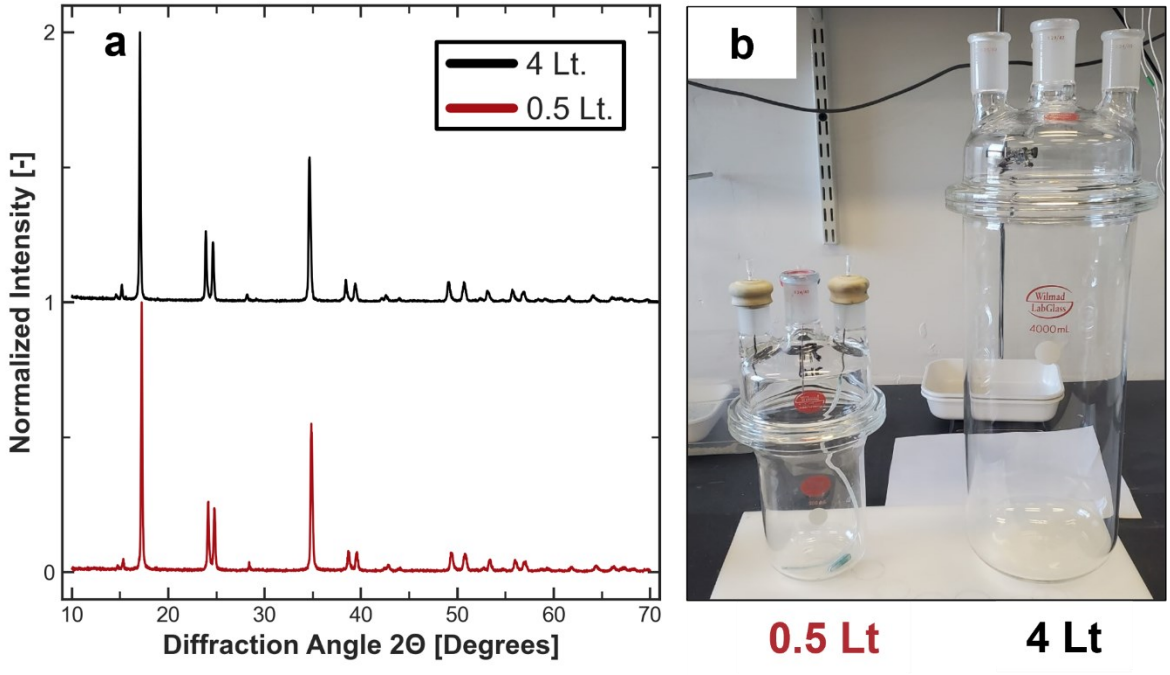

Figure 5.4. (a) XRD patterns for NiHCF synthesized via co-precipitation route in (b) 0.5 and 4 Lt reaction vessels.

5.2. Hydrothermal Synthesis Results

FeHCF was synthesized using a hydrothermal route, and the recipe was initially inspired by the work of Wang and co-workers from the Goodenough group, who achieved a pure rhombohedral product. [33] However, when their exact synthesis procedure was followed, which comprised of adjusting the pH level to 6.5 before transferring the hydrothermal reaction vessel to the oven, the resultant powder post-synthesis turned out to be reddish-

brown (as opposed to the expected blue/white color), indicating the formation of Fe_2O_3, as also reported by Camacho and co-workers. [119] After adjusting the pH to 3, a blue-colored cubic phase FeHCF ($Fm\bar{3}m$ space group) was achieved. Figure 5.5 shows the XRD spectra for FeHCF synthesized via the hydrothermal route in this study.

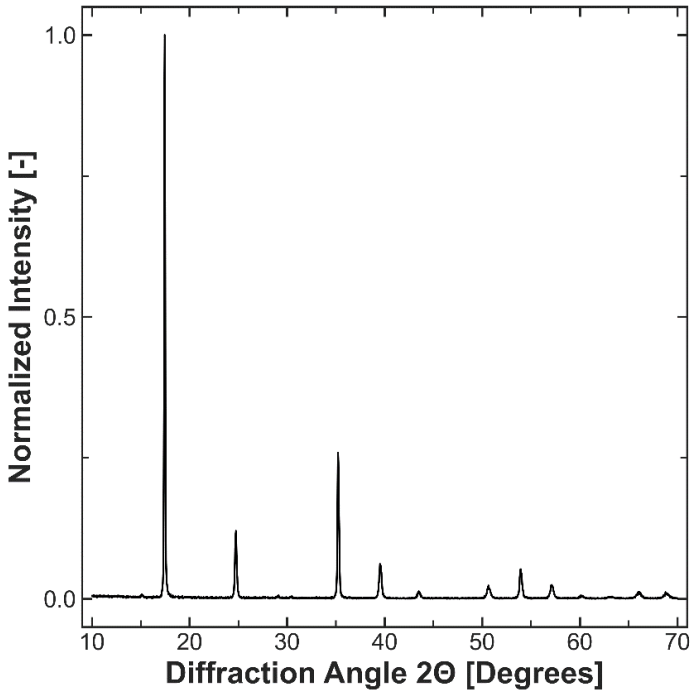

Figure 5.5. XRD pattern for cubic phase FeHCF synthesized via the hydrothermal reaction route.

Here, the peak splitting is absent because of the lower Na content and exhibits a highly symmetrical cubic phase, meaning less Na content or more vacancies, or both. Figure 5.6 shows SEM micrographs for FeHCF obtained from the hydrothermal route. The hydrothermal synthesis of FeHCF allowed the growth of large and highly crystalline single crystals with very well-defined cubic morphology. Since polyanionic positive electrode active materials tend to have lower electronic conductivity than their oxide counterparts,

it is suggested that such big particles may not be the most ideal morphology from a kinetics point of view and an additional step of ball milling may be required to achieve the desired particle size.

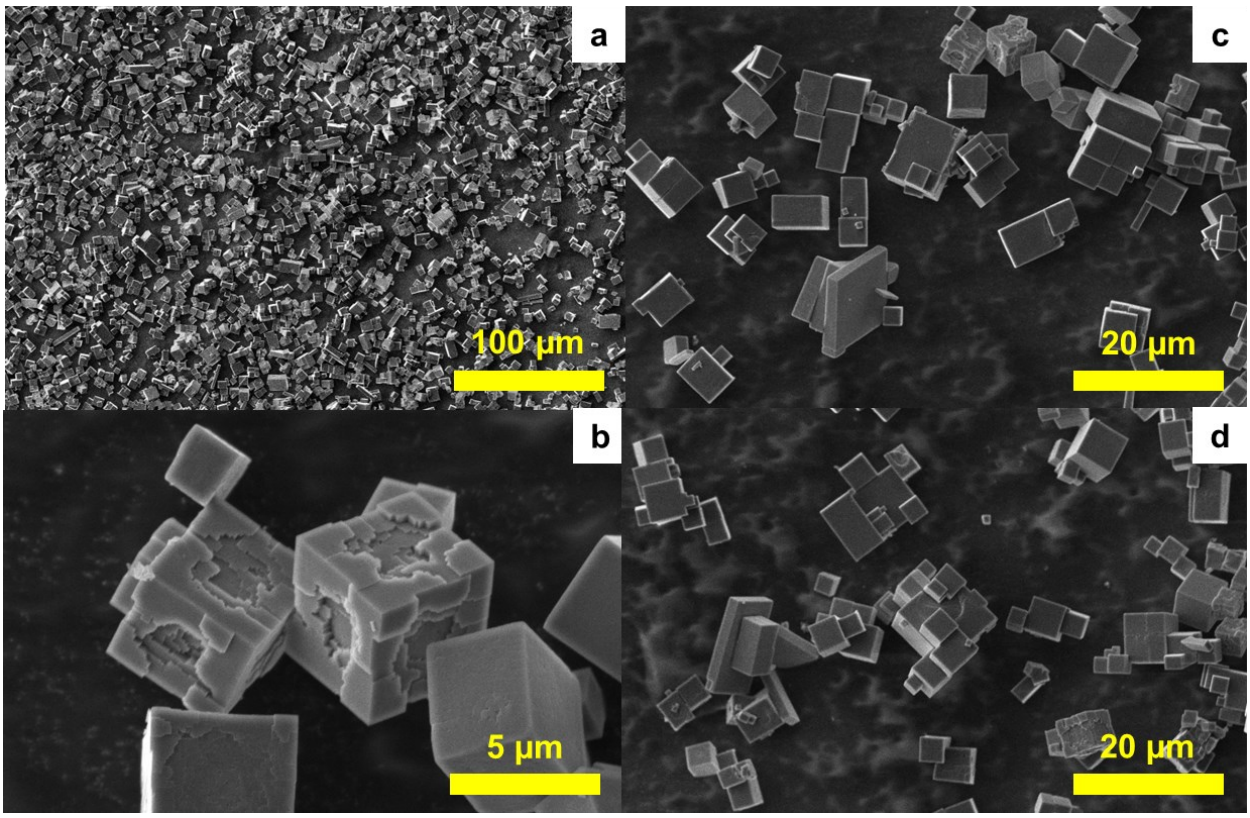

Figure 5.6. SEM images for FeHCF synthesized via hydrothermal route.

With more synthesis optimization, it is believed that a product with higher Na content, i.e., in the monoclinic/rhombohedral phase can be synthesized instead of the cubic phase shown here.

5.3. Mechanochemical Synthesis Results

Mechanochemical synthesis is a fairly new approach for synthesizing PBAs which tries to help minimize water usage during synthesis and promises a greater yield. [120] As described earlier, the synthesis procedure comprised of mixing of $Na_4Fe(CN)_6 \cdot 10H_2O$ and $Mn(CH_3COO)_2 \cdot 4H_2O$ with stainless steel balls (1:2 by wt.). Post milling, the crystal water from $Na_4Fe(CN)_6 \cdot 10H_2O$ comes out and results in a sticky paste also containing CH_3COONa as a side-product, which called for washing and centrifugation. Figure 5.7 shows the XRD spectrum for MnHCF obtained via this route, which exhibits sharp diffraction patterns associated with the monoclinic phase and splitting of peaks revealing a high Na content.

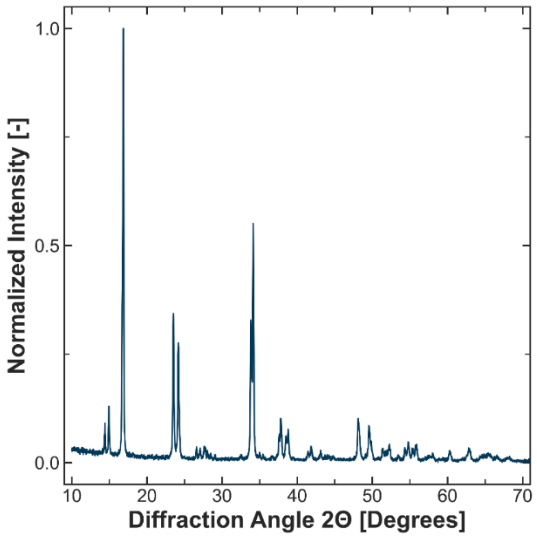

Figure 5.7. XRD pattern for MnHCF (monoclinic phase) synthesized via mechanochemical reaction route.

Figure 5.8 shows the SEM image for MnHCF obtained via mechanochemical synthesis. The particles have a relatively irregular surface morphology and significantly smaller particle distribution than the products obtained from the co-precipitation and hydrothermal route.

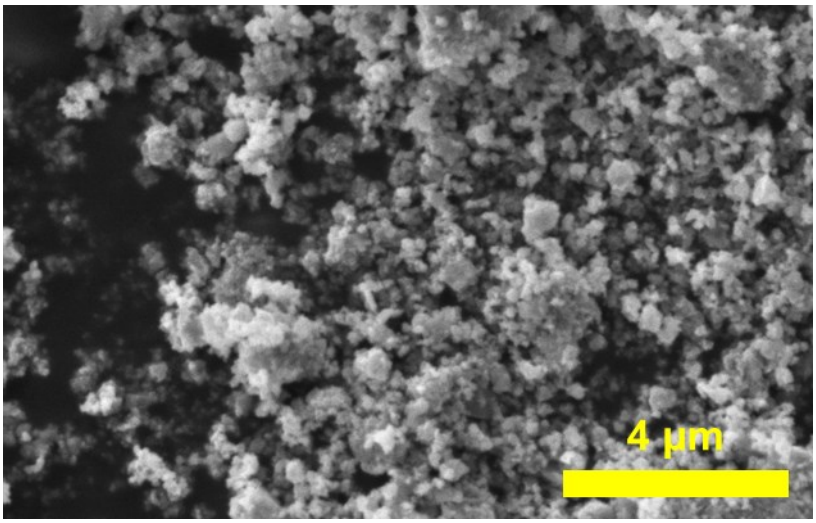

Figure 5.8. SEM image for MnHCF synthesized via mechanochemical route.

Figure 5.9 shows the voltage-capacity profile for MnHCF synthesized via the mechanochemical route, showing a high specific capacity of 167.8 mAh/g which is very close to the ~170 mAh/g theoretical capacity for the material and can be attributed to the minimal $Fe(CN)_6$ vacancies. However, this material shows considerable voltage polarization which is undesirable and hopefully can be addressed with more synthesis optimizations.

Despite achieving a Na-rich phase, the mechanochemical route does not currently look industrially viable when compared to the co-precipitation route for a true scale-up. This is

due to several drawbacks such as poor temperature management and metal contamination issues during milling. Due to the high impact during milling, equipment needs to withstand high shear and stresses as well. Chemically resistant materials like ceramic and glass cannot be used due to lower compressive strength, while structurally robust materials like stainless steel lack chemical inertness during synthesis. Alloys may fill both of these criteria but are ~3-4 times more expensive. [121] Also, this rather low-temperature "dry solid-state" synthesis approach may not be able to match the high degree of homogeneity in the end product at an atomic level that the co-precipitation route can offer.

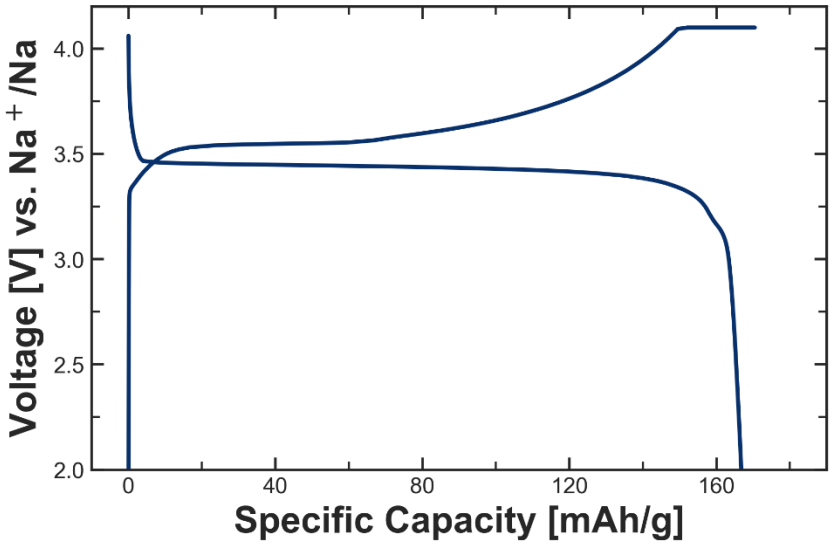

Figure 5.9. Voltage-capacity profile of MnHCF, (synthesized via mechanochemical route collected) in a half-cell at 30 °C using a C/5 rate (tenth cycle) between 2 and 4.1 V vs. Na/Na^+. The C-rate was calculated based on a specific capacity of 170 mAh/g and was assembled with 1 M $NaPF_6$ PC + 2 wt. % FEC electrolyte.

Chapter 6. Impact of Processing and Drying Conditions on Prussian Blue Analogs

As mentioned in Section 5.1, the as-synthesized PBAs from the co-precipitation syntheses (NiHCF, $Ni_{0.03}Mn_{0.97}HCF$, and MnHCF) were divided into three batches to study the impact of water content on structural changes of the PBAs; One batch was exposed to 100% relative humidity (for 20 hours and used as is), the others were first exposed and then dried at 120 or 170 °C (under vacuum for 20 hours with <0.01 torr pressure).

The XRD patterns for all materials after the above-mentioned different processing conditions are shown in Figure 6.1. The XRD patterns for the 170 °C vacuum-dried samples were collected using an air-tight holder which lowered the signal-to-noise ratio. All other samples show sharp diffraction peaks, suggesting a high degree of crystallinity. Upon prolonged exposure, all materials still retained the monoclinic phase (P21/n space group) (see Figure 6.1a) which is an indication of high sodium content and considerable interstitial water content present according to previously reported works [34][44] and agrees with our TGA analysis presented in next section (see Figure 6.2). The fact that all three materials (NiHCF, $Ni_{0.03}Mn_{0.97}HCF$, and MnHCF) still retain a monoclinic phase after prolonged exposure to moisture is rather encouraging, as it tells us that loss of Na from the bulk is minimal (otherwise the materials would have undergone a monoclinic to cubic transformation, see Table II), and hence enables handling in less stringent environments or even aqueous processing. [35][36] Ojwang et al. reported that their FeHCF material is

rather moisture sensitive, which caused it to lose Na from the bulk and undergo a monoclinic to cubic transformation. [122] The higher moisture sensitivity of FeHCF may be due to the rapid oxidation of N-bonded ($Fe^{II/III}$-N ≡C-$Fe^{II/III}$) which seems more sluggish for N-bonded Mn in the case of MnHCF (Mn-$N^{II/III}$≡C-$Fe^{II/III}$). This discrepancy between FeHCF and MnHCF may be explained by the difference in their standard ionization energies, i.e., ease of getting oxidized (2957 and 3248 kJ/mol for $Fe^{II \rightleftharpoons III}$ and $Mn^{II \rightleftharpoons III}$, respectively).

Peak splitting is visible for the exposed and 120 °C dried NiHCF, $Ni_{0.03}Mn_{0.97}$HCF and MnHCF samples (see Figures 6.1a and b) at ~24°, ~39°, ~50°, and ~56°. Shen et al. ascribe this peak splitting to high Na content which induces a distortion in the monoclinic crystal structure. This distortion seems to be minimal in the case of the highly symmetric Na-poor cubic phase (where a = b = c), which prevents peak splitting. [81] Lim and co-workers also reported a similar phenomenon of peak splitting for (220), (420), (440), and (620) planes into two diffraction peaks of near-equal intensities when the sodium content (x) was increased from 1.5 to ~2. [43]

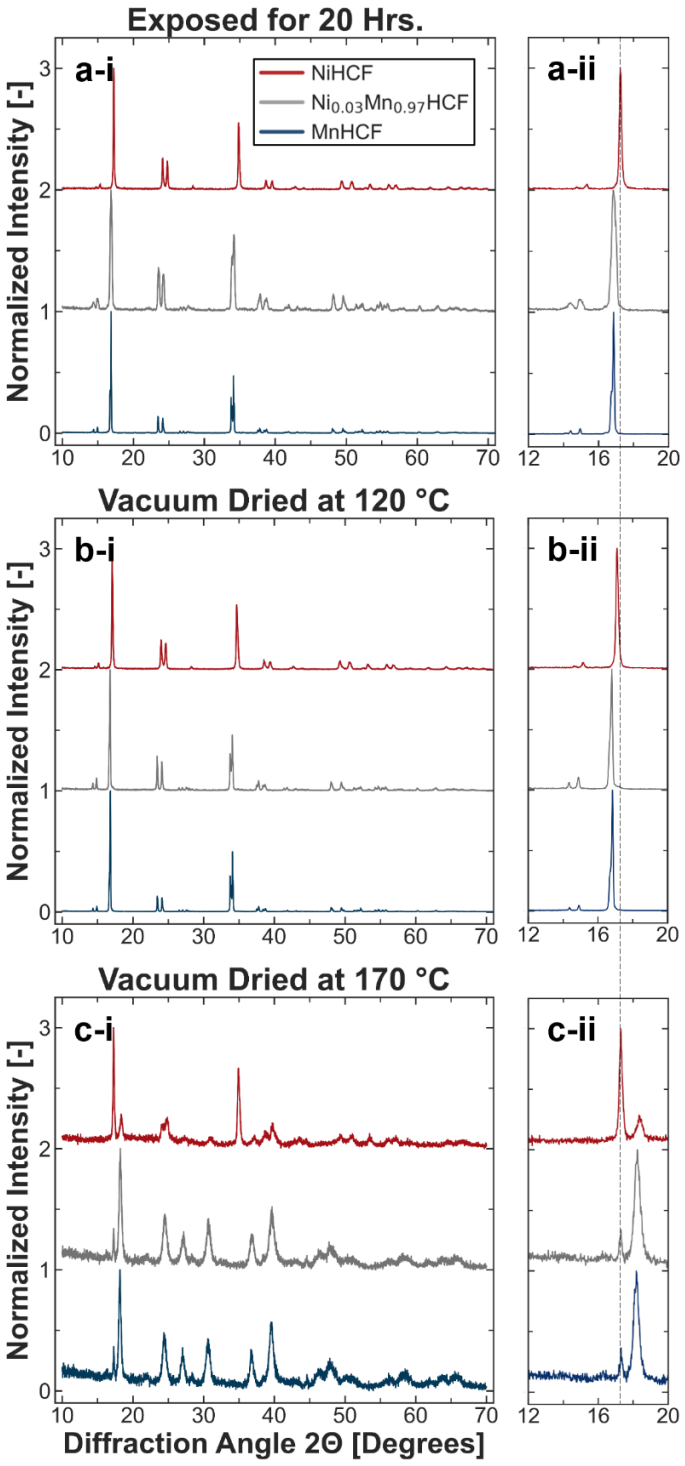

Figure 6.1. XRD spectra for PBAs (a) exposed for 20 hours, (b) vacuum-dried at 120 °C, and (c) vacuum-dried at 170 °C for 20 hours. XRD patterns for the 170 °C samples were collected using an air-tight holder (sample prepared inside an Ar-filled glovebox) to minimize the impact of moisture during data collection.

XRD refinement was carried out for the exposed samples because of its high signal-to-noise ratio and the findings are presented in Table VIII. The dominant diffraction peaks between 16-18° (see Figure 6.1a-i and ii) are found at higher angles for NiHCF than for $Ni_{0.03}Mn_{0.97}$HCF and MnHCF, which suggests a smaller unit cell volume. This is in agreement with the refinement results findings for the exposed samples: 547.80, 582.37, and 583.89 $Å^3$ for NiHCF, $Ni_{0.03}Mn_{0.97}$HCF, and MnHCF, respectively. As stated earlier, this difference in unit cell parameters mostly likely arises from the smaller diameter of Ni compared to Mn (248 vs. 254 pm).

Increasing the drying temperature from 120 to 170 °C led to the formation of the rhombohedral phase ($R\bar{3}$ space group) in the case of $Ni_{0.03}Mn_{0.97}$HCF and MnHCF (by eliminating interstitial water), while it seems like NiHCF mostly remains in the monoclinic phase (see Figure 6.1c). Multiple literature reports suggest that MnHCF is present in the rhombohedral phase when it is nearly free of interstitial water. [34][123][44] On the other hand, it was interesting to see that NiHCF did not completely undergo monoclinic to rhombohedral phase transformation, unlike the other two PBAs, [64] indicating that water removal is more difficult for the former material (see also the TGA analysis in Figure 6.2 for correlation). This may be attributed to the relatively smaller unit cell volume for NiHCF (see Table VIII for unit cell parameters) that possibly hinders the removal of interstitial water from the bulk of the crystal. Moritomo et al. also saw a decrease in unit cell volume of MnHCF when Ni doping was introduced at the M' site ($Na_{1.44}Mn^{II}[Fe^{II}(CN)_6]_{0.86}\cdot 2.8H_2O$ vs. $Na_{1.64}Mn^{II}_{0.74}Ni^{II}_{0.26}[Fe^{II}(CN)_6]_{0.91}\cdot 3.9H_2O$). [124] In agreement with our work, Hebert and

co-workers reported a smaller unit cell volume for NiHCF than MnHCF of 541.63 and 584.31 $Å^3$, respectively, which is close to results from our study. [63]

It is crucial to obtain the water-free rhombohedral phase in the case of MnHCF and $Ni_{0.03}Mn_{0.97}HCF$ before cell fabrication, since any interstitial water present in the monoclinic phase of these materials can be released during charge/discharge cycling, causing potentially undesirable side reactions and decreasing electrochemical and lifetime performance. [34][44] Song and co-workers performed an XRD analysis that revealed a reduction in the unit cell volume of MnHCF when interstitial water was removed [34] i.e., when going monoclinic to rhombohedral phase, which is in agreement with the peak shift to higher angles in our finding (see Figures 6.1b and c). In the case of monoclinic NiHCF, such an interstitial water removal requirement before cell fabrication seems unnecessary since interstitial water is unlikely to escape from the structure during cycling (see TGA analysis in Figure 6.2c).

Unlike MnHCF, NiHCF does not lose its interstitial water easily, and hence it does not form the rhombohedral phase and only undergoes a monoclinic to cubic transformation upon removal of one Na per formula unit. MnHCF instead undergoes a rhombohedral to cubic transformation, and at the end of charge, when all Na is removed and both TMs are in the +3 oxidation state, the material undergoes a cubic to tetragonal phase transformation (see Table II). Note that for NiHCF, there is only one redox active center ($Na_2Ni^{II}[Fe^{II}(CN)_6]$ (monoclinic) ⇌ $Na_1Ni^{II}[Fe^{III}(CN)_6]$ (cubic)), so the cubic to tetragonal phase transformation seems to be forbidden unlike for MnHCF ($Na_2Mn^{II}[Fe^{II}(CN)_6]$

(rhombohedral/monoclinic) ⇌ $Na_1Mn^{II}[Fe^{III}(CN)_6]$) (cubic) ⇌ $Na_0Mn^{III}[Fe^{III}(CN)_6]$ (tetragonal)).

Figure 6.2 shows the mass loss in TGA due to water removal for the three PBAs after following the three processing and drying conditions: (a) exposed to 100% relative humidity for 20 h, (b) vacuum-dried at 120 °C, and (c) vacuum-dried at 170 °C. Two distinct weight loss steps are visible in the case of the exposed samples (see Figure 6.2a). The first step in the 75-100 °C range can be ascribed to the loss of surface adsorbed water and the second step starting at ~175 °C to the removal of interstitial water. For the samples dried at 120 °C, the first weight loss step (due to surface water) is absent but the second step due to the interstitial water loss still exists (see Figure 6.2b). This shows that vacuum-drying at 120 °C is effective at removing surface adsorbed water, but not interstitial water. This agrees with the XRD analysis, which showed the monoclinic phase for all materials after vacuum-drying at 120 °C (see Figure 6.1b). The $Ni_{0.03}Mn_{0.97}$HCF and MnHCF samples dried at 170 °C show only a minimal weight loss of <0.6 % until 350 °C, which proves that both adsorbed and interstitial water have been successfully removed (see Figure 6.2c). This is consistent with the presence of the rhombohedral phase in the XRD pattern shown in Figure 6.1c.

Interestingly, the weight loss of NiHCF always occurs at higher temperatures than for $Ni_{0.03}Mn_{0.97}$HCF or MnHCF, for all conditions, no matter if exposed to moisture or vacuum dried at 120 and 170 °C (see Figures 6.2a-c). This phenomenon may be ascribed to its smaller unit cell volume (as discussed above), which could hinder the removal of water

from the bulk. Hu and co-workers reported a similar observation, where NiHCF had ~1.7 times more water than MnHCF even after vacuum-drying at 120 °C. [64] The fact that interstitial water could not be removed in the case of NiHCF even at 170 °C is consistent with the XRD pattern in Figure 6.1c showing a monoclinic phase. Based on this analysis, removal of interstitial water from NiHCF requires a temperature of at least ~225 °C or above (see Figure 6.2c). To get the stoichiometries presented in Table VIII, the water content of the 170 °C samples was considered, which was <0.6% in the case of $Ni_{0.03}Mn_{0.97}$HCF and MnHCF and ~5 wt. % in the case of NiHCF. The stoichiometries for the PBAs synthesized in this work via the co-precipitation route are shown in Table VIII and found by combining the characterization results from EDS, ICP-OES, TGA, and the sodiation capacities (see Section 8.1).

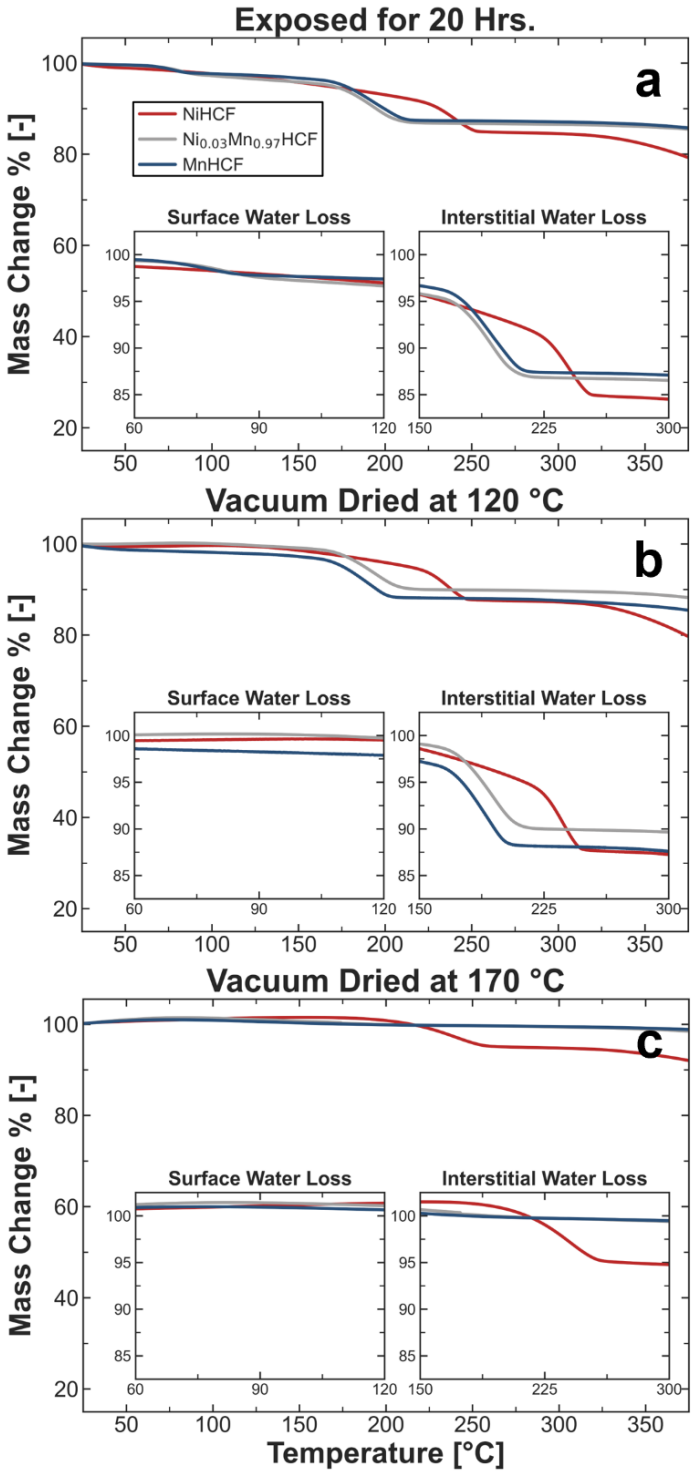

Figure 6.2. TGA curves representing mass loss due to dehydration of PBA powders (a) exposed for 20 hours, (b) dried at 120 °C, and (c) dried at 170 °C. Heating protocol consisted of a constant 5 °C per minute ramp rate to 400 °C.

Table VIII. Stoichiometry, lattice parameters, and water content for NiHCF, $Ni_{0.03}Mn_{0.97}HCF$, and MnHCF.

Analog		Exposed	120 °C	170 °C
NiHCF $Na_{1.99}Ni[Fe(CN)_6]_{0.994}\square_{0.006}$	Phase Designated	Monoclinic	Monoclinic	Monoclinic
	Space Group	P21/n	P21/n	P21/n
	Water Present (wt. %)	15.50	12.75	5.23
	a, b, c [Å]	10.322, 7.352, 7.224		
	Unit Cell Volume [$Å^3$]	547.804		
$Ni_{0.03}Mn_{0.97}HCF$ $Na_{1.76}Ni_{0.03}Mn_{0.97}[Fe(CN)_6]_{0.86}\square_{0.14}$	Phase Designated	Monoclinic	Monoclinic	Rhombohedral
	Space Group	P21/n	P21/n	$R\bar{3}$
	Water Present (wt. %)	13.47	10.34	0.61
	a, b, c [Å]	10.582, 7.524, 7.320		
	Unit Cell Volume [$Å^3$]	582.365		
	α, β, ɣ [°]	90, 92.18, 90		
MnHCF $Na_{1.87}Mn[Fe(CN)_6]_{0.95}\square_{0.049}$	Phase Designated	Monoclinic	Monoclinic	Rhombohedral
	Space Group	P21/n	P21/n	$R\bar{3}$
	Water Present (wt. %)	12.91	12.41	0.52
	a, b, c [Å]	10.595, 7.534, 7.320		
	Unit Cell Volume [$Å^3$]	583.884		
	α, β, ɣ [°]	90, 92.21, 90		

The Na content (x) in the stoichiometries presented in Table VIII is based on ICP-OES (see Table VII). EDS findings were used to estimate the transition metal ratios (see Table VI). The $Fe(CN)_6$ vacancies (□) were quantified as the difference between the observed reversible and theoretical capacities of each material (see Section 8), i.e., we assume that a defect-free material will have near theoretical reversible capacity. Note that the number of vacancies could also be determined from the transition metal ratios from EDS (see Table VI), but the capacitive method is independent of potential errors in the EDS quantification as discussed above. The difference in the vacancy content based on these two methods for NiHCF, $Ni_{0.03}Mn_{0.97}HCF$, and MnHCF is 4.9, 5.1, and 3.7%, respectively. The water content (z) represented in the above stoichiometries is reported for the samples that were vacuum dried at 170 °C.

Chapter 7. Increasing Sodium Content of Prussian Blue Analogs Post-Synthesis

In a non-ideal synthesis of PBAs, the Na content (x) can be less than what the structure could accommodate due to the oxidation of transition metals. [43] This can be addressed post-synthesis by using reducing agents like NaI (see Equation 8) and $NaBH_4$. Jeżowski et al. proposed that during donating Na, other by-products from $NaBH_4$ may include B and H_2 [125] (see Equation 9). For this set of experiments, a MnHCF material represented by the formula $Na_{1.22}Mn[Fe(CN)_6)]_{0.8}\square_{0.2}$ was used. Here, the starting value of x is 1.22, but the structure can theoretically accommodate a Na content of x = 1.6. In a half-cell, the missing Na can be replenished from the Na metal counter electrode. However, in a more practical full-cell, where the counter electrode, i.e., the negative electrode is typically hard carbon, all Na needs to come form the positive electrode. Hence, an attempt was made to increase the sodium content of PBAs post-synthesis. The procedure involved mixing 2x the stoichiometric amount of NaI (acetonitrile media inside an Ar-filled glovebox) or $NaBH_4$ (aqueous media) with MnHCF and reacting it under magnetic stirring for 48 hours.

$$Na_{2-x}Mn[Fe(CN)_6] + NaI \rightarrow Na_{2-x+q}Mn[Fe(CN)_6] + \frac{q}{2}I_2 + (1-q)NaI \quad (8)$$

$$Na_{2-x}Mn[Fe(CN)_6] + NaBH_4 \rightarrow Na_{2-x+q}Mn[Fe(CN)_6] + qB + 2qH_2 + (1-q)NaBH_4 \quad (9)$$

The solutions were then centrifuged and washed thoroughly before vacuum-drying at 120 °C. The recovered material was used to make Na half-cells. The first charge capacity is an indicator for how much Na was de-intercalated from the PBA material and the findings are summarized in Table IX.

Table IX. Chemical reduction results for MnHCF.

Samples	**Na**	**First Charge Capacity [mAh/g]**
As-received	1.22	~110
NaI Sodiation	1.54	~130
$NaBH_4$ Sodiation	1.56	~130

Table IX shows that the Na content was successfully increased from 1.22 to 1.54 and 1.56 by employing NaI or $NaBH_4$ as reducing agents. However, this additional step might increase the cost and time required for synthesis, which might not be ideal in industry and an optimized synthesis like the one shown in Section 5.1 can ensure high sodium content during synthesis in the first place.

Chapter 8. Electrochemical Evaluation of Prussian Blue Analogs

The electrochemical performance for the PBAs synthesized via the co-precipitation route is discussed next.

8.1. Voltage-Capacity Plots

Figure 8.1 shows the voltage-capacity curves (at a C/20 rate) for PBAs synthesized in this study via the co-precipitation route, alongside commercial LFP. As expected, NiHCF shows only one charge/discharge plateau which is associated with the $Fe^{II \rightleftharpoons III}$ redox couple while Ni is inactive and remains in its +2 oxidation state in the 2-4.1 V vs. Na/Na^{+} voltage window, delivering 84.5 mAh/g reversible capacity which is near the theoretical capacity of ~85 mAh/g. Higher specific capacities of 143.2 and 161.7 mAh/g are observed for $Ni_{0.03}Mn_{0.97}HCF$ and MnHCF, respectively, due to the contribution of the $Mn^{II \rightleftharpoons III}$ redox couple. For a defect-free $Ni_{0.03}Mn_{0.97}HCF$ with ~3 at. % Ni, the theoretical capacity should be ~166.9 mAh/g instead of the 143.2 observed here. We ascribe this difference to $Fe(CN)_6$ vacancies, □, present in the structure (see Table VIII).

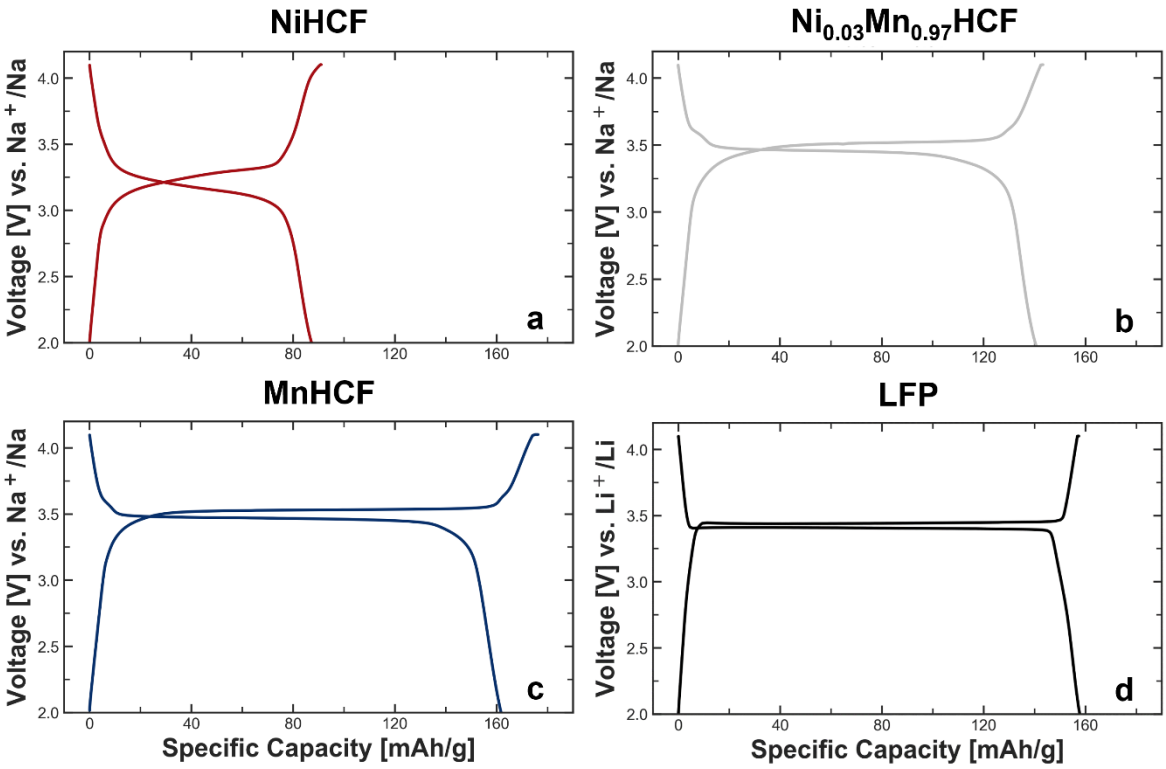

Figure 8.1. Voltage-capacity profiles of (a) NiHCF, (b) $Ni_{0.03}Mn_{0.97}HCF$, (c) MnHCF, and (d) LFP collected in half-cells at 30 °C using a C/20 rate (fourth cycle) between 2 and 4.1 V vs. Na/Na^+. The C-rate was calculated based on a specific capacity of 85 and 170 mAh/g for NiHCF and $Ni_{0.03}Mn_{0.97}HCF$/MnHCF/LFP, respectively. Na and Li half-cells were assembled with 1 M $NaPF_6$ and 1 M $LiPF_6$ in PC + 2 wt. % FEC, respectively.

The specific energy can be calculated by multiplying the specific capacity and the average discharge voltage. Gravimetric and volumetric energy densities for these materials are presented in Figures 8.2a and b, respectively. By comparing Figures 8.1c and d, it can be seen that MnHCF can deliver a materials-level specific energy of 552 Wh/kg, which is competitive with the LFP tested here at 537 Wh/kg. However, the lower crystal density of PBAs puts it at a disadvantage for volume-sensitive applications like long-range EVs (see Figure 8.2b). However, by leveraging low-cost raw materials and improving lifetimes, it

can be a competitive solution for applications such as ESS and short-range EVs.

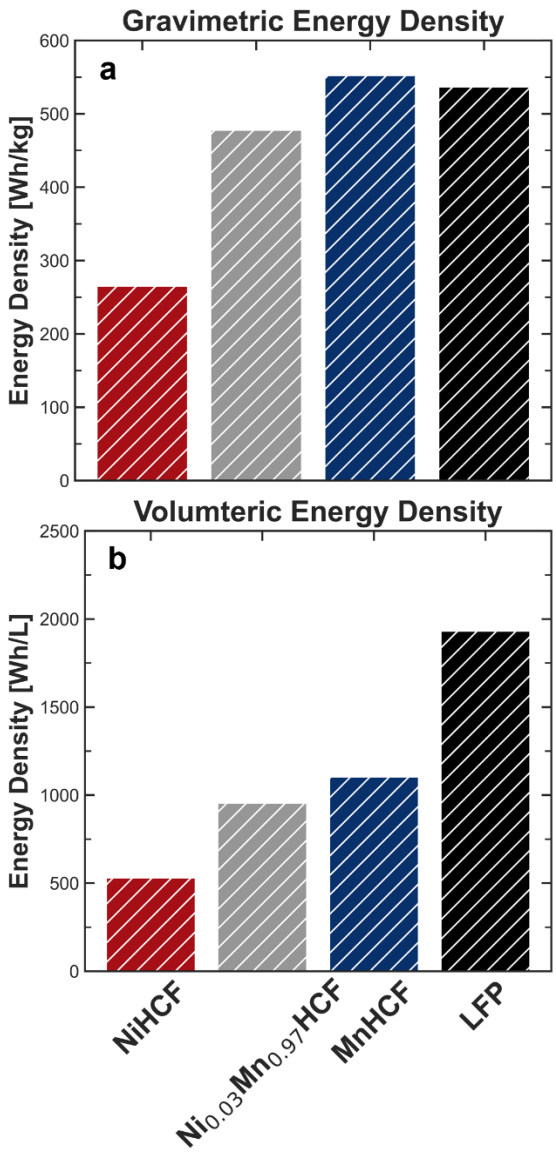

Figure 8.2. (a) Gravimetric and (b) volumetric energy densities for PBAs and LFP from Figure 8.1. For volumetric energy density calculations, crystal densities were used (2 and 3.6 g/cc for PBAs and LFP, respectively).

Despite having two distinct redox centers in the case of MnHCF (Mn and Fe), only one continuous charge/discharge plateau is visible. Song et al. reported two distinct

charge/discharge plateaus (3.1 and 3.5 V vs. Na/Na^+ for Fe and Mn, respectively) in the hydrated state (monoclinic phase) of MnHCF. However, after vacuum drying, the two plateaus merged to give a higher average discharge voltage like the one we reported here (see Figure 8.1c). This single-plateau behavior was also reported in other literature sources and is considered a signature feature for the voltage-capacity profile of rhombohedral MnHCF. [34][49][123] In the case of MnHCF, it seems that despite Fe and Mn having different energies, the fact that they are bonded to different atoms (C and N, respectively) diminishes the difference in energies. Whereas, in the case of rhombohedral FeHCF, where both C and N bonded sites are populated by Fe, two distinct steps in the voltage profiles are visible. [46]

8.2. Impact of Carbon Diluent on Electrochemical Performance of Prussian Blue Analogs

For the PBAs explored in this study, a few different electrode recipes were tested to assess the impact of carbon diluents on the electrochemical performance and the selected results are shown in Figure 8.3. For NiHCF, it was found that a relatively high active material content of 90 wt. % with 5 wt. % Super S as the carbon diluent can ensure stable performance. In the case of $Ni_{0.03}Mn_{0.97}HCF$ (and MnHCF most likely by extension), cells with even 20 wt. % Super S faded rather quickly. This was improved by switching from Super S to the high surface area carbon diluent Ketjen Black (see Figure 8.3). This indicates that maybe it is not the amount of carbon diluent, but rather the type of carbon diluent that dictates electrochemical performance at a certain point (and maybe the extent

of mixing as well). Hence, based on this result, all cells were made with Ketjen Black as the carbon diluent for the remainder of this thesis. The future work will focus on further increasing the active material fraction (to increase energy density) with Ketjen Black as the carbon diluent with the aim of not compromising electrochemical performance.

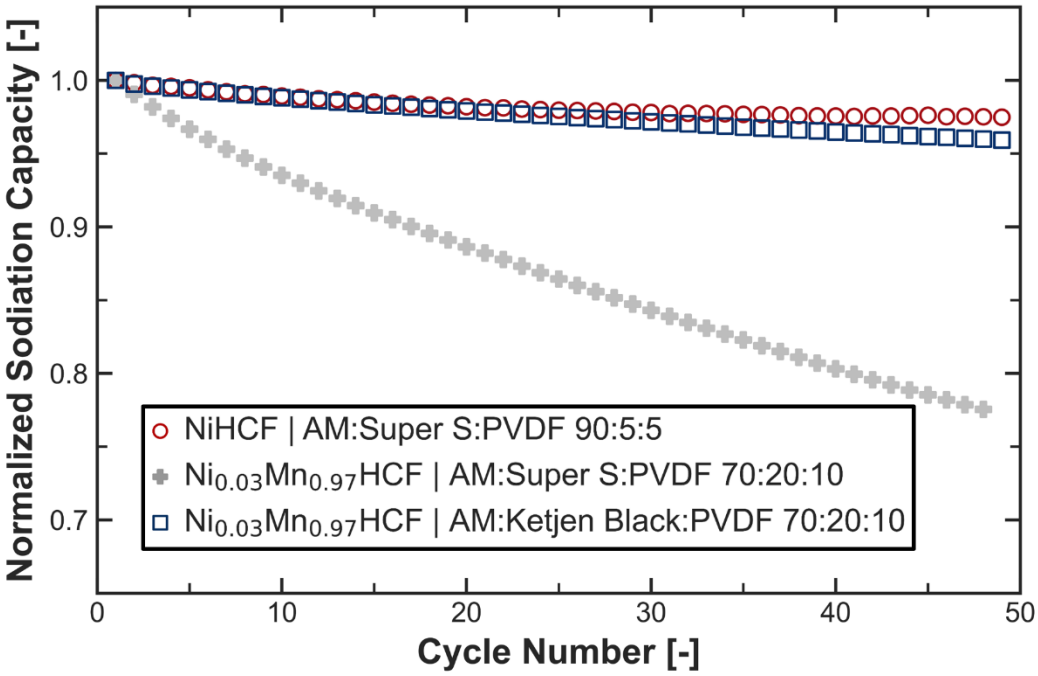

Figure 8.3. Effect of carbon diluents on different PBAs, NiHCF, $Ni_{0.03}Mn_{0.97}HCF$, and MnHCF, evaluated in half-cell format with Na metal as the counter electrode. The electrolyte used was 1 M $NaPF_6$ in PC + 2 wt. % FEC and cycled at 30 °C. All cells were cycled at a C/5 rate between 2 and 4.1 V vs. Na/Na^+ using CCCV charge (until I < C/20) and CC discharge. 1C current densities for NiHCF and $Ni_{0.03}Mn_{0.97}HCF$/MnHCF were assumed to be 85 and 170 mA/g, respectively.

8.3. C-rate Performance

It is important for a material to provide sufficient capacities at a variety of current densities

based on different use cases like fast charge or high-power applications. Figure 8.4 shows the rate capability of the as-synthesized PBAs and their comparison with commercial MnHCF and LFP in Na or Li half-cells. In this test, only the discharge current densities were varied. Charge current densities were kept low (C/10 for the first three cycles and C/5 for subsequent cycles) to prevent dendrite formation on the counter metal electrode. All PBAs show impressive rate capability, with NiHCF able to deliver more than 85% of its discharge capacity even at a high discharge rate of 10D (see Figure 8.4a). The as-synthesized $Ni_{0.03}Mn_{0.97}HCF$ and MnHCF materials perform competitively with commercial MnHCF and LFP, especially at discharge rates higher than 1D. At a current density of 10D, MnHCF retains ~82% capacity which is considerably greater than the 90% retention of NiHCF in absolute terms (theoretical capacity of MnHCF and NiHCF being 171 and 85 mAh/g, respectively). Figures 8.4b and c show the discharge voltage-capacity profiles during the C-rate performance tests with the commercial LFP and the MnHCF synthesized in this study, respectively. Both materials only start to show significant polarization at discharge rates greater than 2D, with MnHCF having a lower discharge voltage but a higher capacity than LFP at the 10D rate mark.

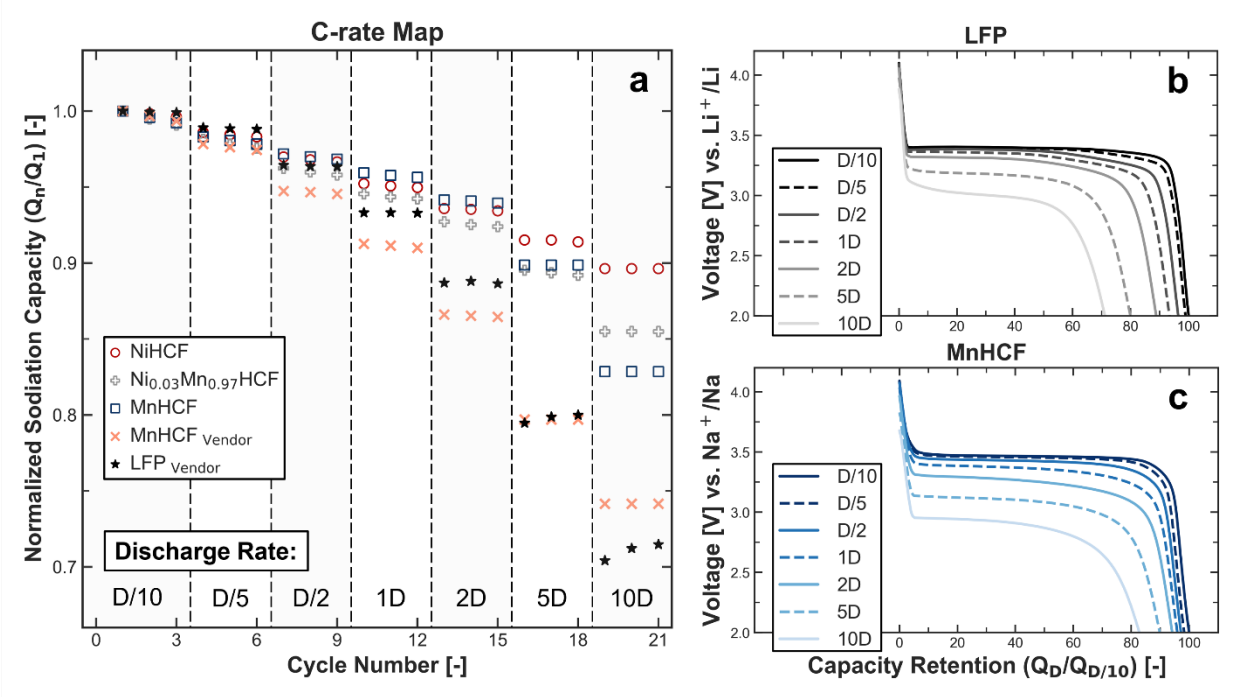

Figure 8.4. (a) Discharge rate maps for PBAs investigated in this study alongside commercial MnHCF and LFP in half-cells at 30 °C. Voltage-capacity profiles for the discharge part of the cycle for (b) LFP and (c) MnHCF. Charge current densities were kept low (C/10 for D10 cycles and C/5 for following cycles) to prevent non-uniform plating in half-cells with loading of 2-3 mg/cm^2. Na and Li half-cells were assembled with 1 M $NaPF_6$ and 1 M $LiPF_6$ in PC + 2 wt. % FEC, respectively.

8.4. Impact of Adding Ni to Sodium Manganese Hexacyanoferrate

Figure 8.5 shows the specific sodiation capacity, normalized sodiation capacity, voltage polarization, and coulombic efficiencies as a function of cycle number for the PBAs synthesized in this work (after vacuum-drying at 170 °C). NiHCF, despite having ~5 wt. % interstitial water (see Table VIII), shows excellent capacity retention (see Figure 8.5b). This suggests that the interstitial water does not compromise the performance of NiHCF, potentially because it is hard to remove the water from the bulk so that it does not leak

into the electrolyte during electrochemical cycling (see TGA data in Figure 6.2). MnHCF starts with a higher specific capacity than $Ni_{0.03}Mn_{0.97}$HCF and NiHCF, but after roughly 270 cycles, its absolute capacity drops below $Ni_{0.03}Mn_{0.97}$HCF (see Figure 8.4a). MnHCF also suffers from a faster growth in voltage polarization than the other two analogs (see Figure 8.5c). The performance of $Ni_{0.03}Mn_{0.97}$HCF is somewhere in between NiHCF and MnHCF, retaining close to 80% capacity after 3,500 hours of cycling, synergistically benefiting from Mn and Ni. Here, Mn provides additional capacity and Ni, even at just 3 at. % leads to better capacity retention. The coulombic efficiency of $Ni_{0.03}Mn_{0.97}$HCF is also higher than that of MnHCF, which further proves the positive effect of Ni doping. Apart from the benefits of Ni, the improved performance $Ni_{0.03}Mn_{0.97}$HCF, might also be ascribed to relatively a greater number of vacancies present in the structure than MnHCF. Cattermull and co-workers in their work discussed how having vacancies in the structure can reduce the ill effect of Jahn-Teller distortion by disrupting connectivity which can keep the distortions confined to local domains and impart flexibility. [126] The coulombic efficiency is an important metric for full-cells with limited Na inventory since it is correlated with the degree of parasitic reactions that can consume Na. All cycling data was collected in half-cells with reactive Na or Li metal as the counter electrode, and it is expected that a much longer lifetime can be achieved in full pouch cells with hard carbon electrodes and optimized electrolytes.

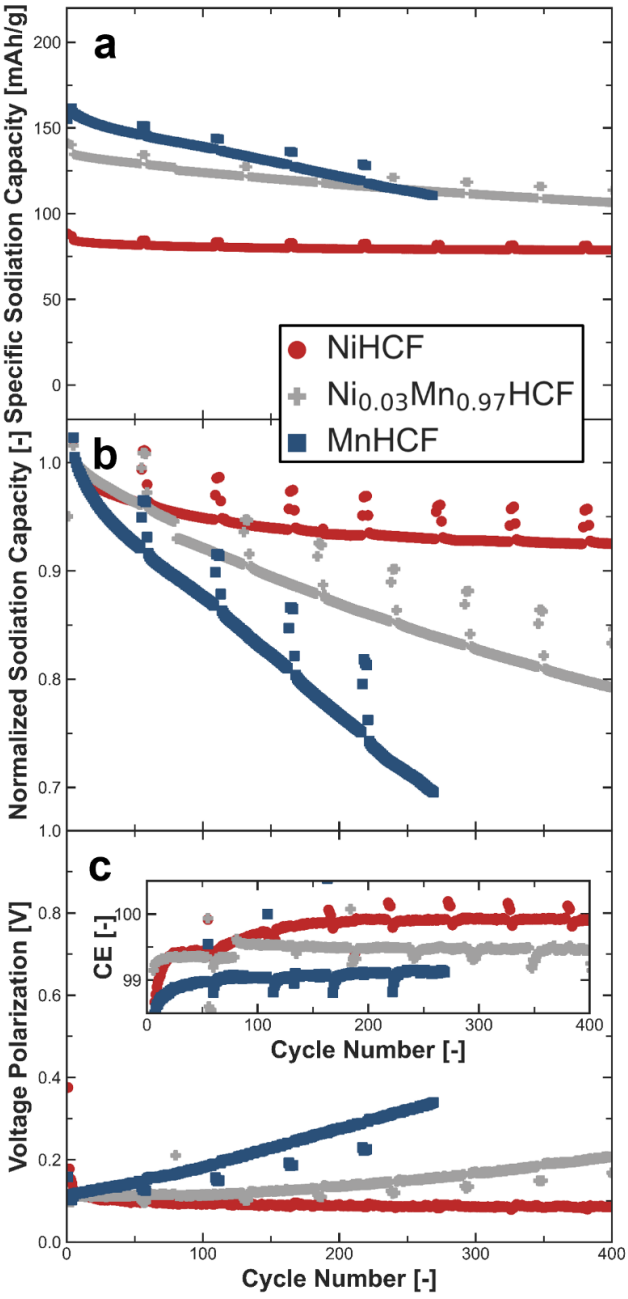

Figure 8.5. (a) Specific sodiation (i.e., discharge) capacity, (b) Normalized sodiation capacity (to third C/5 cycle), and (c) Voltage polarization (inset: Coulombic efficiency) for NiHCF, $Ni_{0.03}Mn_{0.97}HCF$, and MnHCF in half-cells with 1 M $NaPF_6$ in PC + 2 wt. % FEC as electrolyte and cycled at 30 °C. All cells were cycled at a C/5 rate between 2 and 4.1 V vs. Na/Na^+ using CCCV charge (until I < C/20) and CC discharge. Four C/20 "check-up" cycles were done after every 50 C/5 cycles. 1C rates for NiHCF and $Ni_{0.03}Mn_{0.97}HCF$/MnHCF were assumed to be 85 and 170 mA/g, respectively.

Why is NiHCF so much better than MnHCF? Similarities and Differences

Based on the previous discussion, NiHCF and MnHCF undergo different phase transitions due to the difference in the number of redox active sites, which can help explain the discrepancy in retention:

NiHCF: $Na_2Ni^{II}[Fe^{II}(CN)_6]$ (monoclinic) ⇌ $Na_1Ni^{II}[Fe^{III}(CN)_6]$) (cubic),

MnHCF: $Na_2Mn^{II}[Fe^{II}(CN)_6]$ (rhombohedral/monoclinic) ⇌ $Na_1Mn^{II}[Fe^{III}(CN)_6]$) (cubic) ⇌ $Na_0Mn^{III}[Fe^{III}(CN)_6]$ (tetragonal).

The fewer phase transitions per cycle can be a contributing factor to the excellent capacity retention of NiHCF. Also, since Ni does not contribute to redox activity, NiHCF is never fully de-sodiated and remains half-sodiated upon charge, whereas MnHCF is fully de-sodiated. The difference in remaining sodium content could be another factor that helps to explain this discrepancy in normalized capacity retention. Particle cracking and potential loss of active material could occur during repeated volumetric changes. As stated above, MnHCF undergoes an ~8% volume change upon charge/discharge whereas it is <1% for NiHCF, which could also be a contributing factor to capacity fade. [64]

The electronic configuration and the crystal distortions arising from it can be another contributing factor to the relatively poor capacity retention of MnHCF compared to NiHCF. Note that the low-spin state corresponds to a configuration with more paired electrons, while for the high-spin state, a fewer number of paired electrons exist. Mn and Ni (in MnHCF and NiHCF) exist with six N atoms bonded to them in an octahedral configuration,

whereas six C atoms are octahedrally bonded to Fe. In the case of NiHCF, Ni stays in the 2+ oxidation state, with an electronic configuration of $[Ar]3d^8$ (see Figure 8.6). This configuration makes it immune to Jahn-Teller distortion since all the degenerate orbitals are equally filled. In the case of MnHCF, Mn has a +3 oxidation state when charged and has the electronic configuration of $[Ar]3d^4$ (see Figure 8.6). In $Mn^{II/III}$-N≡C-$Fe^{II/III}$, Mn^{III} stays in a high-spin state due to the nature of the cyanide ligand. In the high-spin Mn^{3+}, the t_{2g} orbitals are half-filled with the same spin but there is only one electron in the e_g orbital (see Figure 8.6). Since e_g orbitals were degenerated at first and now they are unevenly occupied under the influence of the ligands, the relative lengths of the axial and equatorial bonds of the octahedral complexes can change such that the energy and symmetry of the molecule are reduced, which is referred to as Jahn-Teller distortion. Mn^{2+} with a $[Ar]3d^5$ configuration does not show Jahn-Teller distortion for its high-spin state, since degeneracy in both t_{2g} and e_g orbitals is maintained. These periodic distortions can cause structural instability and reduce the long-term stability of the material. The excellent performance of $Ni_{0.03}Mn_{0.97}$HCF may be due to the addition of small amounts of Ni in the M' site otherwise occupied by Mn and $Fe(CN)_6$ vacancies giving some flexibility to the structure, which might help alleviate the effect of Jahn-Teller distortion to some extent.

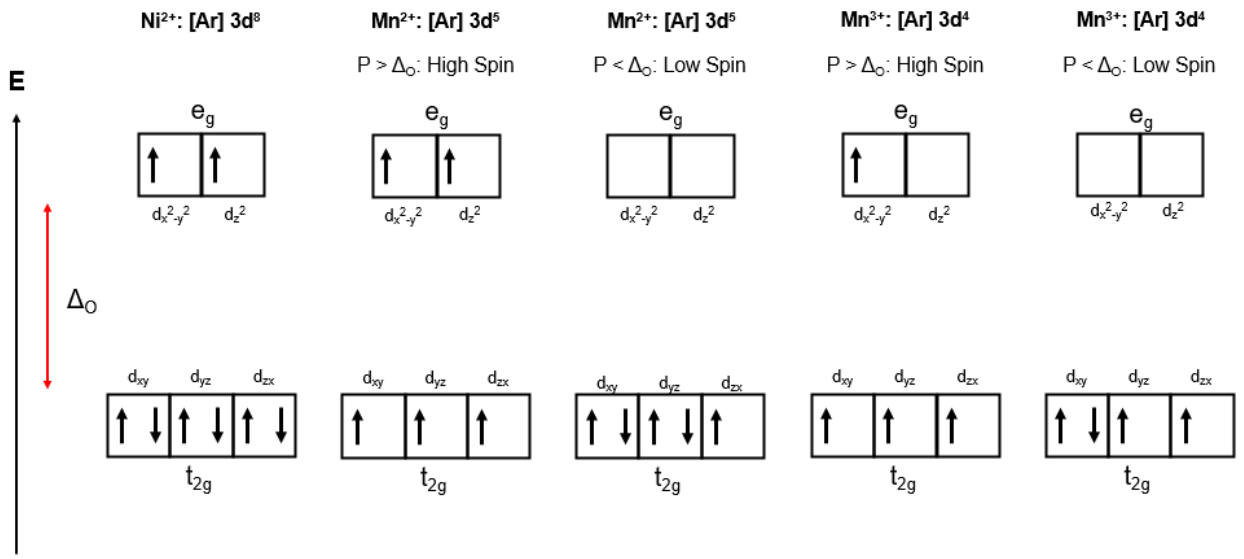

Figure 8.6. Possible electronic configurations for Ni^{2+}, Mn^{2+}, and Mn^{3+} in octahedral complexes.

8.5. Comparing Long-term Cycling Performance to Commercial Materials

Figure 8.7 shows the evaluation of the calendar life performance of PBAs synthesized in this study and its comparison to commercial MnHCF and MnHCF reported by Song et al. [34] MnHCF synthesized in this study can retain 70% of the capacity after 2,500 hours of cycling, which represents an improvement compared to the material reported by Song and co-workers from the Goodenough group, [34] and is higher than for most materials reported in the literature when evaluated on a time basis (see Table X). The synthesized NiHCF retains almost 95% of its capacity after 3,500 hours (~5 months) of cycling in the challenging environment of Na half-cell. This excellent performance of NiHCF may be attributed to its “zero-strain” nature and the absence of Jahn-Teller distortion. [127][128][29]

The $Ni_{0.03}Mn_{0.97}HCF$ material synthesized in this study can match the capacity retention and specific capacity of commercial MnHCF after more than 3,000 hours of cycling in the challenging half-cell format. The commercial MnHCF has a lower capacity than our MnHCF, most likely due to a higher degree of vacancies (i.e., fewer redox active sites).

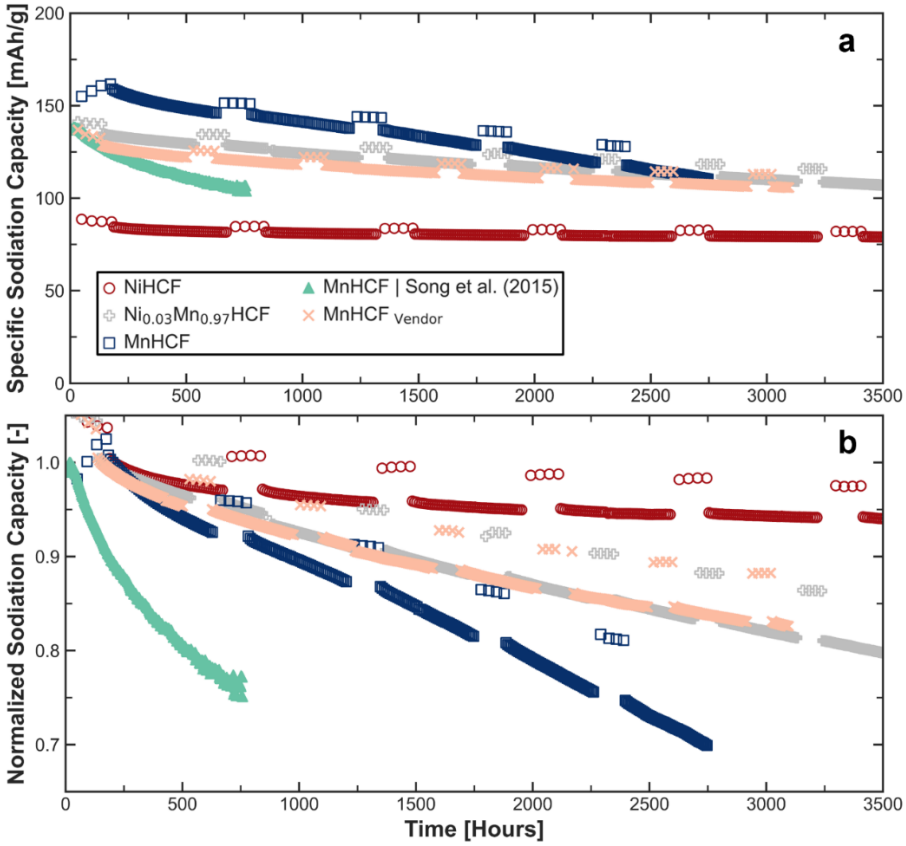

Figure 8.7. (a) Specific sodiation (i.e., discharge) capacity and (b) normalized sodiation capacity (to third C/5 cycle) vs. time for half-cells with NiHCF, $Ni_{0.03}Mn_{0.97}HCF$, and MnHCF 30 °C. The performance is compared to commercial MnHCF as well as MnHCF by Song et al. [34] All cells were cycled at a C/5 rate between 2 and 4.1 V vs. Na/Na^+ using CCCV charge (until I < C/20) and CC discharge protocol. Four C/20 "check-up" cycles were done after every 50 C/5 cycles. 1C rates for NiHCF and $Ni_{0.03}Mn_{0.97}HCF$/MnHCF/LFP were assumed to be 85 and 170 mA/g, respectively. Half-cells were assembled with 1 M $NaPF_6$ PC + 2 wt. % FEC electrolyte.

Table X. Electrochemical performance of PBAs from selected literature reports.

Material	Stoichiometry	Reversible Capacity [mAh/g]	Half-cell Retention After: Time [Hrs.] / Cycles [-], C-rate Used	Reference
NiHCF	$Na_{1.99}Ni[Fe(CN)_6]_{0.994}\square_{0.006}\cdot 0.0046H_2O$	**85 @0.05C**	**95%: 3,500 / 400, 0.2C**	**(This Work)**
	$Na_{1.45}Ni[Fe(CN)_6]_{0.87}\cdot 3.02H_2O$	70 @1.18C	97%: 2,240 / 8000, 5.88C	[81]
	$Na_{1.29}Ni[Fe(CN)_6]\cdot 1H_2O$	70 @1C	99%: ~140 / 100, 1.18C	[63]
$Ni_aMn_{1-a}HCF$	$Na_{1.76}Ni_{0.03}Mn_{0.974}[Fe(CN)_6]_{0.86}\square_{0.14}\cdot 0.0005H_2O$	**140 @0.05C**	**76%: 4,400 / 509, 0.2C**	**(This Work)**
	$Na_{1.17}Ni_{0.12}Mn_{0.88}[Fe(CN)_6]_{0.79}\square_{0.21}\cdot 1.5H_2O$	110 @0.2C	95%: ~1,000 / 100, C/5	[64]
	$Na_{1.37}Ni_{0.54}Mn_{0.46}[Fe(CN)_6]\cdot 0.7H_2O$	93 @~0.6C	96%: ~930 / 500, 0.81C	[63]
MnHCF	$Na_{1.88}Mn[Fe(CN)_6]_{0.95}\square_{0.049}\cdot 0.0004H_2O$	**162 @0.05C**	**70%: 2,747 / 270, 0.2C**	**(This Work)**
	$Na_{1.94}Mn[Fe(CN)_6]_{0.94}\square_{0.06}\cdot 1.98H_2O$	169 @1C	88%: ~118 / 100, 1.7C	[44]
	$Na_{1.89}Mn[Fe(CN)_6]_{0.97}\cdot 0.3H_2O$	150 @0.1C	75%: 600 / 500, 0.7C	[34]

Chapter 9. Conclusion and Future Work

In this work, hydrothermal, mechanochemical, and co-precipitation routes for synthesizing Prussian Blue Analogs were explored. Optimization of co-precipitation route resulted in Na-rich monoclinic phase products for NiHCF, $Ni_{0.03}Mn_{0.97}HCF$, and MnHCF. The concern about water content in PBAs was addressed by employing an effective 170 °C vacuum-drying step before cell assembly. Heat treatment caused phase transformation in the case of $Ni_{0.03}Mn_{0.97}HCF$ and MnHCF (monoclinic to rhombohedral), unlike NiHCF. After heat treatment, the water content in $Ni_{0.03}Mn_{0.97}HCF$ and MnHCF was found to be <0.6 wt. %, while it was found to be ~5 wt. % for NiHCF. This showed that water movement might be hindered inside the crystal more for NiHCF because of its smaller unit cell volume, as verified by XRD refinement. Electrochemical performance for these materials was evaluated in Na half-cell format and compared to commercial and literature references as well. A high specific capacity discharge voltage of ~3.47 V of MnHCF led to a decent specific energy of 562 Wh/kg (materials level energy density), which is on par with commercial LFP. MnHCF showed good capacity retention of 70% after 2,500 hours in a half-cell, while NiHCF impressively retained 95% of capacity after over 3,500 hours of cycling. The capacity retention of MnHCF was augmented by adding ~3 at. % Ni dopant ($Ni_{0.03}Mn_{0.97}HCF$) which led to 76% capacity remaining after more than 4,400 hours of cycling. $Ni_{0.03}Mn_{0.97}HCF$ seems to benefit from a synergistic effect of both transition metals, with Mn improving the absolute capacity and Ni improving capacity retention. $Ni_{0.03}Mn_{0.97}HCF$ was also competitive with commercial MnHCF in terms of capacity retention. These in-house materials also performed greatly in rate tests, with the

ability to deliver over 80% of capacity and a high discharge rate of 10D.

Some possible next steps in this project include construction and evaluation of PBA/hard carbon full-cells, which can help to determine lifetimes with a limited Na inventory and more diverse cycling conditions. Post-mortem analysis of PBA electrodes is also suggested to check for the formation of new phases after cycling (using XRD) and particle cracking (using SEM). Furthermore, transition metal deposition on the negative electrode should be investigated since it has not received much attention in the PBA literature so far. A major area where future work should be placed on increasing the knowledge base regarding $Fe(CN)_6$ vacancies in these materials, as there is still a debate on the drawback and potential benefits arising from them. A series of materials with different amounts of vacancies and transition metals should be synthesized and evaluated to study their impact on long-term performance.

Electrolyte optimization will also be crucial for further prolonging the lifetimes of these materials. There is a large knowledge gap on comprehensive electrolyte formulations tailored for cells employing PBA positive electrode materials. It will be interesting to see if the electrolytes used in Na layered oxide/hard carbon cells work as well in PBA/hard carbon cells or if the choice of positive electrode materials in full-cells also influences performance. One major advantage of PBAs is that most of their capacity is accessible below 3.7 V, meaning that there are less chances of electrolyte oxidation. This may also permit the use of more competitive salts like NaFSI that may not work as well in layered oxide cells on their own due to the higher operating voltage and the associated risk of

anodic dissolution of the aluminum current collector. There should be an attempt to increase the reactant concentration during synthesis to increase the yield from a commercialization point of view. The impact of different precursors during synthesis (like sulfates, nitrates, chlorides, etc.) might also be interesting from a sustainability point of view. Since the ionic conductivity is very high for these materials, their performance should also be benchmarked and evaluated in low-temperature conditions, where other positive electrode active materials suffer. The application of novel carbon coating techniques is also worth investigating to address the limited electronic conductivities of polyanion materials, but it needs to be noted that traditional carbon coatings like the ones applied to LFP often require high temperatures that PBAs might not be able to tolerate. Since PBAs often require more rigorous drying conditions than other battery materials, the choice of separator is crucial as well since it often sets a limit on how high the drying temperature of a cell before the electrolyte filling step can be. Hence, separators with higher melting points (> 170 °C) should be explored to be compatible with these materials.

Appendix

Table XI. Energy density calculation for various Li-ion and Na-ion positive electrode materials.

Material	Specific Capacity [mAh/g]	Average Discharge Voltage [V]	Crystal Density [g/cc]	Gravimetric Energy Density [Wh/kg]	Volumetric Energy Density [Wh/L]	Upper Cutoff Voltage (UCV) [V]	Reference
LFP	159.4	3.367	3.6	536.8	1932.4	4.1	(This Work)
LCO (Theoretical)	274.0	4.05	5.08	1109.7	5637.3	5	-
LCO (4.2 UCV)	140.0	3.91	5.08	547.4	2780.8	4.2	[129]
LCO (4.6 UCV)	220.0	4.03	5.08	886.6	4503.9	4.6	[129]
NMC532	151.6	3.71	4.78	562.4	2688.4	4.2	[130]
NMC811	200.0	3.8	4.78	760.0	3632.8	4.2	[131]
NFM111	150.0	3.15	4.2	472.5	1984.5	4.1	[9]
NVPF	128.0	3.8	3.2	486.4	1556.5	4	[132]
MnHCF	168.8	3.44	2	580.7	1161.3	4.1	[44]

References

1. Jessie E. Harlow, Xiaowei Ma, Jing Li, Eric Logan, Yulong Liu, Ning Zhang, Lin Ma, Stephen L. Glazier, Marc M. E. Cormier, Matthew Genovese, Samuel Buteau, Andrew Cameron, Jamie E. Stark, J. R. Dahn, A Wide Range of Testing Results on an Excellent Lithium-Ion Cell Chemistry to be used as Benchmarks for New Battery Technologies. *Journal of The Electrochemical Society* **166**, A3031–A3044 (2019).

2. James Lu, Sophie, Frith, Will the Real Lithium Demand Please Stand Up? Challenging the 1Mt-by-2025 Orthodoxy, *BloombergNEF* (2019). https://about.bnef.com/blog/will-the-real-lithium-demand-please-stand-up-challenging-the-1mt-by-2025-orthodoxy/.

3. Aluminium Price, *Business Insider* (2024). https://markets.businessinsider.com/commodities/aluminum-price.

4. Copper Price, *Business Insider* (2024). https://markets.businessinsider.com/commodities/copper-price.

5. CRC Handbook of Chemistry and Physics. *CRC Handbook of Chemistry and Physics*, doi: 10.1201/9781315380476 (2016).

6. Claus Daniel, Jürgen Otto Besenhard, Handbook of Battery Materials: Second Edition. *Handbook of Battery Materials: Second Edition*, doi: 10.1002/9783527637188 (2011).

7. Yeru Liang, Chen Zi Zhao, Hong Yuan, Yuan Chen, Weicai Zhang, Jia Qi Huang, Dingshan Yu, Yingliang Liu, Maria Magdalena Titirici, Yu Lun Chueh, Haijun Yu, Qiang Zhang, A review of rechargeable batteries for portable electronic devices. *InfoMat* **1**, 6–32 (2019).

8. Roland Jung, Michael Metzger, Filippo Maglia, Christoph Stinner, Hubert A. Gasteiger, Oxygen Release and Its Effect on the Cycling Stability of LiNi x Mn y Co z O 2 (NMC) Cathode Materials for Li-Ion Batteries. *Journal of The Electrochemical Society* **164**, A1361–A1377 (2017).

9. Libin Zhang, Jay Deshmukh, Hussein Hijazi, Ziwei Ye, Michel B. Johnson, Andy George, Jeff R. Dahn, Michael Metzger, Impact of Calcium on Air Stability of Na[Ni 1/3 Fe 1/3 Mn 1/3]O 2 Positive Electrode Material for Sodium-ion Batteries. *Journal of The Electrochemical Society* **170**, 070514 (2023).

10. Arumugam Manthiram, A reflection on lithium-ion battery cathode chemistry. 1–9 (2020).

11. M. S. Whittingham, Electrical Energy Storage and Intercalation Chemistry. *Science* **192**, 1126–1127 (1976).

12. Akira Yoshino, The Birth of the Lithium-Ion Battery. *Angewandte Chemie International Edition* **51**, 5798–5800 (2012).

13. Bingxing Xie, Baoyu Sun, Tianyu Gao, Yulin Ma, Geping Yin, Pengjian Zuo, Recent progress of Prussian blue analogues as cathode materials for nonaqueous sodium-ion batteries. *Coordination Chemistry Reviews* **460**, 214478 (2022).

14. Karim Zaghib, Michel Trudeau, M V Reddy, Alain Mauger, Christian Julien, Michel Armand, (Invited) John B. Goodenough's Centenarian : Success Story of LiFePO 4 (LFP) As Cathode Material for Rechargeable Lithium Batteries. *ECS Meeting Abstracts* **MA2022-01**, 356 (2022).

15. Karim Zaghib, Alain Mauger, Henri Groult, John B. Goodenough, Christian M. Julien, Advanced electrodes for high power Li-ion batteries. *Materials* **6**, 1028–1049 (2013).

16. Samuel Hasselwander, Markus Meyer, Ines Österle, Techno-Economic Analysis of Different Battery Cell Chemistries for the Passenger Vehicle Market. *Batteries* **9** (2023).

17. Yong Sheng Hu, Yuqi Li, Unlocking Sustainable Na-Ion Batteries into Industry. *ACS Energy Letters* **6**, 4115–4117 (2021).

18. Meng Wang, Yingshuai Wang, Yuhang Xin, Qi Liu, Feng Wu, Hongcai Gao, Nitrogen-Doped Carbon Coated Na3V2(PO4)2F3 Derived from Polyvinylpyrrolidone as a High-Performance Cathode for Sodium-Ion Batteries. *ACS Applied Energy Materials* **6**, 4453–4461 (2023).

19. R. Dugas, B. Zhang, P. Rozier, J. M. Tarascon, Optimization of Na-Ion Battery Systems Based on Polyanionic or Layered Positive Electrodes and Carbon Anodes. *Journal of The Electrochemical Society* **163**, A867–A874 (2016).

20. Hussein Hijazi, Ziwei Ye, Libin Zhang, Jay Deshmukh, Michel B. Johnson, Jeff R. Dahn, Michael Metzger, Impact of Sodium Metal Plating on Cycling Performance of Layered Oxide/Hard Carbon Sodium-ion Pouch Cells with Different Voltage Cut-offs. *Journal of The Electrochemical Society* **170**, 070512 (2023).

21. Dong Zhao, Chunlei Wang, Yan Ding, Mingyue Ding, Yuliang Cao, Zhongxue Chen, Will Vanadium-Based Electrode Materials Become the Future Choice for Metal-Ion Batteries? *ChemSusChem* **15** (2022).

22. Marija Maisch, Tiamat secures funding for sodium-ion gigafactory in France, *pv magazine* (2024). https://www.pv-magazine.com/2024/01/19/tiamat-secures-funding-for-sodium-ion-gigafactory-in-france/.

23. C Delmas, C Fouassier, P Hagenmuller, Structral classification and properties of the layered oxides. *Physica B+C*, doi: 10.1016/0378-4363(80)90214-4 (1980).

24. Chenchen Wang, Luojia Liu, Shuo Zhao, Yanchen Liu, Yubo Yang, Haijun Yu, Suwon Lee, Gi Hyeok Lee, Yong Mook Kang, Rong Liu, Fujun Li, Jun Chen, Tuning local chemistry of P2 layered-oxide cathode for high energy and long cycles of sodium-ion battery. *Nature Communications 2021 12:1* **12**, 1–9 (2021).

25. Elena Marelli, Cyril Marino, Christoph Bolli, Claire Villevieille, How to overcome Na deficiency in full cell using P2-phase sodium cathode – A proof of concept study of Na-rhodizonate used as sodium reservoir. *Journal of Power Sources* **450**, 227617 (2020).

26. Alexander Kraft, What a chemistry student should know about the history of Prussian blue. *ChemTexts* **4**, 1–11 (2018).

27. Xin-Yuan Fu, Lu-Lu Zhang, Cheng-Cheng Wang, Hua-Bin Sun, Xue-Lin Yang, Recent progress of Prussian blue analogues as cathode materials for nonaqueous sodium-ion batteries. *Rare Metals*, doi: https://doi.org/10.1007/s12598-024-02887-3 (2024).

28. H.J. Buser, D. Schwarzenbach, W. Petter, A. Ludi, The Crystal Structure of Prussian Blue: Fe4[Fe(CN)6]3xH2O. *Inorganic Chemistry* **16** (1977).

29. Colin D. Wessells, Sandeep V. Peddada, Robert A. Huggins, Yi Cui, Nickel hexacyanoferrate nanoparticle electrodes for aqueous sodium and potassium ion batteries. *Nano Letters* **11**, 5421–5425 (2011).

30. Mauro Pasta, Colin D. Wessells, Robert A. Huggins, Yi Cui, A high-rate and long cycle life aqueous electrolyte battery for grid-scale energy storage. *Nature Communications* **3** (2012).

31. Bingxing Xie, Baoyu Sun, Tianyu Gao, Yulin Ma, Geping Yin, Pengjian Zuo, Recent progress of Prussian blue analogues as cathode materials for nonaqueous sodium-ion batteries. Elsevier (2022). https://doi.org/10.1016/j.ccr.2022.214478.

32. Hironobu Minowa, Yuhki Yui, Yoko Ono, Masahiko Hayashi, Katsuya Hayashi, Ryuchi Kobayashi, Kazue I. Takahashi, Characterization of Prussian blue as positive electrode materials for sodium-ion batteries. *Solid State Ionics* **262**, 216–219 (2014).

33. Long Wang, Jie Song, Ruimin Qiao, L. Andrew Wray, Muhammed A. Hossain, Yi De Chuang, Wanli Yang, Yuhao Lu, David Evans, Jong Jan Lee, Sean Vail, Xin Zhao, Motoaki Nishijima, Seizoh Kakimoto, John B. Goodenough, Rhombohedral Prussian white as cathode for rechargeable sodium-ion batteries. *Journal of the American Chemical Society* **137**, 2548–2554 (2015).

34. Jie Song, Long Wang, Yuhao Lu, Jue Liu, Bingkun Guo, Penghao Xiao, Jong-Jan Lee, Xiao-Qing Yang, Graeme Henkelman, John B. Goodenough, Removal of Interstitial H2O in Hexacyanometallates for a Superior Cathode of a Sodium-Ion Battery. *Journal of the American Chemical Society* **137**, 2658–2664 (2015).

35. F M Maddar, D Walker, T W Chamberlain, J Compton, A S Menon, M Copley, I Hasa, Understanding dehydration of Prussian white: from material to aqueous processed composite electrodes for sodium-ion battery application. *Journal of Materials Chemistry A* **11** (2023).

36. Louis Hartmann, Jay Deshmukh, Libin Zhang, Sebastian Buechele, Michael Metzger, Reversing the Chemical and Structural Changes of Prussian White After Exposure to Humidity to Enable Aqueous Electrode Processing for Sodium-ion Batteries. *Journal of The Electrochemical Society* **170**, 030540 (2023).

37. Mauro Pasta, Colin Wessells, Robert A. Huggins, Yi Cui, High rate, long cycle life battery electrode materials with an open framework structure (2015). https://patents.google.com/patent/WO2013032567A1/en.

38. Xianyong Wu, Chenghao Wu, Congxiao Wei, Ling Hu, Jiangfeng Qian, Yuliang Cao, Xinping Ai, Jiulin Wang, Hanxi Yang, Highly Crystallized Na2CoFe(CN)6 with Suppressed Lattice Defects as Superior Cathode Material for Sodium-Ion Batteries. *ACS Applied Materials and Interfaces* **8**, 5393–5399 (2016).

39. Changxiu Yan, Along Zhao, Faping Zhong, Xiangming Feng, Weihua Chen, Jiangfeng Qian, Xinping Ai, Hanxi Yang, Yuliang Cao, A low-defect and Na-enriched Prussian blue lattice with ultralong cycle life for sodium-ion battery cathode. doi: 10.1016/j.electacta.2019.135533 (2019).

40. Hang Zhang, Yun Gao, Jian Peng, Yameng Fan, Lingfei Zhao, Li Li, Yao Xiao, Wei Kong Pang, Jiazhao Wang, Shu Lei Chou, Prussian Blue Analogues with Optimized Crystal Plane Orientation and Low Crystal Defects toward 450 Wh kg−1 Alkali-Ion Batteries. *Angewandte Chemie International Edition*, e202303953 (2023).

41. Zeyu Wang, Wenchen Zhuo, Jinliang Li, Liang Ma, Shaozao Tan, Guiping Zhang, Hongzhang Yin, Weihai Qin, Hao Wang, Likun Pan, Aimiao Qin, Wenjie Mai, Regulation of ferric iron vacancy for Prussian blue analogue cathode to realize high-performance potassium ion storage. *Nano Energy* **98**, 107243 (2022).

42. Kevin Hurlbutt, Samuel Wheeler, Isaac Capone, Mauro Pasta, Prussian Blue Analogs as Battery Materials. *Joule* **2**, 1950–1960 (2018).

43. Cheryldine Q.X. Lim, Zhi Kuang Tan, Prussian White with Near-Maximum Specific Capacity in Sodium-Ion Batteries. *ACS Applied Energy Materials* **4**, 6214–6220 (2021).

44. Shunli He, Junmei Zhao, Xiaohui Rong, Chunliu Xu, Qiangqiang Zhang, Xing Shen, Xingguo Qi, Yuqi Li, Xinyan Li, Yaoshen Niu, Xiaowei Li, Shuai Han, Lin Gu, Huizhou Liu, Yong Sheng Hu, Solvent-free mechanochemical synthesis of Na-rich Prussian white cathodes for high-performance Na-ion batteries. *Chemical Engineering Journal* **428**, 131083 (2022).

45. Xianyong Wu, Wenwen Deng, Jiangfeng Qian, Yuliang Cao, Xinping Ai, Hanxi Yang, Single-crystal FeFe(CN)6 nanoparticles: A high capacity and high rate cathode for Na-ion batteries. *Journal of Materials Chemistry A* **1**, 10130–10134 (2013).

46. Long Wang, Jie Song, Ruimin Qiao, L. Andrew Wray, Muhammed A. Hossain, Yi De Chuang, Wanli Yang, Yuhao Lu, David Evans, Jong Jan Lee, Sean Vail, Xin Zhao, Motoaki Nishijima, Seizoh Kakimoto, John B. Goodenough, Rhombohedral Prussian white as cathode for rechargeable sodium-ion batteries. *Journal of the American Chemical Society* **137**, 2548–2554 (2015).

47. Ying Li, Kwok-Ho Lam, Xianhua Hou, CNT-modified two-phase manganese hexacyanoferrate as a superior cathode for sodium-ion batteries. *Inorg. Chem. Front* **8**, 1819 (2021).

48. Wanlin Wang, Yong Gang, Zhe Hu, Zichao Yan, Weijie Li, Yongcheng Li, Qin Fen Gu, Zhixing Wang, Shu Lei Chou, Hua Kun Liu, Shi Xue Dou, Reversible structural evolution of sodium-rich rhombohedral Prussian blue for sodium-ion batteries. *Nature Communications 2020 11:1* **11**, 1–9 (2020).

49. Chunliu Xu, Yongzhi Ma, Junmei Zhao, Peng Zhang, Zhao Chen, Chao Yang, Huizhou Liu, Yong Sheng Hu, Surface Engineering Stabilizes Rhombohedral Sodium Manganese Hexacyanoferrates for High-Energy Na-Ion Batteries. *Angewandte Chemie - International Edition* **62** (2023).

50. Jian Peng, Jiaqi Huang, Yun Gao, Yun Qiao, Huanhuan Dong, Yang Liu, Li Li, Jiazhao Wang, Shixue Dou, Shulei Chou, Defect-Healing Induced Monoclinic Iron-Based Prussian Blue Analogs as High-Performance Cathode Materials for Sodium-Ion Batteries. *Small* **19** (2023).

51. Daxian Zuo, Cuiping Wang, Jiajia Han, Qinghao Han, Yanan Hu, Junwei Wu, Huajun Qiu, Qian Zhang, Xingjun Liu, One-step synthesis of novel core-shell bimetallic hexacyanoferrate for high performance sodium-storage cathode. *Journal of Materials Science & Technology* **114**, 180–190 (2022).

52. Ratul Rehman, Jian Peng, Haocong Yi, Yi Shen, Jinwen Yin, Chang Li, Chun Fang, Qing Li, Jiantao Han, Highly crystalline nickel hexacyanoferrate as a long-life cathode material for sodium-ion batteries. *RSC Advances* **10**, 27033–27041 (2020).

53. Robert Awan, Asadullah, Lancashire, Crystal Field Theory. https://chem.libretexts.org/Bookshelves/Inorganic_Chemistry/Supplemental_Modules_and_Websites_(Inorganic_Chemistry)/Crystal_Field_Theory/Crystal_Field_Theory.

54. Mauro Pasta, Richard Y Wang, Riccardo Ruffo, Ruimin Qiao, Hyun-Wook Lee, Badri Shyam, Minghua Guo, Yayu Wang, L Andrew Wray, Wanli Yang, Michael F Toney, Yi Cui, Manganese-cobalt hexacyanoferrate cathodes for sodium-ion batteries. doi: 10.1039/c5ta10571d (2016).

55. Angelo Mullaliu, Mattia Gaboardi, Jasper Rikkert Plaisier, Stefano Passerini, Marco Giorgetti, Lattice Compensation to Jahn-Teller Distortion in Na-Rich Manganese Hexacyanoferrate for Li-Ion Storage: An Operando Study. *ACS Applied Energy Materials* **3**, 5728–5733 (2020).

56. Shu Zhang, Hongyi Chen, Jun Chen, Shouyi Yin, Yu Mei, Lianshan Ni, Andi Di, Wentao Deng, Guoqiang Zou, Hongshuai Hou, Xiaobo Ji, Mitigating the Jahn-Teller distortion driven by the spin-orbit coupling of lithium manganate cathode. *Journal of Energy Chemistry* **72**, 379–387 (2022).

57. Zhitong Xiao, Fanjie Xia, Linhan Xu, Xuanpeng Wang, Jiashen Meng, Hong Wang, Xiao Zhang, Lishan Geng, Jinsong Wu, Liqiang Mai, Suppressing the Jahn–Teller Effect in Mn-Based Layered Oxide Cathode toward Long-Life Potassium-Ion Batteries. *Advanced Functional Materials* **32** (2022).

58. Hyun Wook Lee, Richard Y. Wang, Mauro Pasta, Seok Woo Lee, Nian Liu, Yi Cui, Manganese hexacyanomanganate open framework as a high-capacity positive electrode material for sodium-ion batteries. *Nature Communications 2014 5:1* **5**, 1–6 (2014).

59. Hyun-Wook Lee, Mauro Pasta, Richard Y Wang, Riccardo Ruffo, Yi Cui, Effect of the alkali insertion ion on the electrochemical properties of nickel hexacyanoferrate electrodes. *Faraday Discussions* **176** (2014).

60. Yunpo Sun, Yunli Xu, Zheng Xu, Yu Sun, Xiongwen Xu, Jian Tu, Jian Xie, Shuangyu Liu, Xinbing Zhao, Long-life Na-rich nickel hexacyanoferrate capable of working under stringent conditions. *Journal of Materials Chemistry A* **9**, 21228–21240 (2021).

61. Xiaofei Bie, Kei Kubota, Tomooki Hosaka, Kuniko Chihara, Shinichi Komaba, Synthesis and electrochemical properties of Na-rich Prussian blue analogues containing Mn, Fe, Co, and Fe for Na-ion batteries. doi: 10.1016/j.jpowsour.2017.12.052 (2017).

62. Colin D. Wessells, Sandeep V. Peddada, Matthew T. McDowell, Robert A. Huggins, Yi Cui, The Effect of Insertion Species on Nanostructured Open Framework Hexacyanoferrate Battery Electrodes. *Journal of The Electrochemical Society* **159**, A98–A103 (2011).

63. Florian Gebert, David L. Cortie, James C. Bouwer, Wanlin Wang, Zichao Yan, Shi-Xue Dou, Shu-Lei Chou, Epitaxial Nickel Ferrocyanide Stabilizes Jahn–Teller Distortions of Manganese Ferrocyanide for Sodium-Ion Batteries. *Angewandte Chemie* **133**, 18667–18674 (2021).

64. Pu Hu, Wenbo Peng, Bo Wang, Dongdong Xiao, Utkarsh Ahuja, Julien Réthoré, Réthoré Réthoré,, Katerina E Aifantis, Concentration-Gradient Prussian Blue Cathodes for Na-Ion Batteries. **17**, 23 (2022).

65. Yue Xu, Mingyang Ou, Yi Liu, Jia Xu, Xueping Sun, Chun Fang, Qing Li, Jiantao Han, Nano Energy Crystallization-induced ultrafast Na-ion diffusion in nickel hexacyanoferrate for high-performance sodium-ion batteries. *Nano Energy* **67**, 104250 (2020).

66. Bingxing Xie, Liguang Wang, Jie Shu, Xiaoming Zhou, Zhenjiang Yu, Hua Huo, Yulin Ma, Xinqun Cheng, Geping Yin, Pengjian Zuo, Understanding the Structural Evolution and Lattice Water Movement for Rhombohedral Nickel Hexacyanoferrate upon Sodium Migration. *ACS Applied Materials and Interfaces* **11**, 46705–46713 (2019).

67. William R. Brant, Ronnie Mogensen, Simon Colbin, Dickson O. Ojwang, Siegbert Schmid, Lennart Häggström, Tore Ericsson, Aleksander Jaworski, Andrew J. Pell, Reza Younesi, Selective Control of Composition in Prussian White for Enhanced Material Properties. *Chemistry of Materials* **31**, 7203–7211 (2019).

68. Zu Tao Pan, Zheng Hua He, Jing Feng Hou, Ling Bin Kong, Designing CoHCF@FeHCF Core–Shell Structures to Enhance the Rate Performance and Cycling Stability of Sodium-Ion Batteries. *Small* **19** (2023).

69. Xiaofei Bie, Kei Kubota, Tomooki Hosaka, Kuniko Chihara, Shinichi Komaba, Synthesis and electrochemical properties of Na-rich Prussian blue analogues containing Mn, Fe, Co, and Fe for Na-ion batteries. *Journal of Power Sources* **378**, 322–330 (2018).

70. Wenhao Ren, Mingsheng Qin, Zixuan Zhu, Mengyu Yan, Qi Li, Lei Zhang, Dongna Liu, Liqiang Mai, Activation of Sodium Storage Sites in Prussian Blue Analogues via Surface Etching. *Nano Letters* **17**, 4713–4718 (2017).

71. Changxiu Yan, Along Zhao, Faping Zhong, Xiangming Feng, Weihua Chen, Jiangfeng Qian, Xinping Ai, Hanxi Yang, Yuliang Cao, A low-defect and Na-enriched Prussian blue lattice with ultralong cycle life for sodium-ion battery cathode. doi: 10.1016/j.electacta.2019.135533 (2019).

72. Hongyu Cheng, Yi-Nuo Liu, Zhuo-Er Yu, Yingying Song, Yinping Qin, Maomao Zhang, Riming Chen, Jingjing Zhou, Yang Liu, Bingkun Guo, Ion exchange to construct a high-performance core-shell MnFe-PB@CuFe-PB cathode material for sodium ion batteries. *J. Mater. Chem. C* **11**, 9787 (2023).

73. Yue Xu, Miao Chang, Chun Fang, Yi Liu, Yuegang Qiu, Mingyang Ou, Jian Peng, Peng Wei, Zhi Deng, Shixiong Sun, Xueping Sun, Qing Li, Jiantao Han, Yunhui Huang, In Situ FTIR-Assisted Synthesis of Nickel Hexacyanoferrate Cathodes for Long-Life Sodium-Ion Batteries. *ACS Applied Materials and Interfaces* **11**, 29985–29992 (2019).

74. Wanlin Wang, Yong Gang, Jian Peng, Zhe Hu, Zichao Yan, Weihong Lai, Yanfang Zhu, Dominique Appadoo, Mao Ye, Yuliang Cao, Qin Fen Gu, Hua Kun Liu, Shi Xue Dou, Shu Lei Chou, Effect of Eliminating Water in Prussian Blue Cathode for Sodium-Ion Batteries. *Advanced Functional Materials* **32** (2022).

75. Dickson O Ojwang, Lennart Häggström, Tore Ericsson, Jonas Ångström, William R Brant, Influence of sodium content on the thermal behavior of low vacancy Prussian white cathode material. **49**, 3570 (2020).

76. Shuangyan Qiao, Shihong Dong, Lingling Yuan, Ting Li, Meng Ma, Yifang Wu, Yingzhen Hu, Ting Qu, Shaokun Chong, Structure defects engineering in Prussian blue cathode materials for high-performance sodium-ion batteries. *Journal of Alloys and Compounds* **950**, 169903 (2023).

77. Jie Wang, Lan Li, Songlin Zuo, Yong Zhang, Liya Lv, Ran Ran, Xiaobao Li, Binglin Li, Fengkui Zhao, Jian Zhang, Yaqi Wang, Ping Nie, Synchronous crystal growth and etching optimization of Prussian blue from a single iron-source as high-rate cathode for sodium-ion batteries. *Electrochimica Acta* **341**, 136057 (2020).

78. Ning Wang, Jiachen Ma, Zhaolu Liu, Jie Xu, Deqiang Zhao, Nan Wang, Chen Yang, Yongjie Cao, Jing Lu, Junxi Zhang, An air-stable iron/manganese-based phosphate cathode for high performance sodium-ion batteries. *Chemical Engineering Journal* **433**, 133798 (2022).

79. T. Muraliganth, A. Manthiram, Understanding the shifts in the redox potentials of olivine LiM 1- yMyPO4 (M = Fe, Mn, Co, and Mg) solid solution cathodes. *Journal of Physical Chemistry C* **114**, 15530–15540 (2010).

80. Jinpeng Wu, Jie Song, Kehua Dai, Zengqing Zhuo, L. Andrew Wray, Gao Liu, Zhi Xun Shen, Rong Zeng, Yuhao Lu, Wanli Yang, Modification of Transition-Metal Redox by Interstitial Water in Hexacyanometalate Electrodes for Sodium-Ion Batteries. *Journal of the American Chemical Society* **139**, 18358–18364 (2017).

81. Liuxue Shen, Yu Jiang, Yuefeng Liu, Junlin Ma, Tongrui Sun, Nan Zhu, High-stability monoclinic nickel hexacyanoferrate cathode materials for ultrafast aqueous sodium ion battery. *Chemical Engineering Journal* **388**, 124228 (2020).

82. Hao Zhang, Yang Yang, Dongsheng Ren, Li Wang, Xiangming He, Graphite as anode materials: Fundamental mechanism, recent progress and advances. *Energy Storage Materials* **36**, 147–170 (2021).

83. Jin Ung Hwang, Jong Hoon Cho, Jong Dae Lee, Ji Sun Im, Characteristics of an artificial graphite anode material for rapid charging: manufactured with different coke particle sizes. *Journal of Materials Science: Materials in Electronics* **33**, 20095–20105 (2022).

84. Yu Lei, Siwei Zhang, Jiahui Dong, Yueteng Gao, Chongwei Gao, Yaojie Wei, Lei Qin, Da Han, Daqing Huang, Guodan Wei, Dengyun Zhai, Feiyu Kang, Potassium-enriched graphite for use as stable hybrid anodes in high-efficiency potassium batteries. *Carbon* **201**, 1030–1037 (2023).

85. Vijay A. Sethuraman, Laurence J. Hardwick, Venkat Srinivasan, Robert Kostecki, Surface structural disordering in graphite upon lithium intercalation/deintercalation. *Journal of Power Sources* **195**, 3655–3660 (2010).

86. Olena Lenchuk, Philipp Adelhelm, Doreen Mollenhauer, New insights into the origin of unstable sodium graphite intercalation compounds. *Phys. Chem. Chem. Phys* **21** (1937).

87. Hiroki Moriwake, Akihide Kuwabara, Craig A.J. Fisher, Yuichi Ikuhara, Why is sodium-intercalated graphite unstable? *RSC Advances* **7**, 36550–36554 (2017).

88. D. A. Stevens, J. R. Dahn, High Capacity Anode Materials for Rechargeable Sodium-Ion Batteries. *Journal of The Electrochemical Society* **147**, 1271 (2000).

89. Azusa Kamiyama, Kei Kubota, Daisuke Igarashi, Yong Youn, Yoshitaka Tateyama, Hideka Ando, Kazuma Gotoh, Shinichi Komaba, MgO-Template Synthesis of Extremely High Capacity Hard Carbon for Na-Ion Battery. *Angewandte Chemie International Edition* **60**, 5114–5120 (2021).

90. Biwei Xiao, Teófilo Rojo, Xiaolin Li, Hard Carbon as Sodium-Ion Battery Anodes: Progress and Challenges. *ChemSusChem* **12**, 133–144 (2019).

91. D. A. Stevens, J. R. Dahn, The Mechanisms of Lithium and Sodium Insertion in Carbon Materials. *Journal of The Electrochemical Society* **148**, A803 (2001).

92. Heather Au, Hande Alptekin, Anders C.S. Jensen, Emilia Olsson, Christopher A. O'Keefe, Thomas Smith, Maria Crespo-Ribadeneyra, Thomas F. Headen, Clare P. Grey, Qiong Cai, Alan J. Drew, Maria Magdalena Titirici, A revised mechanistic model for sodium insertion in hard carbons. *Energy & Environmental Science* **13**, 3469–3479 (2020).

93. Yusuke Morikawa, Shin ichi Nishimura, Ryu ichi Hashimoto, Masato Ohnuma, Atsuo Yamada, Mechanism of Sodium Storage in Hard Carbon: An X-Ray Scattering Analysis. *Advanced Energy Materials* **10**, 1903176 (2020).

94. Ning Sun, Jieshan Qiu, Bin Xu, Understanding of Sodium Storage Mechanism in Hard Carbons: Ongoing Development under Debate. *Advanced Energy Materials* **12**, 2200715 (2022).

95. Haijun Yu, Hongliang Dai, Ying Zhu, Huawen Hu, Ruirui Zhao, Benben Wu, Dongchu Chen, Mechanistic insights into the lattice reconfiguration of the anode graphite recycled from spent high-power lithium-ion batteries. *Journal of Power Sources* **481**, 229159 (2021).

96. Camélia Matei Ghimbeu, Adrian Beda, Bénédicte Réty, Hamza El Marouazi, Alen Vizintin, Blaž Tratnik, Loic Simonin, Julie Michel, John Abou-Rjeily, Robert Dominko, Review: Insights on Hard Carbon Materials for Sodium-Ion Batteries (SIBs): Synthesis – Properties – Performance Relationships. *Advanced Energy Materials* **14** (2024).

97. Ziyi Zhu, Feng Liang, Zhongren Zhou, Xiaoyuan Zeng, Ding Wang, Peng Dong, Jinbao Zhao, Shigang Sun, Yingjie Zhang, Xue Li, Expanded biomass-derived hard carbon with ultra-stable performance in sodium-ion batteries. *Journal of Materials Chemistry A* **6**, 1513–1522 (2018).

98. Chengxin Yu, Yu Li, Haixia Ren, Ji Qian, Shuo Wang, Xin Feng, Mingquan Liu, Ying Bai, Chuan Wu, Engineering homotype heterojunctions in hard carbon to induce stable solid electrolyte interfaces for sodium-ion batteries. *Carbon Energy* **5** (2023).

99. Changhyeon Kim, Huihun Kim, Milan K. Sadan, Minyeong Jeon, Gyu Bong Cho, Tae Hyun Nam, Kwon Koo Cho, Jou Hyeon Ahn, Hyo Jun Ahn, A high rate and long-cycle-life anode based on micrometer-sized Pb powder for sodium-ion batteries. *Journal of Alloys and Compounds* **886**, 161240 (2021).

100. Pranay Gandharapu, Arpita Das, Rashmi Tripathi, Velaga Srihari, Himanshu K. Poswal, Amartya Mukhopadhyay, Facile and Scalable Development of High-Performance Carbon-Free Tin-Based Anodes for Sodium-Ion Batteries. *ACS Applied Materials & Interfaces*, doi: 10.1021/ACSAMI.3C07305 (2023).

101. Matthew D L Garayt, Libin Zhang, Yixiang Zhang, Martins C Obialor, Jay Deshmukh, Yingjie Xing, Chongyin Yang, Michael Metzger, Jeff R Dahn, Practical Alloy-Based Negative Electrodes for Na-ion Batteries. *Journal of The Electrochemical Society* **171** (2024).

102. J. Y. Song, Y. Y. Wang, C. C. Wan, Conductivity Study of Porous Plasticized Polymer Electrolytes Based on Poly(vinylidene fluoride) A Comparison with Polypropylene Separators. *Journal of The Electrochemical Society* **147**, 3219 (2000).

103. Rosamaría Fong, Ulrich von Sacken, J. R. Dahn, Studies of Lithium Intercalation into Carbons Using Nonaqueous Electrochemical Cells. *Journal of The Electrochemical Society* **137**, 2009–2013 (1990).

104. Kanghua Pan, Haiyan Lu, Faping Zhong, Xinping Ai, Hanxi Yang, Yuliang Cao, Understanding the Electrochemical Compatibility and Reaction Mechanism on Na Metal and Hard Carbon Anodes of PC-Based Electrolytes for Sodium-Ion Batteries. *ACS Applied Materials and Interfaces* **10**, 39651–39660 (2018).

105. Yilong Lin, Qi Peng, Longwen Chen, Qi Zuo, Qingwu Long, Fenghui Lu, Sheng Huang, Yanwu Chen, Yuezhong Meng, Organic liquid electrolytes in sodium-based batteries: Actualities and perspectives. *Energy Storage Materials* **67**, 103211 (2024).

106. Bernardine L.D. Rinkel, David S. Hall, Israel Temprano, Clare P. Grey, Electrolyte oxidation pathways in lithium-ion batteries. *Journal of the American Chemical Society* **142**, 15058–15074 (2020).

107. Changchun Ye, Wenqiang Tu, Limei Yin, Qinfeng Zheng, Cun Wang, Yaotang Zhong, Yuegang Zhang, Qiming Huang, Kang Xu, Weishan Li, Converting detrimental HF in electrolytes into a highly fluorinated interphase on cathodes †. doi: 10.1039/c8ta06150e (2018).

108. GSAS-II. https://subversion.xray.aps.anl.gov/trac/pyGSAS.

109. VESTA Visualization for Electronic and Structral Analysis.

110. Match Phase Analysis using Powder Difrraction. https://www.crystalimpact.com/match/.

111. Jeremy Cockcroft, Paul Barnes, Advanced Certificate in Powder Diffraction on the Web. http://pd.chem.ucl.ac.uk/pd/indexnn.htm.

112. Monu Malik, Ka Ho Chan, Gisele Azimi, Review on the synthesis of LiNixMnyCo1-x-yO2 (NMC) cathodes for lithium-ion batteries. *Materials Today Energy* **28**, 101066 (2022).

113. Yinzhu Jiang, Shenglan Yu, Baoqi Wang, Yong Li, Wenping Sun, Yunhao Lu, Mi Yan, Bin Song, Shixue Dou, Prussian Blue@C Composite as an Ultrahigh-Rate and Long-Life Sodium-Ion Battery Cathode. *Advanced Functional Materials* **26**, 5315–5321 (2016).

114. Ya You, Xing-Long Wu, Ya-Xia Yin, Yu-Guo Guo, High-quality Prussian blue crystals as superior cathode materials for room-temperature sodium-ion batteries. doi: 10.1039/c3ee44004d (2014).

115. Hee Jin Maeng, Dae Han Kim, Nam Woon Kim, Hyun Ruh, Dong Kyu Lee, Hyunung Yu, Synthesis of spherical Prussian blue with high surface area using acid etching. *Current Applied Physics* **18**, S21–S27 (2018).

116. D. Wyrzykowski, L. Chmurzyński, Thermodynamics of citrate complexation with Mn2+, Co 2+, Ni2+ and Zn2+ ions. *Journal of Thermal Analysis and Calorimetry* **102**, 61–64 (2010).

117. Renjie Chen, Yongxin Huang, Man Xie, Ziheng Wang, Yusheng Ye, Li Li, Feng Wu, Chemical inhibition method to synthesize highly crystalline prussian blue analogs for sodium-ion battery cathodes. *ACS Applied Materials and Interfaces* **8**, 31669–31676 (2016).

118. Haoyu Yue, Zhijie Shang, Pan Xu, Dongyue Feng, Xinxue Li, Preparation of EDTA modified chitooligosaccharide/sodium alginate/Ca2+ physical double network hydrogel by using of high-salinity oilfield produced water for adsorption of Zn2+, Ni2+ and Mn2+. *Separation and Purification Technology* **280**, 119767 (2022).

119. Paula Sanz Camacho, Romain Wernert, Mathieu Duttine, Alain Wattiaux, Ashish Rudola, Palani Balaya, François Fauth, Romain Berthelot, Laure Monconduit, Dany Carlier, Laurence Croguennec, Impact of Synthesis Conditions in Na-Rich Prussian Blue Analogues. *ACS Applied Materials and Interfaces* **13**, 42682–42692 (2021).

120. Peng Zhang, Chunliu Xu, Junmei Zhao, Yongzhi Ma, Xin Hu, Lingyun Hao, Xiaowei Li, Yang Yang, Shuyin Xu, Huizhou Liu, Yong Sheng Hu, Rapid and solvent-free mechanochemical synthesis of Na iron hexacyanoferrate for high-performance Na-ion batteries. *Materials Today Energy* **27**, 101027 (2022).

121. Javier F. Reynes, Valerio Isoni, Felipe García, Tinkering with Mechanochemical Tools for Scale Up. *Angewandte Chemie - International Edition* **62** (2023).

122. Dickson O. Ojwang, Mikael Svensson, Christian Njel, Ronnie Mogensen, Ashok S. Menon, Tore Ericsson, Lennart Häggström, Julia Maibach, William R. Brant, Moisture-Driven Degradation Pathways in Prussian White Cathode Material for Sodium-Ion Batteries. *ACS Applied Materials and Interfaces* **13**, 10054–10063 (2021).

123. Zonglin Li, Xiaobing Lou, Shinuo Kang, Dingming Liu, Fushan Geng, Ming Shen, Bingwen Hu, In-cell dehydration of sodium manganese hexacyanoferrate cathode revealed by solid-state NMR. doi: 10.1016/j.mrl.2024.200135 (2024).

124. Yutaka Moritomo, Shota Urase, Takayuki Shibata, Enhanced battery performance in manganese hexacyanoferrate by partial substitution. *Electrochimica Acta* **210**, 963–969 (2016).

125. Pawel Jezowski, Olivier Crosnier, Thierry Brousse, Sodium borohydride (NaBH4) as a high-capacity material for next-generation sodium-ion capacitors. *Open Chemistry* **19**, 432–441 (2021).

126. John Cattermull, Mauro Pasta, Andrew L. Goodwin, Structural complexity in Prussian blue analogues. *Materials Horizons* **8**, 3178–3186 (2021).

127. Ya You, Xing Long Wu, Ya Xia Yin, Yu Guo Guo, A zero-strain insertion cathode material of nickel ferricyanide for sodium-ion batteries. *Journal of Materials Chemistry A* **1**, 14061–14065 (2013).

128. Jian Peng, Mingyang Ou, Haocong Yi, Xueping Sun, Yuanpeng Zhang, Bao Zhang, Yu Ding, Feng Wang, Songqi Gu, Carlos Alberto López, Wang Zhang, Yi Liu, Ju Fang, Peng Wei, Yuyu Li, Ling Miao, Jianjun Jiang, Chun Fang, Qing Li, María Teresa Fernández-Díaz, José Antonio Alonso, Shulei Chou, Jiantao Han, Defect-free-induced Na + disordering in electrode materials. *Energy & Environmental Science* **14**, 3130–3140 (2021).

129. Cong Lin, Jianyuan Li, Zu Wei Yin, Weiyuan Huang, Qinghe Zhao, Qingsong Weng, Qiang Liu, Junliang Sun, Guohua Chen, Feng Pan, Structural Understanding for High-Voltage Stabilization of Lithium Cobalt Oxide. *Advanced Materials* **36**, 2307404 (2024).

130. Mohammad Mohsen Loghavi, Ashkan Nahvibayani, Mohammad Hadi Moghim, Mohsen Babaiee, Shaghayegh Baktashian, Rahim Eqra, Electrochemical evaluation of LiNi0.5Mn0.3Co0.2O2, LiNi0.6Mn0.2Co0.2O2, and LiNi0.8Mn0.1Co0.1O2 cathode materials for lithium-ion batteries: from half-coin cell to pouch cell. *Monatshefte fur Chemie* **153**, 1197–1212 (2022).

131. Roland Jung, Robert Morasch, Pinar Karayaylali, Katherine Phillips, Filippo Maglia, Christoph Stinner, Yang Shao-Horn, Hubert A. Gasteiger, Effect of Ambient Storage on the Degradation of Ni-Rich Positive Electrode Materials (NMC811) for Li-Ion Batteries. *Journal of The Electrochemical Society* **165**, A132–A141 (2018).

132. Xin Chen, Qiao Wu, Peng Guo, Xiaojie Liu, Rational design of two dimensional single crystalline Na3V2(PO4)2F3 nanosheets for boosting Na+ migration and mitigating grain pulverization. *Chemical Engineering Journal* **439**, 135533 (2022).